

Dissertation zur Erlangung des Doktorgrades  
der Fakultät für Chemie und Pharmazie  
der Ludwig-Maximilians-Universität München

Interplay of superconductivity and  
magnetism in  $\text{Ba}_{1-x}\text{K}_x\text{Fe}_2\text{As}_2$   
and its potential as wire material

Josef Erwin Wiesenmayer  
aus  
Timișoara, Rumänien

2015

## **Erklärung**

Diese Dissertation wurde im Sinne von § 7 der Promotionsordnung vom 28. November 2011 von Herrn Prof. Dr. Dirk Johrendt betreut.

## **Eidesstattliche Versicherung**

Diese Dissertation wurde eigenständig und ohne unerlaubte Hilfe erarbeitet.

München, der 09.06.2015

Erwin Wiesenmayer

Dissertation eingereicht am 09.06.2015

1. Gutachter: Prof. Dr. Dirk Johrendt
2. Gutachter: Prof. Dr. Bettina Valeska Lotsch

Mündliche Prüfung am 07.07.2015

*Pentru voi*

## Danksagung

Ich danke besonders Herrn Prof. Dr. Johrendt für die freundliche Aufnahme in seinen Arbeitskreis, die Überlassung des interessanten und spannenden Themas und die hervorragende Betreuung während dieser Doktorarbeit.

Frau Prof. Dr. Lotsch möchte ich herzlich für die Übernahme des Zweitgutachtens danken.

Prof. Dr. Böttcher, Prof. Dr. Karaghiosoff, PD Dr. Minar und Prof. Dr. Schnick danke ich für ihre Bereitschaft am Rigorosum teilzunehmen.

Mein Dank gilt ebenso allen AK-Mitgliedern, ehemaligen und aktuellen: Daniel Bichler, Andreas Binek, Lars Bulthaupt, Katharina Förg, Rainer Frankovsky, Gina Friederichs, Franziska Hummel, Lola Lilosten, Catrin Löhnert, Katarina Marković, Marianne Martin, Fabian Nitsche, Ursula Pachmayr, Simon Peschke, Roman Pobel, Constantin von Schirnding, Anne Schulz, Juliane Stahl, Christine und Tobias Stürzer, Marcus Tegel und Veronika Zinth für die Integration in die Gruppe, Hilfe und Unterstützung bei unterschiedlichsten Problemen, die Einführung der Geräte/Programme bzw. Durchführung verschiedenster Messungen und natürlich auch für die Aktivitäten außerhalb der Arbeitszeit.

Marianne Martin und Marcus Tegel möchte ich danken für die Hilfe bei der Einarbeitung in das Thema und die fortwährende Unterstützung während der Bearbeitung des Themas.

Allen Praktikanten denen ich die Ehre hatte etwas über Festkörperchemie beibringen zu dürfen möchte ich aus tiefstem Herzen danken. Danke an Andreas Binek, Ursula Pachmayr, Katarina Marković, Markus Dunst, Derya Daniel Bessinger, Tobias Sebastian Hermann und Stefan Marchner.

Meinen Kooperationspartner Dr. Hubertus Luetkens, Dr. Gwendolyn Pascua, Dr. Rustem Kashanov, Dr. Zurab Shermadini, Dr. Zurab Guguchia, Dr. Andrea Malagoli, Dr. Marcus Tegel, Dr. Jan Engelmann, Eike Ahrens, Dr. Pablo Docampo

und Dr. Fabian Hanusch danke ich für die interessanten Diskussionen, Anregungen, die fortwährende Unterstützung und die lockere Gesprächsatmosphäre während und nach der Zusammenarbeit.

Danke an meine Kollegen im Labor: Erik Flügel, Sebastian Junggeburth, Alberto von Mankowski, Ida Pavlichenko, Anna Ranft, Christine und Tobias Stürzer, Katalin Szendrei, Hongji Wang, für die Diskussions- und Hilfsbereitschaft während meiner Doktorarbeit.

Herrn Hartl und Frau Obel möchte ich für die stets zügige und verlässliche Durchführung der ICP-Messungen danken.

Christian Minke, Thomas Miller und Wolfgang Wünschheim danke ich für die stets freundliche und kompetente Unterstützung bei EDX-Messungen, Computertechnischem, Technischem und Administrativem.

Frau Dewald möchte ich für ihre stets freundliche und unterstützende Art danken.

Meinen Kollegen in den Arbeitskreisen Lotsch, Oeckler und Schnick danke ich für die Hilfe die sie mir zukommen ließen und den Spaß den wir miteinander hatten.

Rainer Frankovsky und Florian Pucher möchte ich für ihre Hilfe beim Erlernen des Umgangs mit den Gloveboxen danken.

Meinen Freunden danke ich für die schönen Zeiten innerhalb und außerhalb der Universität!

Neben vielen anderen Dingen möchte ich Franziska Hummel herzlich für das Korrekturlesen der Dissertation danken.

Meiner Familie möchte ich für die Unterstützung und den Rückhalt danken, den ich mein ganzes Leben lang erfahren durfte.

"Viele *kleine* Leute,  
an vielen *kleinen* Orten,  
die viele *kleine Schritte* tun,  
können das Gesicht der Erde verändern."  
Sprichwort der Xhosa

---

# Contents

1	Introduction .....	1
2	Methods .....	10
2.1	Starting materials and synthesis conditions.....	10
2.2	Powder diffraction.....	10
2.2.1	X-ray powder diffraction .....	10
2.2.2	Rietveld refinements .....	11
2.3	AC susceptibility .....	11
2.4	Induced coupled plasma atomic absorption spectroscopy (ICP-AAS).....	12
2.5	Transmission/Scanning electron microscopy (TEM/SEM) and energy dispersive X-ray analysis (EDX) .....	12
2.6	Muon spin rotation and relaxation ( $\mu$ SR) .....	13
2.6.1	General considerations and properties .....	14
2.6.2	Principles and configurations of the $\mu$ SR experiments.....	15
2.7	Critical current density measurements .....	17
3	Microscopic coexistence of superconductivity and magnetism in $\text{Ba}_{1-x}\text{K}_x\text{Fe}_2\text{As}_2$ .....	19
3.1	Introduction.....	19
3.2	Synthesis.....	21
3.3	Results and discussion.....	23
3.3.1	AC susceptibility.....	23
3.3.2	Muon spin rotation and relaxation .....	24
3.4	Conclusion.....	29
4	Short-range magnetic order in $\text{Ba}_{1-x}\text{K}_x\text{Fe}_2\text{As}_2$ .....	30
4.1	Introduction.....	30
4.2	Synthesis.....	31

---

4.3	Results and discussion.....	32
4.3.1	Susceptibility.....	32
4.3.2	Moun spin rotation and relaxation.....	33
4.4	Conclusion.....	38
5	Rise of a new magnetic phase in $\text{Ba}_{0.8}\text{K}_{0.2}\text{Fe}_2\text{As}_2$ .....	40
5.1	Introduction.....	40
5.2	Synthesis.....	41
5.3	Results and discussion.....	42
5.3.1	AC susceptibility.....	42
5.3.2	Muon spin rotation and relaxation.....	43
5.4	Conclusion.....	48
6	Exploring the potential of $\text{Ba}_{0.6}\text{K}_{0.4}\text{Fe}_2\text{As}_2$ wires and tapes.....	49
6.1	Motivation.....	49
6.2	Powder synthesis and characterization.....	50
6.3	$\text{Ba}_{0.6}\text{K}_{0.4}\text{Fe}_2\text{As}_2$ wires and tapes.....	53
6.3.1	The powder in tube method.....	53
6.3.2	Properties of the wires and tapes.....	55
6.4	Discussion.....	65
7	Optimizing the synthesis process of $\text{Ba}_{1-x}\text{K}_x\text{Fe}_2\text{As}_2$ .....	67
7.1	Motivation.....	67
7.2	Synthetic difficulties.....	67
7.3	Element-based synthesis.....	70
7.4	Synthesis via mechanical alloying of ternary precursors.....	72
7.4.1	Precursor synthesis.....	73
7.4.1.1	$\text{BaFe}_2\text{As}_2$ .....	73
7.4.1.2	$\text{KFe}_2\text{As}_2$ .....	74
7.4.2	Mechanical alloying.....	75

---

7.4.2.1 Overview.....	75
7.4.2.2 Experimental details .....	76
7.4.2.3 Results of milling process A.....	77
7.4.2.4 Results of milling process B.....	80
7.5 Discussion .....	84
8 Summary and outlook.....	87
9 Appendix.....	93
10 Abbreviations.....	96
11 Scientific contributions.....	100
12 Bibliography.....	102



# 1 Introduction

One of the major challenges that humanity is facing in the 21st century is climate change. It is caused by the excessive emission of CO<sub>2</sub> because of the usage of fossil energy sources like oil, natural gas, and coal<sup>[1]</sup>. They are still our number one source of energy because they are well accessible, easily transportable and cheap in production. Therefore, the CO<sub>2</sub> level in the atmosphere increased by 40 % compared to pre-industrial times<sup>[2]</sup>. If this process continues, the earth will further warm up and the results may be devastating. Heat waves and droughts on one side and heavy precipitation and the intensification of hurricanes on the other side are just some of the events that are at least likely to occur with higher frequencies in the 21st century due to global warming<sup>[2]</sup>.

However, if the biggest industrial nations work together and reform their energy policy, the worst case scenario can be averted. Two key features of this reform are the efficient use of energy and the production of renewable, CO<sub>2</sub>-free energy. In both segments new high performance materials like high-temperature superconductors can play an important role for example in the development of wind turbines utilized for conversion of wind energy to electricity. They are an established way of producing "green" energy. In order to optimize the efficiency of these turbines new high tech generators using high-temperature superconductors like MgB<sub>2</sub><sup>[3]</sup> could lead to a noticeable weight and size reduction of the turbines and increase their efficiency to over 95 %<sup>[4]</sup> already including the energy used for the cooling of the superconductor.

Superconductivity is known since its discovery in 1911 in Hg (cooled by liquid helium) by Heike Kamerlingh Onnes<sup>[5-7]</sup>. Below a critical temperature ( $T_c$ ) the resistance drops to an infinitely small value and the material becomes an ideal diamagnet. This means that if a magnetic field  $H_{ext}$  is applied below  $T_c$ , a current is induced at the superconductor's surface creating a magnetic field expelling  $H_{ext}$  from the inside. This is called the Meissner effect. By raising the external field, the current on the surface of the superconductor also rises until a critical field  $H_c$  is reached. At this point, the magnetic flux either permeates the superconductor completely (type 1 superconductor) or penetrates the superconductor partially by the magnetic flux

creating a vortex lattice (Shubnikov phase of a type 2 superconductor). The vortices grow with increasing  $H_{\text{ext}}$  until the external field completely penetrates the superconductor. This field is called  $H_{c2}$ .

Because of these unique properties superconductors have been an intensively investigated class of materials for more than one century now. During this time the number of known superconducting materials grew steadily. First, superconductivity was found in elements like Nb ( $T_c = 9.25$  K)<sup>[8]</sup>, then in alloys like the A15 compounds Nb<sub>3</sub>Sn ( $T_c = 18.3$  K)<sup>[9]</sup> and Nb<sub>3</sub>Ge ( $T_c = 23$  K)<sup>[10]</sup>, chevrel phases like PbMo<sub>6</sub>Se<sub>8</sub> ( $T_c = 18$  K)<sup>[11]</sup> and various superconducting cuprates like HgBa<sub>2</sub>Ca<sub>2</sub>Cu<sub>3</sub>O<sub>8+x</sub> ( $T_c \approx 133$  K)<sup>[12]</sup>. Among the superconductors the last mentioned cuprates take a special place, being the first and up to now only class to become superconducting above the boiling point of nitrogen at 77 K. Unfortunately they exhibit a high anisotropy and their processability is limited due to their ceramic character making it hard to incorporate them in flexible materials. In 2001 superconductivity in MgB<sub>2</sub> was discovered<sup>[3]</sup>. It is up to now the superconductor with the highest  $T_c$  (39 K) that can be explained by the BCS theory (see below). The last milestone in superconductor research was achieved in 2008 when *Kamihara et al.* discovered that LaFeAsO<sub>1-x</sub>F<sub>x</sub> becomes superconducting at a temperature of 26 K<sup>[13]</sup>. Iron compounds until then weren't taken into consideration for superconductivity because of their magnetism. Ferromagnetism was considered to be a knock-out criterion for superconductivity for a long time<sup>[14]</sup>. As a consequence of the discovery of superconductivity in LaFeAsO<sub>1-x</sub>F<sub>x</sub> soon other iron pnictides and chalcogenides were investigated concerning their superconductivity and  $T_c$  in this class of materials was increased in a short time up to 55 K in SmFeAsO<sub>1-x</sub>F<sub>x</sub><sup>[15]</sup> and 56 K in Ca<sub>1-x</sub>Nd<sub>x</sub>FeAsF<sup>[16]</sup>. In the present work the focus lies on Ba<sub>1-x</sub>K<sub>x</sub>Fe<sub>2</sub>As<sub>2</sub>, a type 2 superconducting iron arsenide<sup>[17]</sup>, which was also discovered in 2008.

The iron-arsenide superconductors can be classified by their chemical stoichiometries. Ba<sub>1-x</sub>K<sub>x</sub>Fe<sub>2</sub>As<sub>2</sub> is a member of the 122<sup>[17]</sup> family, LaFeAsO<sub>1-x</sub>F<sub>x</sub> a member of the 1111 family. However, the class of the superconducting iron arsenides contains many more families like the 111<sup>[18]</sup>, the 21311<sup>[19]</sup>, the 32522<sup>[20]</sup>, the 1038<sup>[21]</sup>, or the 1048<sup>[22]</sup> compounds.

Iron-based superconductors exhibit layered structures. In  $\text{LaFeAsO}_{1-x}\text{F}_x$  ( $\text{LaO}$ )<sup>+</sup> layers alternate with ( $\text{FeAs}$ )<sup>-</sup> layers (Figure 1-1, left).  $\text{LaFeAsO}_{1-x}\text{F}_x$  crystallizes in a  $\text{ZrCuSiAs}$ -type structure in the space group  $P4/nmm$ .

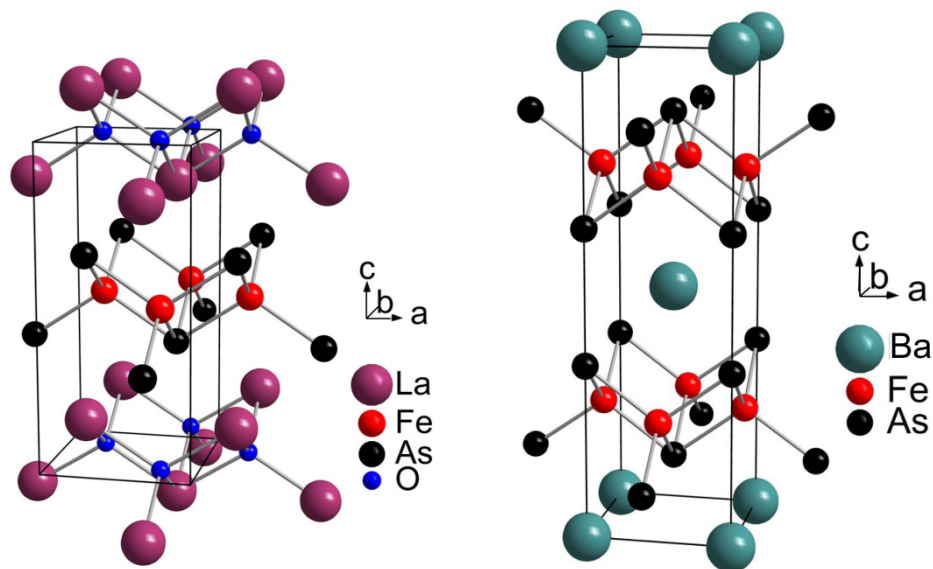


**Figure 1-1: Crystal structure of  $\text{LaFeAsO}$  (left) and  $\text{BaFe}_2\text{As}_2$  (right) as representatives for the 1111 and the 122 family of iron-arsenide superconductors.**

It undergoes a structural transition from  $P4/nmm$  to  $Cmme$ <sup>[23]</sup> at about 155 K followed by a transition into an antiferromagnetically ordered state at about 137 K<sup>[24]</sup>.  $\text{LaFeAsO}$  itself is not superconducting, but through partial substitution for example of oxygen by fluorine, the antiferromagnetic order is weakened and superconductivity emerges<sup>[13]</sup>.

All superconducting iron arsenides have one thing in common; they all consist of layers built from edge-sharing  $\text{FeAs}_{4/4}$  tetrahedra. In  $\text{Ba}_{1-x}\text{K}_x\text{Fe}_2\text{As}_2$  (Figure 1-1, right) the  $\text{FeAs}_{4/4}$  tetrahedral layers are separated by Ba/K atoms. Different from  $\text{LaFeAsO}$  the iron-arsenide layers are not just shifted along the  $c$ -axis but also half a unit cell along the  $a$ - and the  $b$ -axis.  $\text{BaFe}_2\text{As}_2$  with  $\text{BaZn}_2\text{P}_2$ -type structure<sup>[25]</sup> crystallizes in the tetragonal space group  $I4/mmm$  and was first synthesized in 1980<sup>[26]</sup>. Below a temperature of 140 K it undergoes a structural transition from  $I4/mmm$  to  $Fmmm$

(Figure 1-2) driven by spin-density wave (SDW)<sup>[27]</sup> ordering which leads to a stripe-type antiferromagnetic pattern.

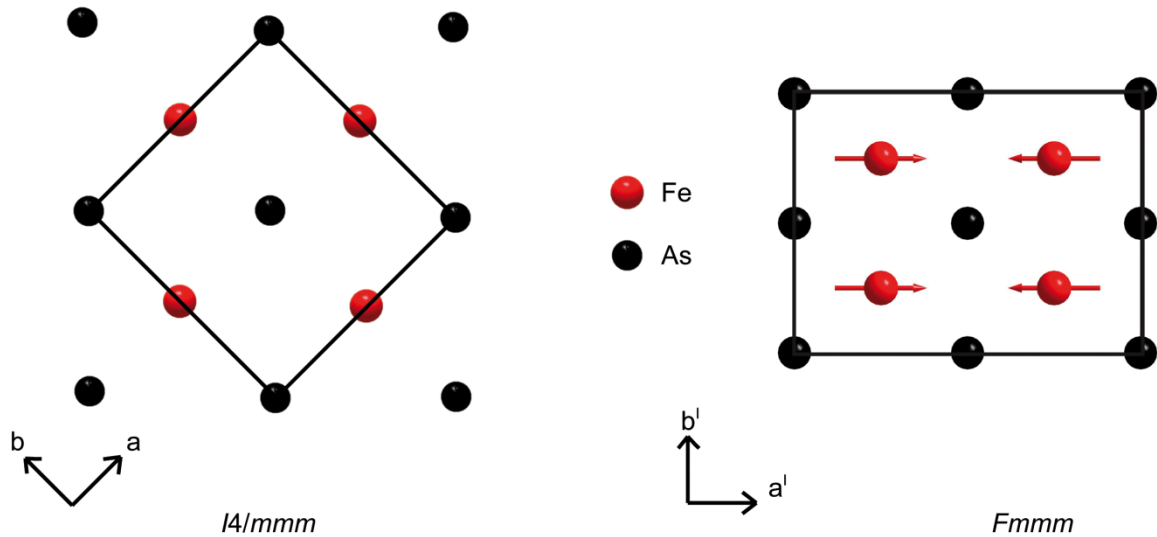


**Figure 1-2:** Schematic illustration of the  $ab$ -plane of the FeAs layers in  $\text{BaFe}_2\text{As}_2$  before (left) and after (right) the structural and magnetic transition into an orthorhombic stripe-type antiferromagnet.

In  $\text{BaFe}_2\text{As}_2$  a weakening of the antiferromagnetic state followed by superconductivity can be achieved by substituting either of the crystallographic sites of the structure. Substituting the barium site by potassium induces superconductivity with a critical temperature  $T_c$  of up to 38 K in  $\text{Ba}_{0.6}\text{K}_{0.4}\text{Fe}_2\text{As}_2$ <sup>[17]</sup> (hole doping). Exchanging iron by cobalt leads to superconductivity up to 23 K in  $\text{Ba}(\text{Fe}_{0.937}\text{Co}_{0.063})_2\text{As}_2$ <sup>[28]</sup> (electron doping). Superconductivity also arises through substitution of arsenic by phosphorous ( $T_{c,\text{max}} = 30$  K), which is a case of isoelectronic doping<sup>[29]</sup>. Finally, a doping agent is not even necessary to induce superconductivity in  $\text{BaFe}_2\text{As}_2$ . At a pressure of 5.64 GPa it becomes superconducting with a  $T_c$  of about 31 K<sup>[30]</sup>. All these methods change the situation at the Fermi surface, destabilize the antiferromagnetic order, and induce superconductivity.

The discovery of superconductivity in cuprates and afterwards in iron arsenides raised new questions about how superconductivity emerges. Until 1986 the

mechanism by which superconductivity is induced was described by the BCS theory<sup>[31-33]</sup> postulated by *J. Bardeen*, *L. N. Cooper* and *J. R. Schrieffer* in the 1950s. According to this theory the emergence of superconductivity is mediated through phonons (lattice vibrations) leading to a condensation of the conduction electrons into Cooper pairs. Cooper pairs are bosons and therefore no longer bound to the Pauli principle and can all occupy the same energetic state. Furthermore, as bosons they underlie the Bose-Einstein statistics instead of the Fermi-Dirac statistics and because of that cannot be scattered by the crystal lattice allowing resistance free electrical conductivity. The formation of all Cooper pairs can be described quantum mechanically by one wave function, the so-called "s-wave" (Figure 1-3, left) that is valid for most superconductors.

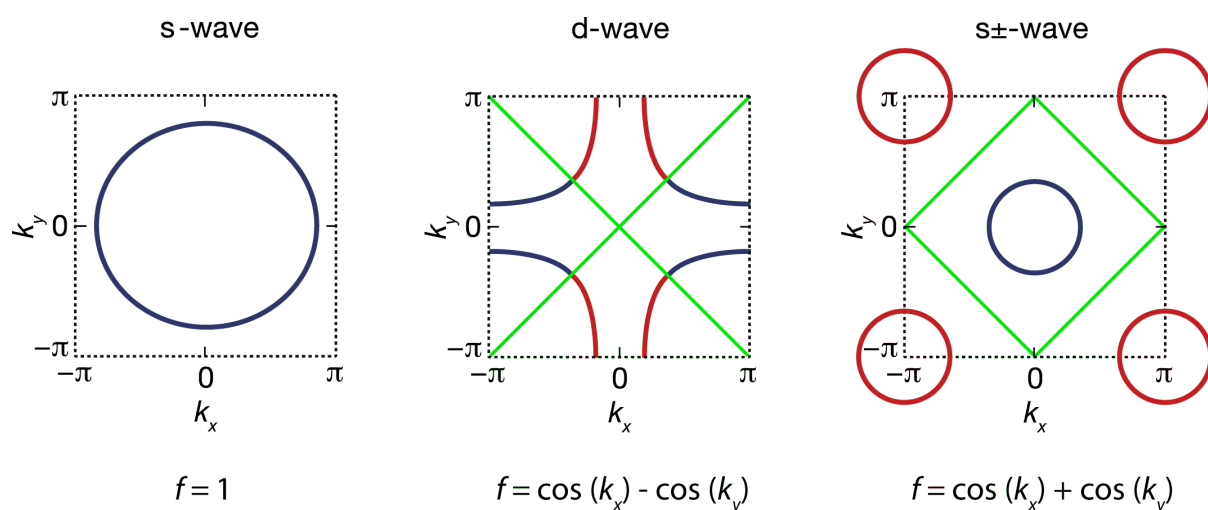


**Figure 1-3:** 2D representations of the Fermi surfaces and the Brillouin zones<sup>[34]</sup>. The green lines mark the nodes in the superconducting parameter. The blue and red circles emphasize the different signs of the pockets.  $f$  is the symmetry of the wave functions.

But the coupling of electrons to phonons is very weak, therefore this theory cannot explain superconductivity in materials with  $T_c > 40$  K<sup>[35]</sup>. It was proposed that the major contribution for the formation of the Cooper pairs in cuprates is provided by antiferromagnetic spin fluctuations instead of phonons<sup>[36]</sup>. The compounds showing this type of superconductivity are called "unconventional superconductors". The quasi 2D features of the CuO layers support large fluctuation effects, as a consequence of

the system having the tendency to develop long-range order<sup>[37]</sup>. In the parent compounds the spins display a checkerboard-like antiferromagnetic order<sup>[38]</sup>. Through doping the magnetic order can be weakened, the Mott insulating state can be overcome, and superconductivity emerges. The wave function of the Cooper pair condensation has "*d*-wave" symmetry. The order parameter of the *d*-wave gap is of  $(\cos(k_x) - \cos(k_y))$  symmetry, requiring a sign change and nodes (Figure 1-3, middle).

In contrast to the cuprates the iron arsenides are semi-metals<sup>[24]</sup>. They can be deduced from indirect semiconductors (Figure 1-4, left). But instead of an indirect bandgap, in semi-metals the bands overlap in energy and also overlap with the Fermi energy (Figure 1-4, right), allowing an electron transfer from the valence band to the conduction band.

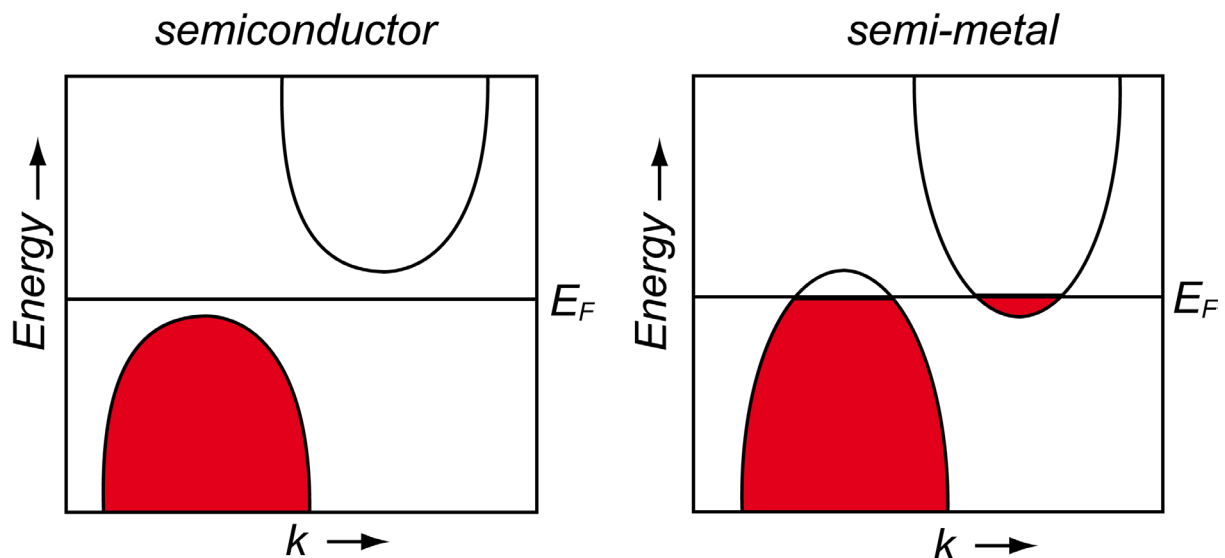


**Figure 1-4:** Left: Schematic band structure in an indirect semiconductor. Right: Schematic band structure in a semi-metal.

In this case the valence band is called "hole pocket", while the conduction band is called the "electron pocket". Doping of the electron and the hole pocket leads to a destabilization of the antiferromagnetic order, for example in  $\text{LaFeAsO}/\text{BaFe}_2\text{As}_2$  and induces superconductivity. Reducing the total amount of electrons by partly exchanging one element of a parent compound with another one having less valence

electrons, as described for  $\text{Ba}_{1-x}\text{K}_x\text{Fe}_2\text{As}_2$ , is called "hole doping". "Electron doping" is the opposite. Thereby, an element with a higher number of valence electrons replaces one in the parent compound, thus raising the number of electrons (as shown for  $\text{Ba}(\text{Fe}_{1-x}\text{Co}_x)_2\text{As}_2$ ). Although both methods of doping can lead to superconductivity, their effect on magnetism can be different<sup>[39]</sup>. Generally, in the case of the iron arsenides the antiferromagnetism is a result of a spin-density wave (SDW)<sup>[27]</sup>. Spin-density waves are incommensurate periodic modulations of electronic spins. They cause an energy gap, lowering the total energy of the system and occur in metals with low dimensionality and a high density of states at the Fermi surface. Doping prevents the SDW from entering the commensurate ordered state (antiferromagnetic ordering), while the low-energy fluctuations of the spin moments persist. Spin-fluctuation mediated superconductivity requires a sign change in the superconducting wave function, thus one expects *d*-wave symmetry (as in cuprates). ARPES experiments on iron-based materials revealed nodeless superconductivity (*s*-wave) on different sheets of the Fermi surface. The sign change occurs between different sheets, which is then denoted as *s*<sub>±</sub>-wave<sup>[40]</sup> (Figure 1-3, right). This scenario is generally accepted for the optimally doped  $\text{Ba}_{1-x}\text{K}_x\text{Fe}_2\text{As}_2$  ( $x = 0.4$ ) as well as for superconductivity in the underdoped area, between  $0.14 \leq x \leq 0.4$  of the phase diagram (Figure 1-5), while for strongly hole-doped  $\text{Ba}_{1-x}\text{K}_x\text{Fe}_2\text{As}_2$  the wave function transforms into a nodal *d*-wave<sup>[41]</sup>. But how superconductivity is induced and where exactly the transition of the wave function occurs in these materials is still under debate and has to be investigated further.

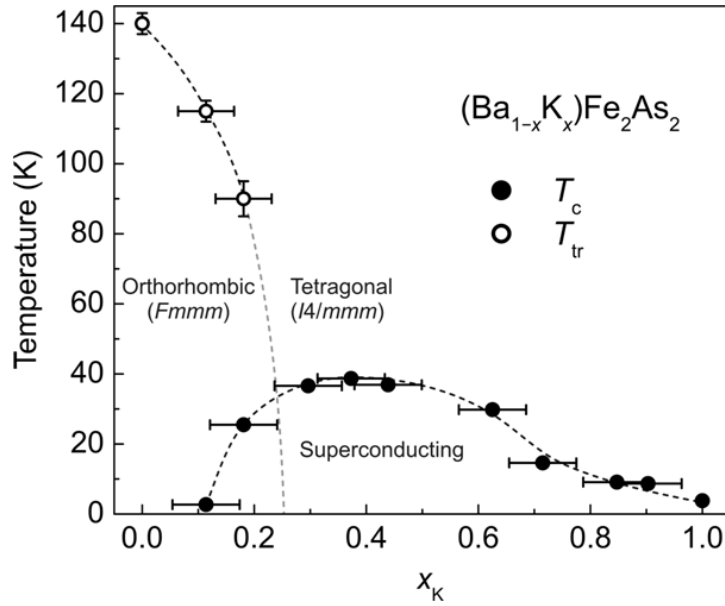


**Figure 1-5:** Phase diagram of  $\text{Ba}_{1-x}\text{K}_x\text{Fe}_2\text{As}_2$  including superconducting ( $T_c$ ) and phase transition ( $T_{tr}$ ) temperature<sup>[42]</sup>.

To study these fundamental questions potassium doped  $\text{BaFe}_2\text{As}_2$  is ideally suited. Understanding the transition from the antiferromagnetic to the superconducting state requires reliable and more detailed information about the phase diagram. The proposed  $s_{\pm}$ -wave symmetry within a spin fluctuation scenario would lead to microscopic coexistence of the superconducting and the magnetic order parameters<sup>[43]</sup>. On the other hand  $s_{++}$  as nodeless symmetry would lead to phase separation in superconducting (non-magnetic) and magnetic (non-superconducting) fractions<sup>[43]</sup>. One goal of this thesis is to clarify this fundamental question for  $\text{Ba}_{1-x}\text{K}_x\text{Fe}_2\text{As}_2$ , which is a challenge from the view of material synthesis as well as relevant physical methods. The interplay of superconductivity and magnetism is further explored in the optimally and overdoped regimes of the phase diagram, where a change of the gap symmetry has been suggested<sup>[41]</sup>. Based on recent developments<sup>[44]</sup>, by adding the additional dimension of physical pressure onto the underdoped region of the phase diagram of  $\text{Ba}_{1-x}\text{K}_x\text{Fe}_2\text{As}_2$ , a new phase was revealed. This implies a more complex situation in the phase diagram concerning the interplay of superconductivity and magnetism, even though the new phase has not been fully investigated yet. Furthermore, because of its relatively high  $T_c$  (up to 39 K), its air-stability, its high critical field  $H_{c2}$  (up to 60 T)<sup>[45]</sup>, and its weak field dependence,  $\text{Ba}_{0.6}\text{K}_{0.4}\text{Fe}_2\text{As}_2$  is a possible candidate for application in wires and tapes.

In the following chapters the interplay of magnetism and superconductivity in the underdoped regime of  $\text{Ba}_{1-x}\text{K}_x\text{Fe}_2\text{As}_2$  is investigated by a combination of high-resolution X-ray diffraction and  $\mu\text{SR}$  measurements on high-quality samples, proving a microscopic coexistence of both features (see chapter 3).

These studies are extended to the optimally and overdoped regime showing the evolution of the magnetism from a long-range antiferromagnetic order in the underdoped region to an unexpected short-range order in optimally doped  $\text{Ba}_{0.6}\text{K}_{0.4}\text{Fe}_2\text{As}_2$  and up to  $\text{Ba}_{0.34}\text{K}_{0.66}\text{Fe}_2\text{As}_2$ , simultaneously exploring a possible change in the superconducting wave function from *s*- to *d*-wave for  $x = 0.66$  (see chapter 4).

The rise of a new magnetic phase in underdoped  $\text{Ba}_{0.8}\text{K}_{0.2}\text{Fe}_2\text{As}_2$  under pressure is discovered and its interaction with superconductivity and the known magnetic phase at ambient pressure are examined on pressure-dependent  $\mu\text{SR}$  experiments (see chapter 5).

The experience obtained from these results is used to further explore a possible application of  $\text{Ba}_{0.6}\text{K}_{0.4}\text{Fe}_2\text{As}_2$  as a tape/wire material for a possible high field application (see chapter 6).

To deliver sufficient material for the proper exploration of the properties two new paths of synthesizing  $\text{Ba}_{1-x}\text{K}_x\text{Fe}_2\text{As}_2$  and especially  $\text{Ba}_{0.6}\text{K}_{0.4}\text{Fe}_2\text{As}_2$  are investigated. One is element based, the other one uses mechanical alloying of the ternary compounds  $\text{BaFe}_2\text{As}_2$  and  $\text{KFe}_2\text{As}_2$  (see chapter 7).

## 2 Methods

### 2.1 Starting materials and synthesis conditions

The starting materials used for the synthesis of the samples are listed in Table 2-1.

**Table 2-1: Starting materials used for the thesis.**

Starting material	Appearance	Purity [%]	Manufacturer
As	pieces	99.999*	Alfa Aesar
Ba	dendritic pieces	99.99	Sigma-Aldrich
Fe	powder	99.90	Chemetall
K	ingot	99.95*	Sigma-Aldrich

\* metal basis

In order to prevent oxidation, all weighing processes and the storage of the air- and moisture-sensitive samples were performed in two glove boxes (*MBraun* MB150-GL,  $O_2 < 1$  ppm,  $H_2O < 1$  ppm, and *MBraun* UNIlab Plus,  $O_2 < 0.1$  ppm,  $H_2O < 0.1$  ppm) filled with purified argon (*Argon 3.0, Air Liquide*). Alumina crucibles (*Friatec*) in silica ampoules (HSQ 300, *Vogelsberger*) were used as reaction containers. All samples were handled under dried argon. The argon was purified through three cylinders equipped with phosphorus pentoxide (*Merck*), a molar sieve (porewidth 0.4 nm, *Merck*) and BTS catalyst (*Fluka*). Solid state reactions were performed in resistance furnaces with Pt/PtRh thermocouples and programmable PID temperature controllers (model 2408, *Eurotherm*).

### 2.2 Powder diffraction

#### 2.2.1 X-ray powder diffraction

The first characterization was performed on *Huber* G670 Imaging Plate diffractometers (Cu- $K_{\alpha 1}$ -/Co- $K_{\alpha 1}$ -radiation,  $\lambda = 1.5406 \text{ \AA} / 1.7890 \text{ \AA}$ , Ge(111))

monochromator, silicon as external standard, (Guinier geometry) oscillating flat sample holder) or on a *STOE STADI P* (Mo-K $_{\alpha 1}$ -radiation  $\lambda = 0.7107 \text{ \AA}$  Ge(111) monochromator, silicon as external standard, rotating capillary (Debye-Scherrer geometry), 0.3 outer diameter).

Low-temperature powder patterns between 300 K and 10 K were measured on the *Huber* diffractometer with a closed-cycle helium cryostat model 22 CP provided by *CTI-CRYOGENICS*. The temperature was controlled by a *LAKESHORE-330-1* thermostat with a maximum deviation of about 0.1 K.

The gathered data were pre-processed with the program *HConvert*<sup>[34]</sup>. The programs *RAWDAT*<sup>[46]</sup> and *GRAPHICS*<sup>[47]</sup> in combination with the search algorithm "Search/Match", referring to the *JCPDS*-database<sup>[48]</sup>, were used for the identification and purity analysis of known phases. The program *THEO*<sup>[49]</sup> and the *Pearson's Crystal Data*-database<sup>[50]</sup> were used to create powder patterns of *JCPDS*-unknown phases.

### 2.2.2 Rietveld refinements

Using the *TOPAS* package<sup>[51]</sup> X-ray powder diffractograms were refined by the Rietveld method. *TOPAS* generates reflection profiles by using the fundamental parameters approach<sup>[52]</sup>, which involves crystallite microstructure effects and a convolution of appropriate source emission profiles with axial instrument contributions. Shape anisotropy and the peak half width were described by a modified approach of *Le Bail* and *Jouanneaux*<sup>[53]</sup>. The preferred orientation of the crystallites was described by spherical harmonics or March-Dollase functions<sup>[54-55]</sup>. For further information see [34].

## 2.3 AC susceptibility

AC susceptibility measurements were performed with a fully automated differential dual coil AC susceptometer. It is composed of a *Janis* SHI-950 two state closed-cycle cryostat, a dual channel temperature *LAKESHORE-332* temperature controller, an

EG&G-7260 DSP lock-in amplifier and a *Quantum Design* DC transport unit for sample centering and differential measurements<sup>[34]</sup>.  $^4\text{He}$  was used as exchange gas. Different parts of the susceptometer like the control software<sup>[56]</sup>, the coil assembly, the step controller, the sample holder, the coil assembly and other parts are developed by *Dr. Marcus Tegel*. The samples were placed in small gelatin capsules and fixed in straws before being attached to the sample holder and introduced into the susceptometer. The measurements were performed between 3.5 K and 50 K with altering magnetic fields up to 8 Oe at a frequency of 1333 kHz.

## **2.4 Induced coupled plasma atomic absorption spectroscopy (ICP-AAS)**

ICP-AAS measurements were performed on a *VARIAN* Vista RL. Powder samples were dissolved in a mixture of  $\text{HNO}_3$  and  $\text{HCl}$  and sprayed into a 10000 K argon plasma. As a result light of a certain wave length was emitted that is specific for the particular element. This light hits a CCD camera and thus can be quantified.

## **2.5 Transmission/Scanning electron microscopy (TEM/SEM) and energy dispersive X-ray analysis (EDX)**

Certain samples used for the wire and tape production were analyzed via transmission electron microscopy (TEM) and scanning electron microscopy (SEM). One part of the samples was investigated at the Italian Institute of Technology in Genoa, Italy, by *Dr. Alessandro Genovese*. High resolution TEM (HRTEM), energy filtered TEM (EFTEM) and high angle annular dark field (HAADF) scanning TEM (STEM) measurements were performed by a *JEOL* JEM-2200FS microscope, equipped with a Schottky electron source, a *CEOS* spherical aberration corrector of the objective lens which allows to reach a sub-angstrom resolution (0.9 Å), and an “in-column” Omega energy filter.

Spatially resolved chemical analysis was obtained in STEM mode via energy dispersive X-ray spectroscopy (EDX) using a *Bruker* Quantax 400 XFlash 6 T silicon drift detector (SDD) with an area of 60 mm<sup>2</sup> and chemical quantification calculated using the standardless Cliff-Lorimer method. TEM characterizations were carried out using a double tilt holder equipped with a beryllium tip to correctly align the lamellae along zone axes and to reduce the background in EDX analysis.

SEM characterizations of as-obtained lamellae were performed by a *JEOL* JSM-7500F. SEM analysis was carried out using a Rutherford backscattered electron imaging (RBEI) detector to increase electron contrast by adding a compositional contribution. SEM-EDX chemical analysis was performed using an *Oxford* X-Max 80 system with a SDD detector of 80 mm<sup>2</sup>.

Additional SEM and EDX measurements were performed by *Christian Minke* at the *Ludwig-Maximilians-University* in Munich, Germany, on a *JEOL* JSM-6500 equipped with a 7418 EDX detector provided by *Oxford Instruments*. The ground powder was attached to self-adhesive carbon plates (*PLANO GmbH*) on brass sample holders. Based on the characteristic X-ray emissions of the elements that were collected and analyzed with the INCA program package<sup>[57]</sup>. In order to increase the accuracy of the semi-quantitative results, several points on different positions of the sample were measured and averaged.

## 2.6 Muon spin rotation and relaxation ( $\mu$ SR)

With muon spin rotation and relaxation different physical properties like the magnetic order, magnetic fluctuations, superconductivity and their interplay in condensed matter can be investigated. The experiments were performed at the *Paul Scherrer Institute* in Switzerland on the  $\pi$ E1 and the  $\pi$ M3 beamlines at the GPS, Dolly, and the GPD spectrometers. The GPS and the Dolly spectrometers solely work at ambient pressure, while in the GPD spectrometer also pressure experiments can be conducted. The data obtained from the measurements was finally analyzed with the *MUSRFIT* package<sup>[58]</sup>.

### 2.6.1 General considerations and properties

Muons are leptons, have a mass of 200 electrons or 1/9 of a proton, a spin of 1/2, a life span of 2.2  $\mu\text{s}$ , and positive or a negative charge<sup>[59]</sup>. They are part of the cosmic radiation but can also be produced by shooting accelerated protons ( $E > 500 \text{ MeV}$ ) on a pyrolytic graphite or beryllium target. As a result positive and negative pions  $\pi^\pm$  are formed with a lifetime of 26 ns. Each pion  $\pi^\pm$  decays into a muon  $\mu^\pm$  and a neutrino  $\nu_\mu$  (Figure 2-1).

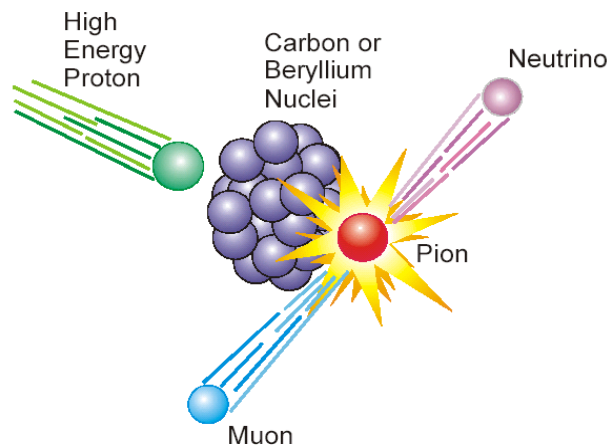
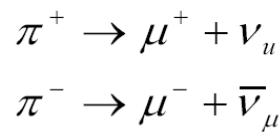


**Figure 2-1:** Illustration of the emergence and the decay of pions  $\pi^\pm$ <sup>[60]</sup>.

Here, only positively charged muons  $\mu^+$  are used. Negatively charged muons  $\mu^-$  are strongly attracted to the nuclei and thus provide more information about the core interactions. The  $\mu^+$ -beam is transported and focused on the sample by dipole and quadrupole magnets. Arriving at the sample the muons place themselves at highly symmetric interstitial lattice sites that are energetically favorable. Due to the parity violation of the muons<sup>[61-62]</sup> the beam is nearly 100 % spin polarized before and also after the implantation. In the sample the muons precess with the Larmor frequency  $\omega_L = \gamma \vec{H}$  around a magnetic field, either external or internal until the muon decays in a three body process into a positron and two neutrinos. The motion of the muon in a magnetic field is macroscopically described by the Bloch equations (Figure 2-2).

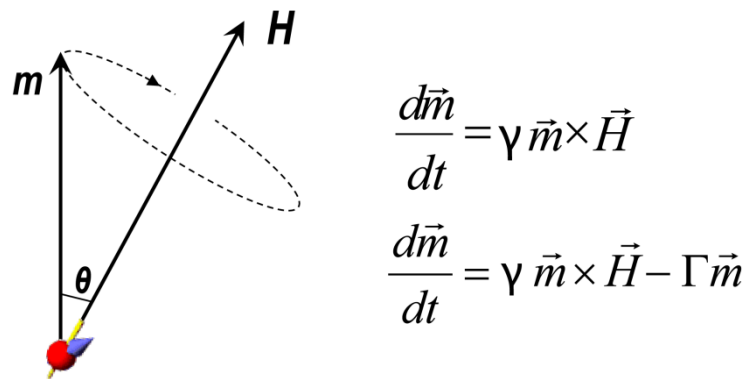


**Figure 2-2:** Left: Muon response to a magnetic field. Right: Bloch equations describing the motion of the muon in a magnetic field<sup>[60]</sup>.

$\vec{m}$  stands for the magnetization of the muon,  $\gamma$  is the gyromagnetic ratio,  $\vec{H}$  is the magnetic field the muon senses and the  $\Gamma\vec{m}$  term describes the relaxation of the muon. The positrons are emitted preferably along the direction of the spin in the moment of their decay. Knowing the before-mentioned features gives us the possibility to restore the time evolution of the muon spin.

### 2.6.2 Principles and configurations of the $\mu$ SR experiments

The goal of the experiment is to measure the time evolution of the spin polarization  $P(t)$  of a certain amount of muons. The measurement starts with the implantation of the  $\mu^+$  into the sample. Only one muon at a time is allowed into the sample. This guarantees that due to the dilution no major structural deformation can occur. Inside, the muon interacts with the magnetic environment until it decays after  $2.2 \mu\text{s}$  and emits a positron preferably along the muon spin direction in the moment of its destruction. This positron is detected by one of two positron counters arranged in the front and in the back of the muon beam.

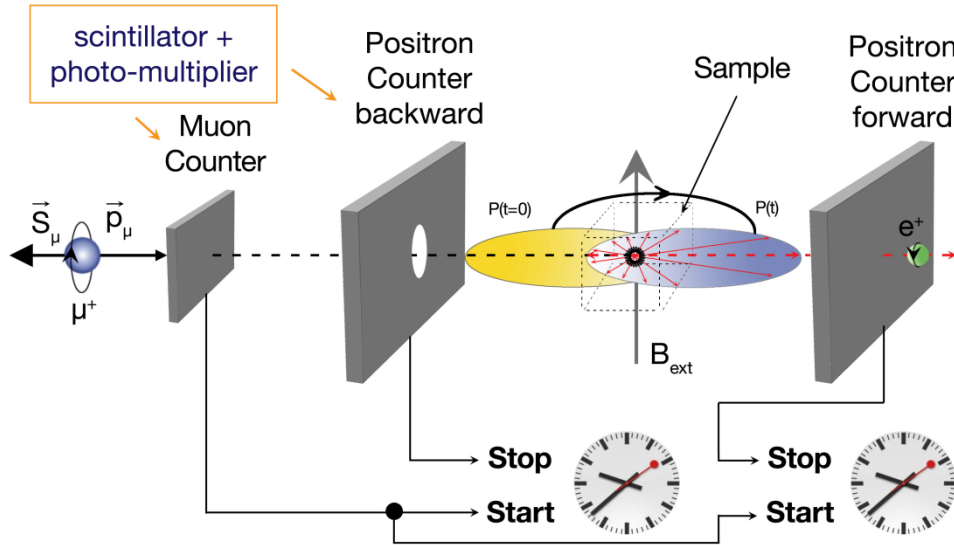


**Figure 2-3:** Schematic setup of a TF- $\mu$ SR experiment from the entrance of the muon into the spectrometer to the detection of decay product<sup>[63]</sup>.

If an additional muon reaches the sample within  $10 \mu\text{s}$  after the first implantation, the event is discarded. This is accomplished by an electronic trigger logic, accepting those events that have only one muon inside the sample in a certain time period. The electronic clock is started when an incoming muon is implemented into the sample and stops when a detector measures the emitted positron. Having two detectors, we obtain an oscillating signal with the frequency  $\omega_\mu$ . With the count rate of the forward  $N_F(t)$  and the backward  $N_B(t)$  detector the asymmetry signal  $A(t)$  can be calculated.

$$A(t) = A_0 P(t) = \frac{N_B(t) - N_F(t)}{N_B(t) + N_F(t)}$$

$A_0$  is the initial symmetry and depends on the absorption, the efficiency and the scattering of the positrons as well as the angle of the detector towards the muon beam. It has typical values between 0.25 and 0.3.  $A(t)$  and  $P(t)$  depend on the magnetic environment and the spatial distribution of the muons. With the help of these considerations information about the physical properties can be extracted from the  $\mu$ SR experiments depending on different setups. Different applied magnetic fields help to reveal a variety of effects. Zero field (ZF-)  $\mu$ SR with no external field grants access to the magnetic order parameter that is directly proportional to the frequency

of the  $\mu$ SR signal. Longitudinal field (LF-)  $\mu$ SR helps to obtain information about the superfluid density  $n_s$  in the superconducting state and transverse field (TF-)  $\mu$ SR can be used in combination with the other techniques to visualize the magnetic volume fraction of samples. Above that, the damping of the  $\mu$ SR-signal holds information about the inhomogeneity or the dynamics within a sample.

## 2.7 Critical current density measurements

The critical current density  $J_c$  is a measure for the quantity of current that can be transported in a superconducting wire or tape in a magnetic field perpendicular to the tape/wire. The application of a magnetic field limits this quantity. We investigated  $J_c$  on 10 - 12 mm pieces of superconducting wires or tapes that were produced in Genoa, Italy. The wires were fabricated by the powder in tube method by *Dr. Andrea Malagoli*, described in section 6.3.1. Basically there are two possibilities being used to measure  $J_c$ . The first one is by extracting it from magnetization hysteresis loops<sup>[64-65]</sup>. The second method, the one used on our wires and tapes, is to measure  $J_c$  by voltage-current-curves ( $V$ - $I$ -curves)<sup>[66-68]</sup>. These curves display the response on the application of a current on a wire/tape with a voltage criterion of 1  $\mu$ V/cm. The measurement is executed in a DC-four-probe homemade system that is positioned in a liquid helium bath (4.2 K). After connecting the voltage taps to the wire/tape and the wire/tape to the current leads by soldering (Figure 2-4), the equipment was implemented into the sample holder placed first in a Dewar with liquid nitrogen, in order to pre-cool it, and then into the proper Dewar filled with liquid helium to reach the final temperature. The holder can be equipped with two samples, but only one wire/tape at a time can be measured.

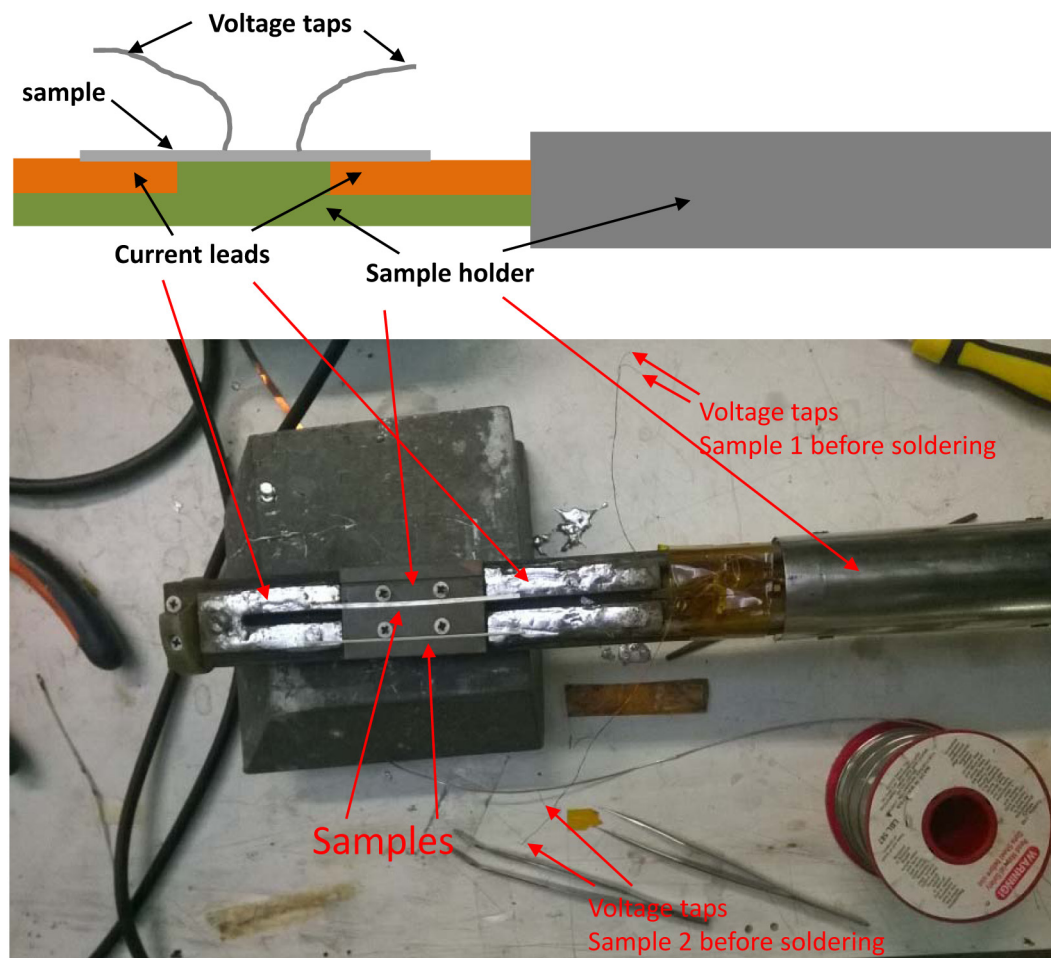


**Figure 2-4:** Schematic set up of a  $J_c$  measurement (up). Real set up of a  $J_c$  measurement before it is placed in a Dewar<sup>[69]</sup>.

The sample holder is positioned in the center of a 7 T split-coil magnet at the bottom of the Dewar. The magnetic field has a horizontal direction, perpendicularly to the longitudinal axis of the sample. During the experiment the current passes through the sample and the voltage is measured in the presence of the magnetic field. Each measurement is conducted in different magnetic fields and as a result the  $V-I$  curves are obtained. When examining a superconducting sample the current is increased until a measurable voltage is detected. This current value is called the critical current  $I_c$ , at which the superconductivity is destroyed. Taking the surface area of the superconductor and  $I_c$  into consideration  $J_c$  is calculated.

## 3 Microscopic coexistence of superconductivity and magnetism in $\text{Ba}_{1-x}\text{K}_x\text{Fe}_2\text{As}_2$

*Parts of this chapter are published in:* E. Wiesenmayer, H. Luetkens, G. Pascua, R. Khasanov, A. Amato, H. Potts, B. Banusch, H.-H. Klauss, Dirk Johrendt, *Physical Review Letters*, **2011**, *107*, 231001.

DOI: 10.1103/phyRevLett.107.231001

<http://journals.aps.org/prl/abstract/10.1103/PhysRevLett.107.237001>

© 2011 by The American Physical Society.

### 3.1 Introduction

The interplay of structural, magnetic and superconducting order parameters is one of the most intriguing aspects in iron-based superconductors. In the  $\text{LaFeAsO}$  (1111) and  $\text{BaFe}_2\text{As}_2$  (122) families, superconductivity (SC) evolves from non-superconducting parent compounds with tetragonal crystal structures that are subject to tiny orthorhombic lattice distortions below certain temperatures ( $T_s$ ). Static long-range antiferromagnetic ordering emerges at Néel temperatures ( $T_N$ ) well below  $T_s$  in  $\text{LaFeAsO}$ <sup>[24]</sup>, but very close to  $T_s$  in  $\text{BaFe}_2\text{As}_2$ <sup>[27]</sup>. The structural and magnetic transitions of the parent compounds are suppressed and finally eliminated by doping of the FeAs layers by electrons or holes, and superconductivity emerges at certain doping levels<sup>[70]</sup>. With respect to the origin of unconventional superconductivity, the possible coexistence of magnetic and superconducting phases in the underdoped areas of the phase diagrams is of considerable interest. But the coupling of structural, magnetic and superconducting order parameters relies on microscopic phase coexistence that is often difficult to distinguish from mesoscopic phase separation. In the 122 family, microscopic coexistence of these orders is generally accepted for the electron-doped compounds  $\text{Ba}(\text{Fe}_{1-x}\text{Co}_x)_2\text{As}_2$ , while conflicting reports exist for the hole-doped compounds  $\text{Ba}_{1-x}\text{K}_x\text{Fe}_2\text{As}_2$ .

The coexistence of the orthorhombic structure with superconductivity has first been suggested for  $\text{Ba}_{1-x}\text{K}_x\text{Fe}_2\text{As}_2$  up to  $x \approx 0.2$  by X-ray powder diffraction<sup>[42]</sup>, while neutron diffraction experiments additionally showed long-range antiferromagnetic ordering up to  $x \approx 0.3$ <sup>[71]</sup>. Diffraction methods however only provide the mean structural information on a rather long spatial scale, and cannot supply conclusive information regarding phase separation.  $^{57}\text{Fe}$ -Mössbauer spectroscopy as a local probe indicated microscopic coexistence<sup>[72]</sup>, but other local probes such as muon spin rotation ( $\mu\text{SR}$ )<sup>[73-75]</sup> and NMR<sup>[76]</sup> showed phase separation with non-magnetic superconducting volume fractions between 25 and 40%. These experiments with almost optimally doped single crystals grown from fluxes constituted the paradigm of phase separation in underdoped  $\text{Ba}_{1-x}\text{K}_x\text{Fe}_2\text{As}_2$ .

In contrast to these scattered results, studies with cobalt-doped  $\text{Ba}(\text{Fe}_{1-x}\text{Co}_x)_2\text{As}_2$  yielded convincing evidence for microscopic coexistence<sup>[77]</sup>. Moreover, competing order parameters became obvious by the concomitant reduction of the orthorhombic lattice distortion  $\delta = (a-b)/(a+b)$  and magnetic moment  $\mu_{\text{Fe}}$  when crossing the critical temperature<sup>[28]</sup>. This microscopic coexistence supports  $\pm$ -symmetry of the superconducting order parameter<sup>[43, 78]</sup> and gives strong evidence for unconventional superconductivity in iron arsenides.

Considering this generally accepted situation for  $\text{Ba}(\text{Fe}_{1-x}\text{Co}_x)_2\text{As}_2$ , it is particularly important to clarify the intrinsic behavior of  $\text{Ba}_{1-x}\text{K}_x\text{Fe}_2\text{As}_2$ , also because cobalt doping causes additional disorder in the  $(\text{Fe}_{1-x}\text{Co}_x)\text{As}$  layers, while potassium doping hardly affects the FeAs layers. Thus, if both orders coexist microscopically in  $\text{Ba}_{1-x}\text{K}_x\text{Fe}_2\text{As}_2$ , we rather observe the behavior of the clean superconducting FeAs layer. Indeed, a recent neutron diffraction study with polycrystalline material supports early suggestions about microscopic coexistence<sup>[79]</sup>, but gives no conclusive proof, because elastic neutron scattering as a bulk probe is principally unable to distinct whether the magnetic volume fraction or the magnetic moment at the iron site decreases.

In this chapter, a combined high-resolution X-ray diffraction and muon spin rotation  $\mu\text{SR}$  study with underdoped  $\text{Ba}_{1-x}\text{K}_x\text{Fe}_2\text{As}_2$  ( $x = 0, 0.19, 0.23, 0.25$ ) is reported. The homogeneous coexistence of the superconducting and antiferromagnetic phase and the competition of the respective order parameters are unambiguously shown.

### 3.2 Synthesis

Polycrystalline samples of  $\text{Ba}_{1-x}\text{K}_x\text{Fe}_2\text{As}_2$  ( $x = 0, 0.19, 0.23, 0.25$ ) were synthesized by heating stoichiometric mixtures of the elements (purities > 99.9 %) in alumina crucibles sealed in silica tubes under purified argon as described in chapter 7.3. Lattice parameters were obtained by temperature-dependent X-ray powder diffraction (Co-, Cu-, Mo- $\text{K}\alpha_1$ -radiation) and Rietveld refinements using the TOPAS package<sup>[51]</sup>. Figure 3-1 shows a typical XRD pattern. Only traces of impurity phases were detected. Ba/K ratios were examined by refinement of the site occupancy parameters and cross-checked by ICP-AAS chemical analysis.  $\mu\text{SR}$  measurements have been performed using the GPS and Dolly spectrometers. The data have been analyzed using the MUSRFIT package<sup>[58]</sup>.

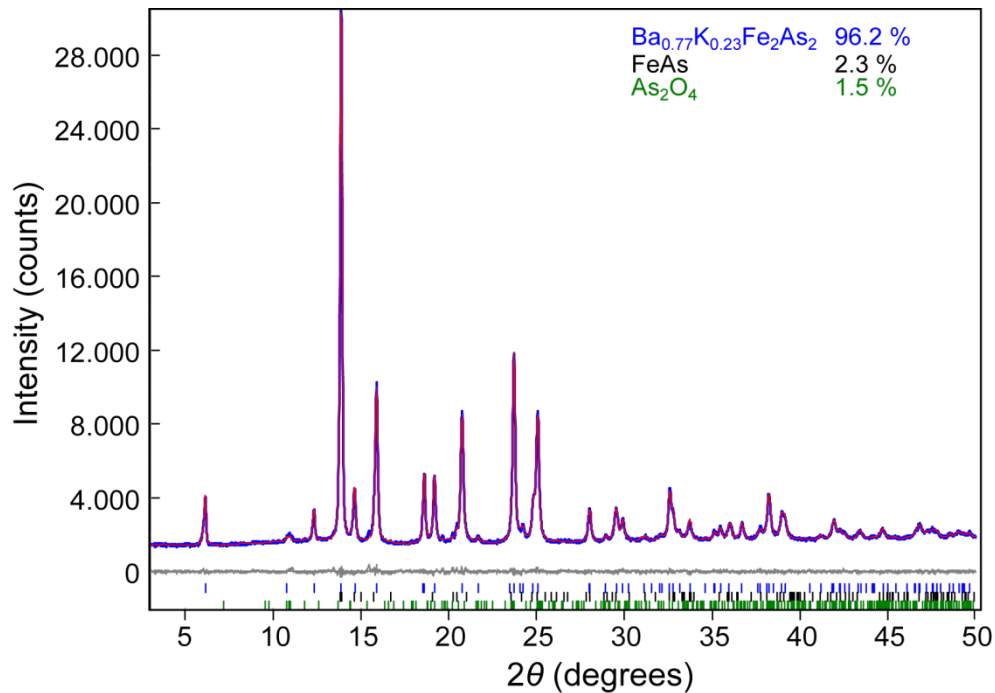


**Figure 3-1:** X-ray powder diffraction pattern (blue) and Rietveld fit (red) of  $\text{Ba}_{1-x}\text{K}_x\text{Fe}_2\text{As}_2$  ( $x = 0.23$ ).

X-ray powder patterns of the samples revealed the known structural phase transitions from tetragonal to orthorhombic symmetry. In agreement with earlier studies<sup>[42]</sup>, also

[79] showed that the orthorhombic distortion depends on the potassium concentration and is finally absent if  $x \geq 0.3$ . Figure 3-2 shows the temperature dependency of the 112 reflections. While the clear splitting, or at least broadening of the peak is visible at  $x = 0.19$  and  $0.23$ , it is apparently absent at  $x = 0.25$ . However, a closer inspection reveals the onset of peak broadening below  $\sim 70$  K also in this case. From this we obtained the tetragonal to orthorhombic transition temperatures  $T_s = 140$  K,  $98$  K,  $84$  K and  $70$  K for  $x = 0, 0.19, 0.23$ , and  $0.25$ , respectively.

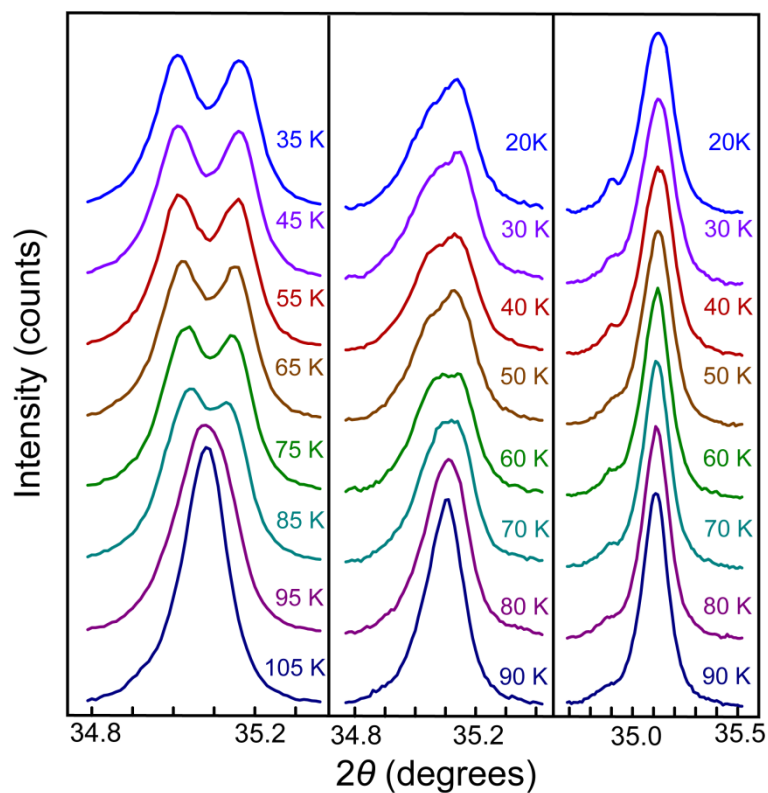


**Figure 3-2: Temperature dependence of the 112 reflections of for  $x = 0.19, 0.23$ , and  $0.25$ .**

The lattice parameters obtained from Rietveld refinements are shown in Figure 3-3. The continuous splitting indicates that the transitions are likely second order at least in the doped samples. This has also been suggested for the undoped parent compound<sup>[27, 80]</sup>. It is obvious that potassium doping of  $\text{BaFe}_2\text{As}_2$  reduces the

transition temperature  $T_s$  and also the extent of the lattice parameter splitting, which is still visible at  $x = 0.25$  where  $T_c$  is already 32.6 K.

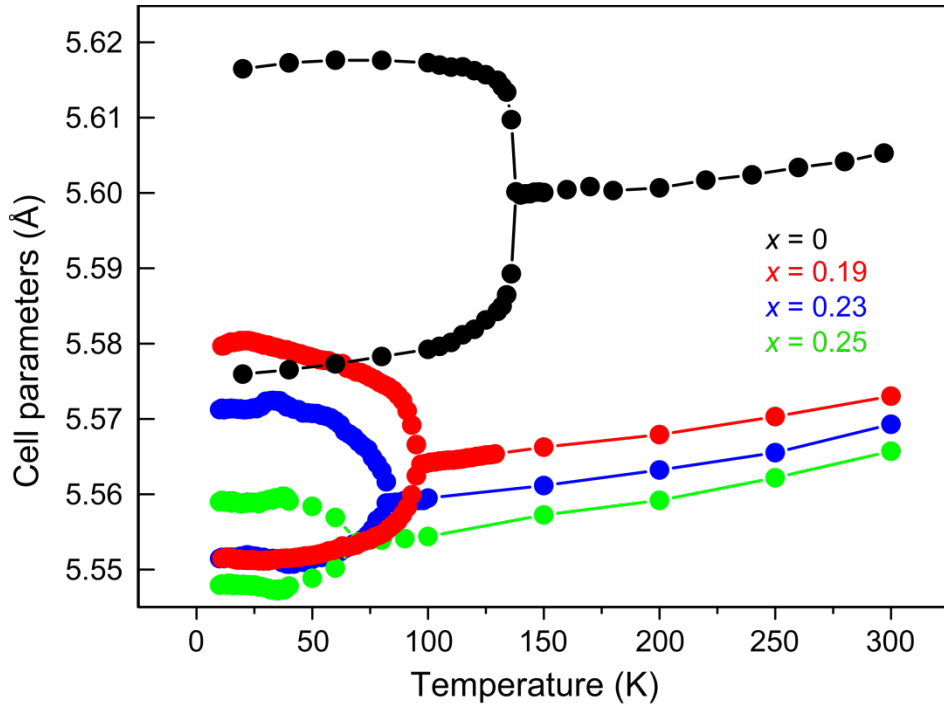
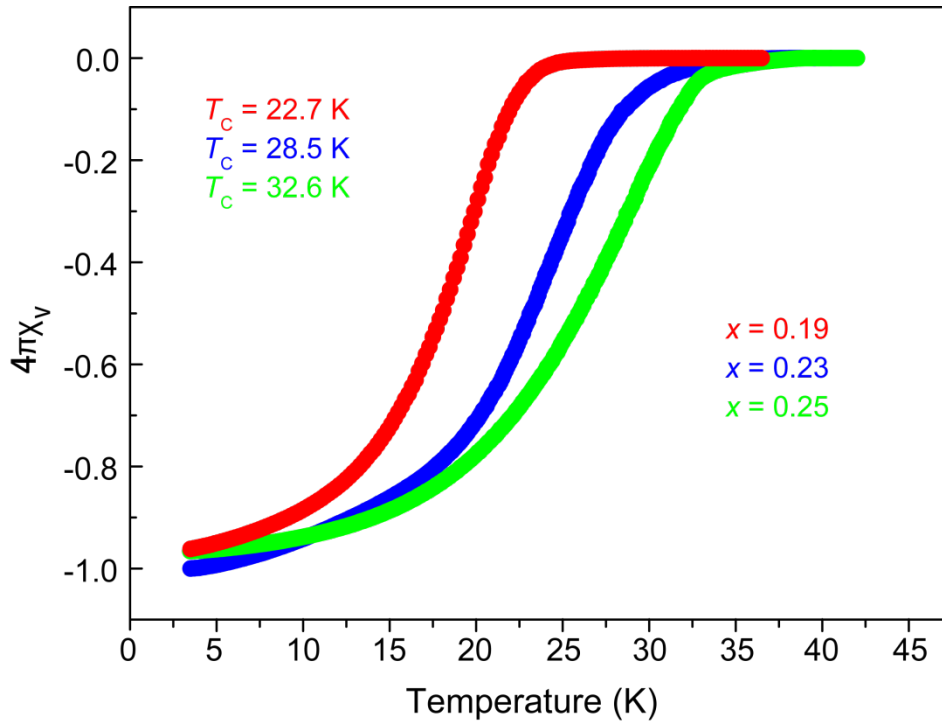


Figure 3-3: *a*- and *b*-axis cell parameters as a function of temperature obtained from Rietveld refinements of the different samples.

### 3.3 Results and discussion

#### 3.3.1 AC susceptibility

Diamagnetic signals were detected below  $T_c = 22.7$  K ( $x = 0.19$ ), 28.5 K ( $x = 0.23$ ) and 32.6 K ( $x = 0.25$ ) as shown in Figure 3-4. The superconducting volume fractions of all samples are close to 100 % and prove bulk superconductivity.



**Figure 3-4:** Magnetic susceptibility measurement of  $\text{Ba}_{1-x}\text{K}_x\text{Fe}_2\text{As}_2$  with  $x = 0.19$ ,  $0.23$ , and  $0.25$  showing  $\sim 100\%$  diamagnetic shielding.

### 3.3.2 Muon spin rotation and relaxation

Muon spin rotation measurements in a weak transverse field (wTF- $\mu$ SR) provide an easy means to measure the magnetic volume fraction. In Figure 3-5 the magnetic volume fractions obtained by such measurements in  $H_{\text{ext}} = 50$  Oe are shown for various  $\text{Ba}_{1-x}\text{K}_x\text{Fe}_2\text{As}_2$  samples ( $x = 0, 0.19$ , and  $0.23$ ) as a function of temperature. For all samples a transition to a magnetic state is observed. From this the magnetic transition temperature, where 50 % of the volume is magnetic, has been determined to  $T_N^{50\%} = 138$  K, 97 K, and 83 K for the three samples, respectively, which are very close to the structural transition temperatures  $T_s$ . The magnetic volume fraction reaches 100 % for all three samples and, most remarkable, does not change below the superconducting  $T_c$ .

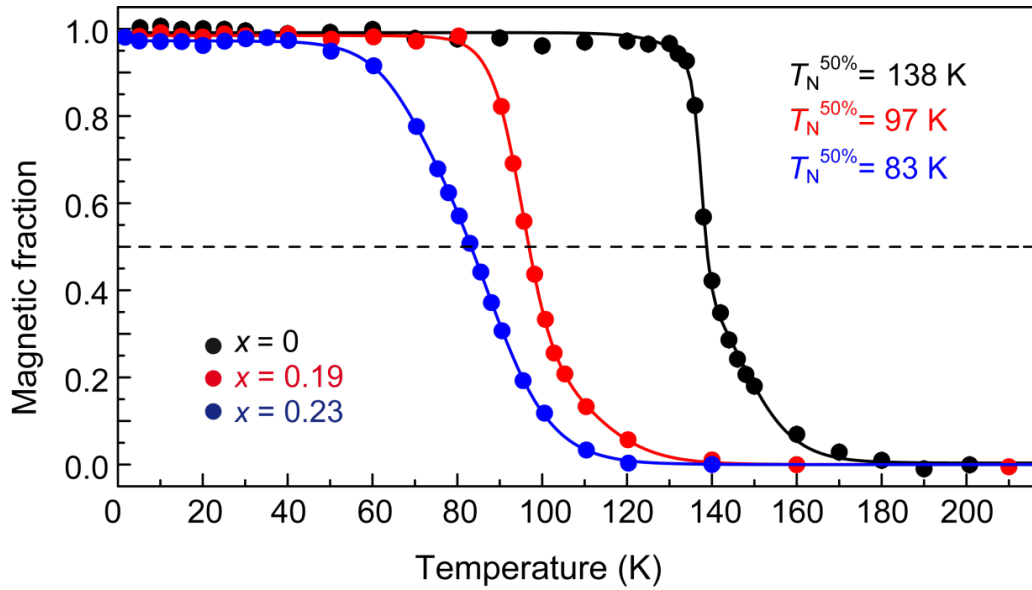


**Figure 3-5:** Magnetic volume fraction as a function of temperature, obtained from wTF- $\mu$ SR measurements.

Therefore, these results, together with the 100 % superconducting shielding signal observed in the AC susceptibility measurements, prove the microscopic coexistence of magnetism and superconductivity in the orthorhombic phase of the samples. The structural, magnetic, and superconducting transition temperatures are compiled in the phase diagram depicted in Figure 3-6.

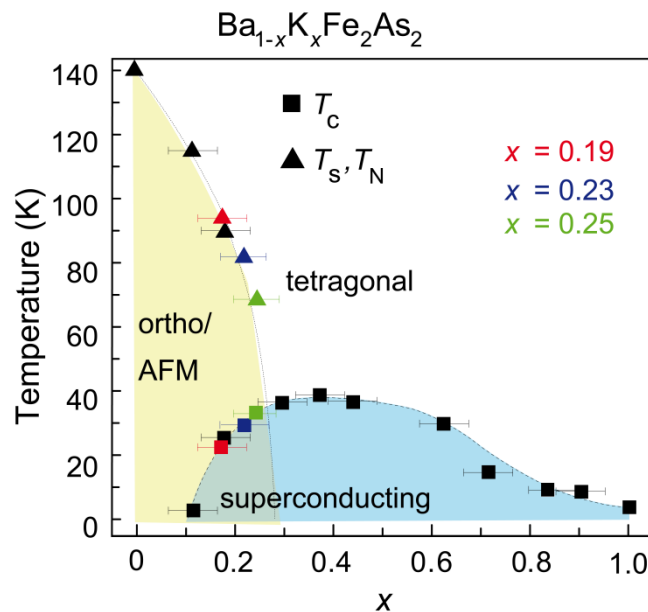


**Figure 3-6:** Structural, magnetic, and superconducting phase diagram of  $\text{Ba}_{1-x}\text{K}_x\text{Fe}_2\text{As}_2$ .

The orthorhombic distortion in terms of the structural order parameter  $\delta = (a-b)/(a+b)$  is shown in (Figure 3-7a). In the  $x = 0.19$  sample,  $\delta$  achieves a clear maximum  $\delta_{\text{max}} \approx 27 \times 10^{-4}$  at the superconducting transition temperature close to 23 K and then decreases to lower temperatures. Higher potassium concentrations further decrease  $T_s$  to 84 K while  $\delta_{\text{max}} \approx 20 \times 10^{-4}$  again coincides with  $T_c$  at 28.5 K ( $x = 0.23$ ). This trend continues to  $x = 0.25$  with  $T_s \approx 70$  K,  $T_c = 32.6$  K, and  $\delta_{\text{max}} \approx 13 \times 10^{-4}$ . This behavior is similar to  $\text{Ba}(\text{Fe}_{1-x}\text{Co}_x)_2\text{As}_2$ <sup>[28]</sup>, however, we do not observe the further linear decrease of  $\delta$  at lower temperatures back to a quasi-tetragonal structure, but rather saturation of  $\delta$ . Also in contrast to the cobalt-doped material, the effect becomes smaller with increasing potassium concentrations  $x$ . The reason for that is not yet clear. The stronger effect in the case of cobalt doping may be connected with the fact that magnetic ordering is weakened not only by the electron doping, but additionally by the disorder that is introduced by the cobalt atoms at the iron sites. Thus the competition of superconductivity and antiferromagnetism for the same electrons may affect the  $(\text{Fe}_{1-x}\text{Co}_x)\text{As}$  layers more efficiently than the clean  $\text{FeAs}$  layers in the potassium-doped material.

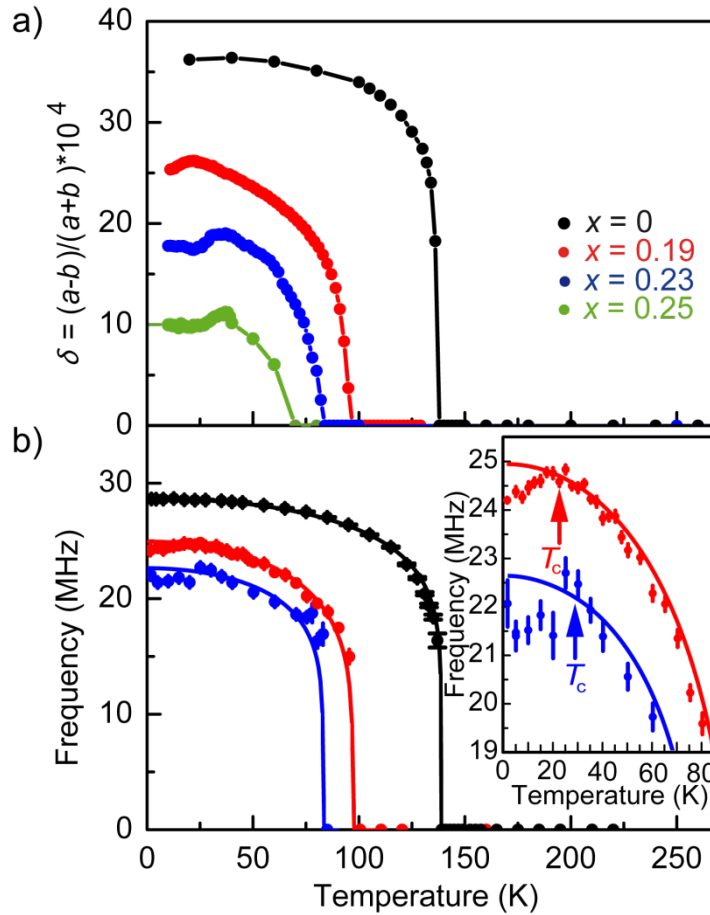


**Figure 3-7: Orthorhombicity parameter  $\delta$  and ZF- $\mu$ SR frequency (magnetic order parameter) of  $\text{Ba}_{1-x}\text{K}_x\text{Fe}_2\text{As}_2$  as a function of temperature.**

To elucidate further the magnetic properties of  $\text{Ba}_{1-x}\text{K}_x\text{Fe}_2\text{As}_2$  zero field (ZF-)  $\mu$ SR measurements have been performed. The ZF- $\mu$ SR spectra shown in Figure 3-8 exhibit well defined muon spin precessions below  $T_N$ . The increased damping of the precession indicates a decreased level of magnetic homogeneity throughout the sample. Anyhow, the observation of a spontaneous  $\mu$ SR precession is the signature of a long-range magnetically ordered phase even at  $x = 0.23$ .

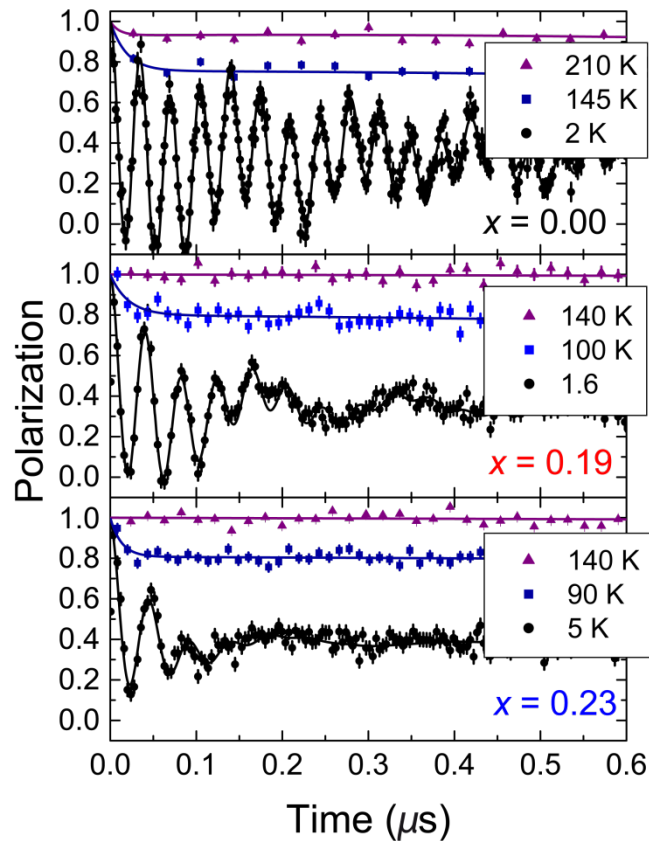


**Figure 3-8:** Zero field  $\mu\text{SR}$  spectra for characteristic temperatures (above, at, and below the transition) for  $\text{Ba}_{1-x}\text{K}_x\text{Fe}_2\text{As}_2$  powder samples with  $x = 0.0, 0.19,$  and  $0.23$ .

As already observed in other Fe-based superconductors<sup>[74, 81-82]</sup>, the ZF spectra are composed of two distinct precession frequencies, which is clearly visible from the beating of the time domain data in Figure 3-8. This has been interpreted as two magnetically inequivalent muon stopping sites in the structure. The data can be well fitted with two damped cosine functions and a non-relaxing longitudinal tail with an amplitude of  $1/3$ . This is the fingerprint of a commensurate magnetic structure, which is static on a time scale of  $\mu\text{SR}$ <sup>[83]</sup>. Note that in underdoped samples of the related  $\text{Ba}(\text{Fe}_{1-x}\text{Co}_x)_2\text{As}_2$  family only a strongly overdamped oscillation can be observed<sup>[84-85]</sup>. This indicates that the doping in the barium layer causes considerably less disorder in the magnetic system. Another difference is that in the cobalt-doped systems  $\mu\text{SR}$  spectra consistent with incommensurate order have been found. ZF- $\mu\text{SR}$  allows us to precisely determine the temperature dependence of the magnetic order parameter (Fe moment) which is proportional to the measured  $\mu\text{SR}$  frequency. The higher one

of the two observed  $\mu\text{SR}$  frequencies is shown in Figure 3-7b together with the orthorhombicity parameter  $\delta = (a-b)/(a+b)$  deduced from the XRD measurements (Figure 3-7a).

The magnetic order parameter shown in Figure 3-7b decreases alike the orthorhombicity as a function of potassium doping. Most remarkable, however, is the decrease of the magnetic order parameter (Fe moment) below the superconducting  $T_c$  clearly visible in the inset of Figure 3-7b. It should be mentioned that  $\mu\text{SR}$  as a local probe is able to measure the magnetic volume fraction (Figure 3-5) and the size of the ordered moment (via the ZF- $\mu\text{SR}$  frequency) separately unlike it is done in scattering experiments where the product of both quantities is measured. Taking all data together it is obvious that all investigated samples remain 100 % magnetic, but that the ordered Fe magnetic moment as well as the orthorhombicity decrease below the superconducting  $T_c$ . In other words, superconductivity and magnetism coexist on a microscopic scale, but compete for the same electrons in the underdoped region of the  $\text{Ba}_{1-x}\text{K}_x\text{Fe}_2\text{As}_2$  phase diagram.

### 3.4 Conclusion

In summary, these results prove the paradigm of phase separation in underdoped  $\text{Ba}_{1-x}\text{K}_x\text{Fe}_2\text{As}_2$  wrong. Instead compelling evidence of microscopic coexistence of superconductivity with magnetic ordering is found from combined X-ray and  $\mu\text{SR}$  data. The competition for the same electrons reduces the magnetic moment below  $T_c$ , while the magnetic fraction remains 100 % according to volume-sensitive  $\mu\text{SR}$  measurements. The response of the structural and magnetic order parameters at  $T_c$  is weaker than in cobalt-doped  $\text{Ba}(\text{Fe}_{1-x}\text{Co}_x)_2\text{As}_2$ . Since potassium doping introduces no disorder in the superconducting FeAs layer, it can be suggested that we rather observe its intrinsic behavior.

## 4 Short-range magnetic order in $\text{Ba}_{1-x}\text{K}_x\text{Fe}_2\text{As}_2$

### 4.1 Introduction

The proximity of superconducting and magnetic areas in the phase diagrams of iron arsenides led to the idea that magnetic fluctuations may play an important role in an unconventional pairing mechanism<sup>[86-88]</sup>. In fact superconductivity coexists with the antiferromagnetic orthorhombic phases in the underdoped areas of electron-doped  $\text{Ba}(\text{Fe}_{1-x}\text{Co}_x)_2\text{As}_2$ <sup>[28]</sup> as well as in hole-doped  $\text{Ba}_{1-x}\text{K}_x\text{Fe}_2\text{As}_2$ <sup>[89]</sup>. Resistivity measurements with detwinned crystals revealed anisotropies much larger than the lattice distortions<sup>[90]</sup>. This suggested the existence of a magnetic nematic state as earlier predicted<sup>[91]</sup>, which breaks the C4 symmetry of the electronic structure even if the crystal lattice remains tetragonal<sup>[92]</sup>. The nematic phase encompasses the boundary between the para- and antiferromagnetic area. Recently refined phase diagrams of the 122-type compounds revealed even higher complexity. Small pockets of tetragonal phases have been found inside the orthorhombic areas of underdoped  $\text{Ba}_{1-x}\text{Na}_x\text{Fe}_2\text{As}_2$  by neutron diffraction<sup>[93-94]</sup> and in  $\text{Ba}_{1-x}\text{K}_x\text{Fe}_2\text{As}_2$  by thermal expansion and specific heat experiments<sup>[95]</sup>.

Less attention has been paid to the optimal and overdoped areas of the  $\text{Ba}_{1-x}\text{K}_x\text{Fe}_2\text{As}_2$  phase diagram. Earlier  $\mu\text{SR}$ - and NMR-studies of single crystals with  $x = 0.4 - 0.55$  (nearly optimal doping) indicated fractions of static magnetism with incommensurate or short-range order coexisting with superconductivity, and claimed the existence of mesoscopic phase separations<sup>[73-76]</sup>. On the other hand, polycrystalline samples of  $\text{Ba}_{1-x}\text{K}_x\text{Fe}_2\text{As}_2$  with  $x$  up to 0.25 exhibit reductions of the magneto-elastically coupled magnetic moments below  $T_c$  with magnetic volume fractions of 100 %, proving microscopic coexistence of superconducting and the magnetic order parameter<sup>[89]</sup>.

Thus, in order to clarify how magnetism and superconductivity interact in  $\text{Ba}_{1-x}\text{K}_x\text{Fe}_2\text{As}_2$  over a larger range of the phase diagram, whether magnetic signatures exist in optimally and overdoped polycrystalline  $\text{Ba}_{1-x}\text{K}_x\text{Fe}_2\text{As}_2$ , and where

the change of the superconducting wave function occurs, X-ray, AC susceptibility, and  $\mu\text{SR}$  measurements have been performed on different samples with  $0 \leq x \leq 0.66$ .

## 4.2 Synthesis

The polycrystalline samples of  $\text{Ba}_{1-x}\text{K}_x\text{Fe}_2\text{As}_2$  ( $x = 0, 0.19, 0.23, 0.27, 0.31, 0.4, 0.5, 0.6, 0.66$ ) were synthesized by heating stoichiometric mixtures of the elements (purities  $> 99.9\%$ ) in alumina crucibles sealed in silica tubes under an atmosphere of purified argon as described in chapter 7.3. All compounds could be obtained as the main phase with small reflection full widths at half maximum. Only small fractions of the impurity phase FeAs are visible due to the potassium evaporation. The impurity phase could be detected especially in the highest-doped compound (FeAs  $\geq 8.5\text{ wt}\%$  for  $x = 0.66$ ). In the lower-doped compounds ( $x < 0.66$ ) the amount of FeAs is smaller or even absent. The lattice parameters were obtained by X-ray powder diffraction (Cu/Co- $K_{\alpha 1}$ -radiation) and Rietveld refinements using the TOPAS package<sup>[52]</sup>. A representative powder pattern and its Rietveld fit showing no impurity phase is depicted in Figure 4-1.

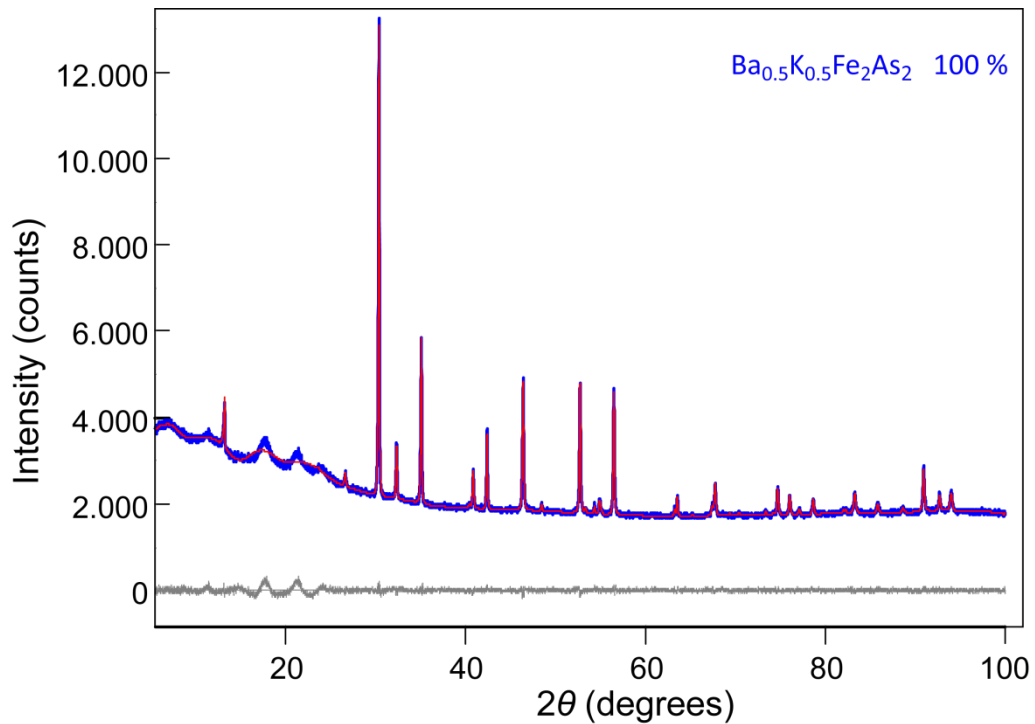


**Figure 4-1:** X-ray powder diffraction pattern (blue) and Rietveld fit (red) of  $\text{Ba}_{0.5}\text{K}_{0.5}\text{Fe}_2\text{As}_2$ .

The two broad signals around  $20^\circ 2\theta$  are measurement artifacts.

The Ba/K ratio was examined by refinement of the site occupancy parameters, ICP-AAS, superconducting transition temperature and cross checked with [42].

## 4.3 Results and discussion

### 4.3.1 Susceptibility

The susceptibility measurements and superconducting transition temperatures are shown in Figure 4-2. The broad superconducting transition for the  $x = 0.66$  sample can probably be attributed to a less homogeneous potassium distribution compared to the other samples. The superconducting volume fraction of all samples is above 75 % and proves bulk superconductivity in all samples.

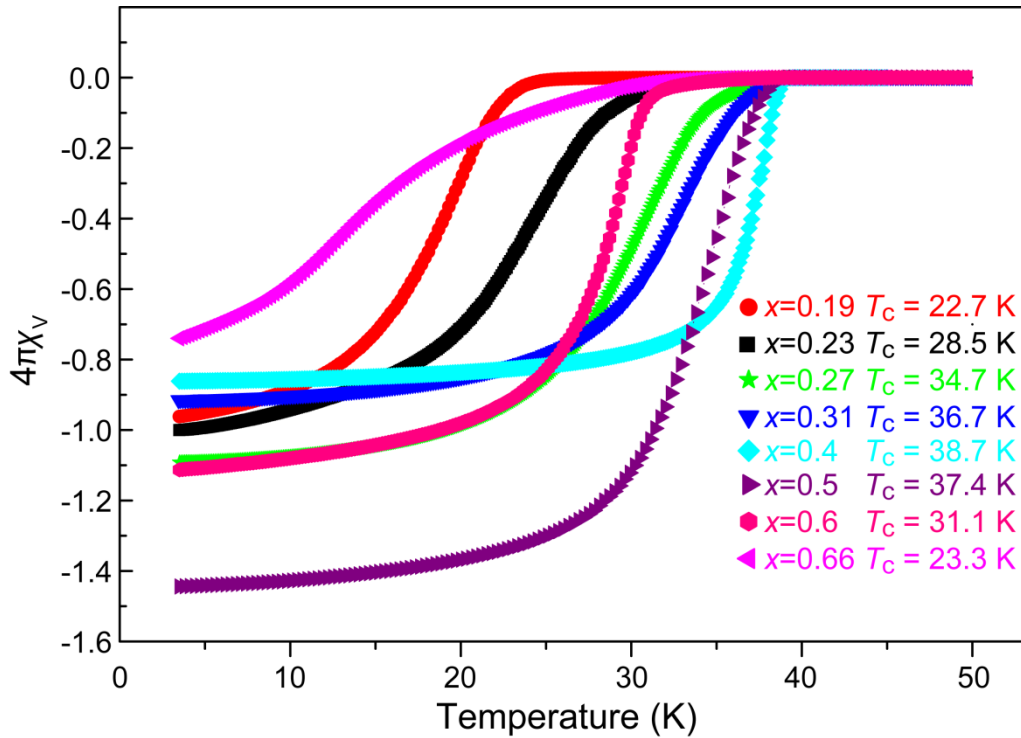


**Figure 4-2:** Susceptibility measurements of all investigated samples of  $\text{Ba}_{1-x}\text{K}_x\text{Fe}_2\text{As}_2$  ( $0.19 \leq x \leq 0.66$ ).

### 4.3.2 Moun spin rotation and relaxation

The polarization data is plotted in Figure 4-3. We see a clear decrease of the polarization at low temperatures ( $T < 5$  K) with increasing potassium content. Up to  $x = 0.27$  the muon oscillation is still visible representing long-range magnetic order (Figure 4-3). At  $x = 0.31$  a distinct polarization still occurs but without oscillation, representing a transition to short-range magnetic order. In  $\text{Ba}_{0.6}\text{K}_{0.4}\text{Fe}_2\text{As}_2$  and higher-doped compounds the polarization at 5 K is further reduced. Remarkably, in contrast to common belief the short-range magnetic order remains existent up to  $x = 0.66$ .

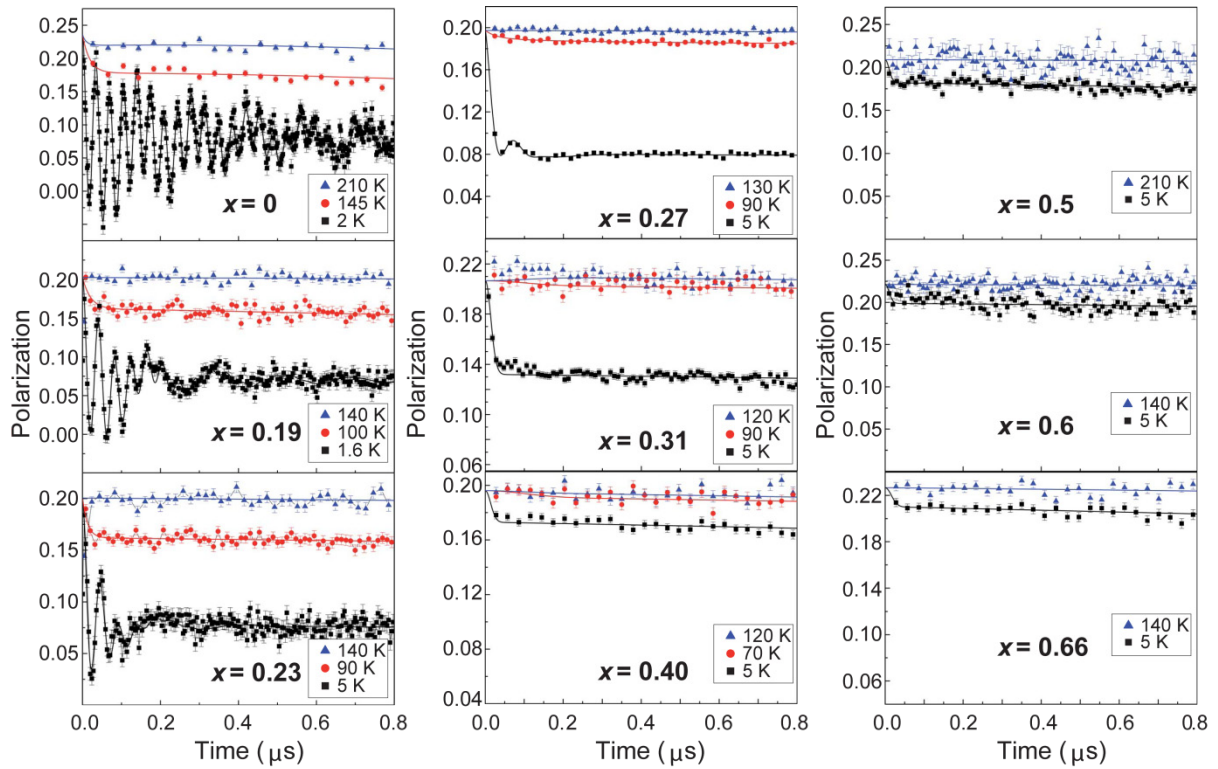


**Figure 4-3: Results of the zero field polarization measurements of all investigated  $\text{Ba}_{1-x}\text{K}_x\text{Fe}_2\text{As}_2$  ( $0 \leq x \leq 0.66$ ) samples at different temperatures.**

In Figure 4-4 the magnetic volume fractions obtained by wTF- $\mu$ SR measurements with  $H_{\text{ext}} = 50$  Oe are displayed as a function of temperature. For all samples magnetic fractions are observed even though only samples with  $x \leq 0.23$  become 100 % magnetic. As mentioned before, in the area between  $0.14 \leq x \leq 0.25$  superconductivity and long-range ordered antiferromagnetism coexist on a microscopic scale.

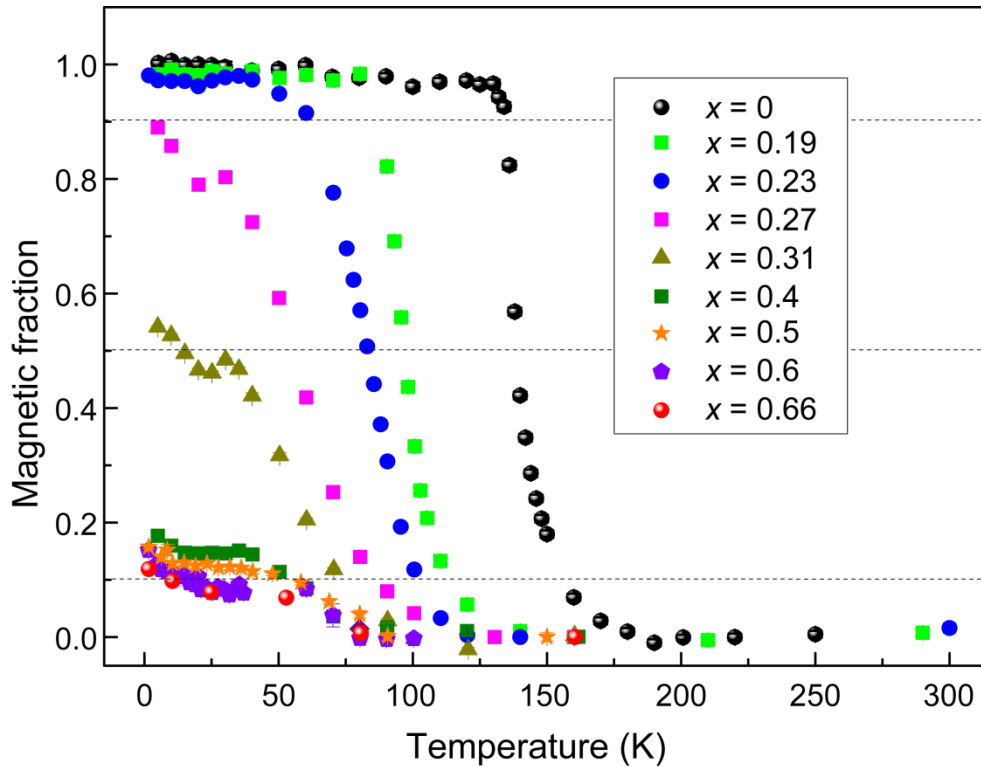


**Figure 4-4:** Magnetic volume fractions obtained from  $w\text{TF-}\mu\text{SR}$  measurements of different  $\text{Ba}_{1-x}\text{K}_x\text{Fe}_2\text{As}_2$  ( $0 \leq x \leq 0.66$ ) samples.

For undoped  $\text{BaFe}_2\text{As}_2$  an evolution of the magnetic volume fraction is found below 160 K, more than 20 K above the evolution of the long-range antiferromagnetic order at 138 K. These nematic fluctuations arise when the spins are already pre-ordered because of the low temperature, but still have enough energy to precess around their final condensed state. They are visible up to at least  $x = 0.4$ , suggesting a close tie to superconductivity<sup>[96]</sup>. The magnetic volume fraction<sup>[96]</sup> of higher-doped compounds ( $x > 0.23$ ) decreases with rising potassium content as a consequence of the doping. Note the dips in the curves coinciding with the superconducting transition temperatures, which indicate competition of both magnetism and superconductivity for the same electrons<sup>[89]</sup>. Unexpectedly, magnetic volume fractions of 10 - 15 % clearly remain also at and above optimal doping ( $x \approx 0.4$ ). The magnetic volume fractions for  $x > 0.23$  suggest that a non-magnetic superconducting phase is separated from a phase with coexisting superconductivity and antiferromagnetically ordered clusters. The combination of a short-range order and a phase separation indicates a quantum critical point at  $x \approx 0.3$ . This effect was also observed for phosphorous-<sup>[97]</sup>, cobalt-<sup>[98]</sup> and nickel-doped<sup>[99]</sup>  $\text{BaFe}_2\text{As}_2$  near ideal doping. Unlike

common belief, magnetic ordering is not completely suppressed in  $\text{Ba}_{1-x}\text{K}_x\text{Fe}_2\text{As}_2$  as the superconducting transition temperature reaches its maximum for  $x = 0.4$ . A residual magnetic fraction emerges at 70 K. One may argue that the residual magnetic volume in the optimally and overdoped samples ( $x \geq 0.4$ ) may derive from FeAs impurities ( $T_N = 77 \text{ K}$ )<sup>[100]</sup>. The highest FeAs fractions from X-ray diffraction are 6 vol% at  $x = 0.66$  and 2 vol% at  $x = 0.6$ , while no FeAs was detected at  $x = 0.5$  and 0.4. However, the low-temperature magnetic volume decreases with increasing  $x$  which is just the reverse trend compared with the FeAs fraction. Furthermore the  $\mu\text{SR}$  depolarization signal of pure FeAs is still very weak at 70 K<sup>[100]</sup>, where the magnetic fraction is already significant in these data. From this it can be excluded that the remaining magnetism originates from FeAs.

By merging the data obtained from the susceptibility, X-ray, and the  $\mu\text{SR}$  measurements a color-coded phase diagram was created (Figure 4-5). Small magnetic fractions are measured up to unexpected high temperatures throughout the whole investigated range. Also, the temperatures of structural distortion, represented by  $T_N^{50\%}$  (yellow area of Figure 4-5), and the magnetic transition to the long-range ordered antiferromagnetic state (red area of Figure 4-5), are apparently drifting apart with increasing  $x$ . This is highlighting the influence of the short-range order. Comparing this phase diagram to others as found in [42] and [101] it becomes clear that the sharp borders, as drawn there, do not display the real interplay of structural, magnetic, and superconducting properties sufficiently, due to missing information about nematic and short-range ordered areas.

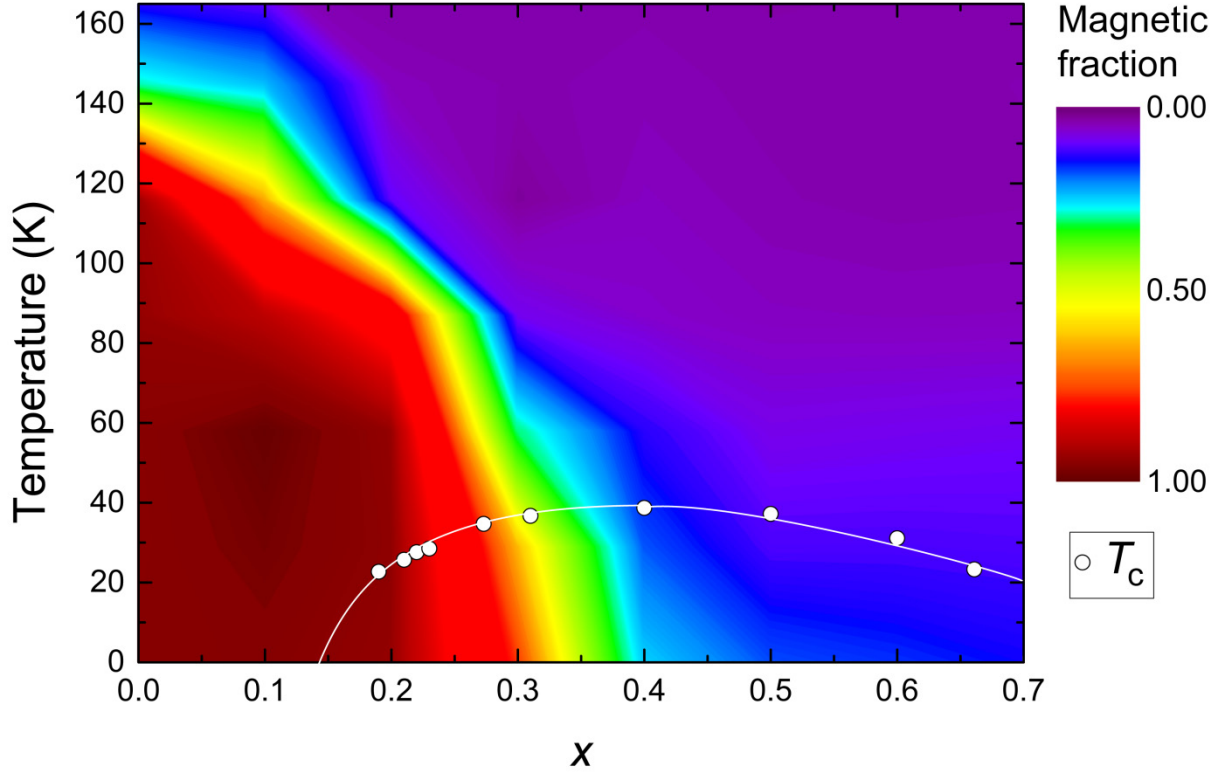


**Figure 4-5:** Color-coded phase diagram of  $\text{Ba}_{1-x}\text{K}_x\text{Fe}_2\text{As}_2$  ( $0 \leq x \leq 0.66$ ).

As discussed by *Thomale et al.*<sup>[41]</sup> a change of the superconducting wave function from  $s$ - to  $d$ -wave in highly overdoped  $\text{Ba}_{1-x}\text{K}_x\text{Fe}_2\text{As}_2$  can be assumed. Where this change actually occurs hasn't been finally resolved yet. The superfluid density ( $n_s$ ) represents the amount of cooper pairs and is related to the penetration depth  $\lambda$  by  $n_s/m^* \propto \sigma_{\text{SC}} \propto 1/\lambda^2$ <sup>[102]</sup>. The relaxation rate  $\sigma_{\text{SC}}$  can be determined by  $\mu\text{SR}$  and reveals information about the superconducting gap due to its progression. Muon relaxation rates in transverse fields show decreasing superfluid densities in overdoped samples ( $x = 0.5, 0.6$  and  $0.66$ ) (Figure 4-6), thus superconductivity of  $\text{Ba}_{1-x}\text{K}_x\text{Fe}_2\text{As}_2$  becomes weaker for  $x > 0.5$ . The data obtained with the  $x = 0.5$  and  $0.6$  samples fit well with an  $s+s$ -wave gap function, while  $x = 0.66$  doesn't show saturation at low temperatures indicating a possible  $d$ -wave gap. This is in line with photoemission experiments suggesting a change in the Fermi surface topology in overdoped  $\text{Ba}_{1-x}\text{K}_x\text{Fe}_2\text{As}_2$  at  $x = 0.7 - 0.9$ <sup>[103]</sup>.

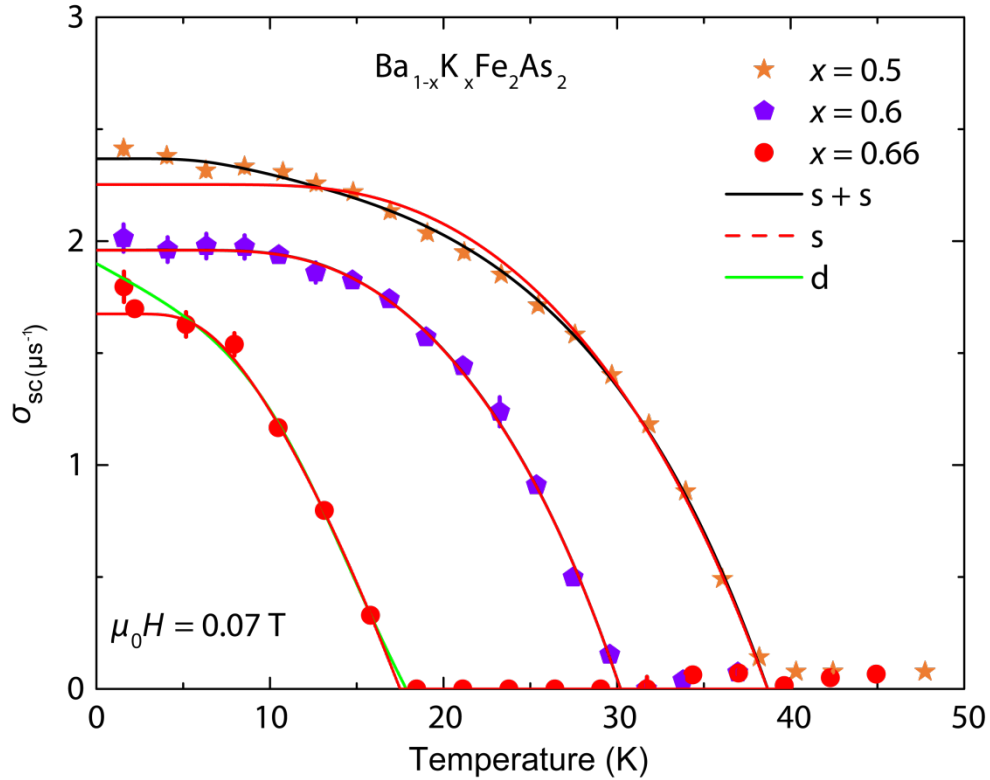


**Figure 4-6:** wTF- $\mu$ SR measurements of the superfluid density of  $\text{Ba}_{1-x}\text{K}_x\text{Fe}_2\text{As}_2$  ( $x = 0.5, 0.6, 0.66$ ). The black line represents an (s+s)-wave, the red dotted line an s-wave, and the green line a d-wave symmetry.

## 4.4 Conclusion

In summary, a color-coded phase diagram was presented, showing that the interplay of magnetism and superconductivity is more complicated than expected. Slow magnetic fluctuations prove a nematic phase preceding the evolution of magnetic order up to  $x = 0.4$ . The transition from a long-range to a short-range antiferromagnetic order takes place between  $0.27 > x > 0.31$ , emphasizing the fact that clear borders for the phase diagram of  $\text{Ba}_{1-x}\text{K}_x\text{Fe}_2\text{As}_2$  do not reflect the complete situation of the solid solution. In contrast to common belief, the region of short-range order exists at least up to  $x = 0.66$ . Furthermore, the competition of superconductivity and the antiferromagnetic order exceeds the point of phase separation at about  $x = 0.27$ . This is represented by dips in the magnetic volume fractions after passing  $T_c$ . The phases separate into a superconducting non-magnetic phase and a phase where superconductivity and antiferromagnetically ordered clusters coexist. By displaying short-range magnetic order and the phase separation

around  $x = 0.3$ , a quantum critical point is avoided<sup>[97]</sup>, an observation up to now not been measured in potassium-doped  $\text{BaFe}_2\text{As}_2$ . Superfluid density measurements for overdoped  $\text{Ba}_{1-x}\text{K}_x\text{Fe}_2\text{As}_2$  imply a transition from an (s+s)-wave into a *d*-wave gap function in samples with  $x \geq 0.6$ .

## 5 Rise of a new magnetic phase in $\text{Ba}_{0.8}\text{K}_{0.2}\text{Fe}_2\text{As}_2$

### 5.1 Introduction

The combination of different doping agents was a logic step in the investigation of  $\text{BaFe}_2\text{As}_2$ , in order to see how superconductivity and magnetism interact. In potassium and cobalt co-doped  $\text{BaFe}_2\text{As}_2$  the electron doping and the hole doping should compensate each other. This happens up to a certain doping level, but going beyond this point induces superconductivity until it completely vanishes together with the magnetic order at even higher doping levels<sup>[104]</sup>. In cobalt and phosphorous co-doped compounds the combination of both dopants leads to superconductivity at concentrations where only one doping agent wouldn't be sufficient<sup>[105]</sup>. Also, the combination of physical pressure and a dopant isn't new. For example  $\text{BaFe}_2\text{As}_2$  has been doped with ruthenium and physical pressure was applied to these samples<sup>[30]</sup>.

One topic that again takes a special position among these experiments is potassium doped  $\text{BaFe}_2\text{As}_2$  under pressure. *Hassinger et al.* observed the development of a new phase in underdoped  $\text{Ba}_{1-x}\text{K}_x\text{Fe}_2\text{As}_2$  ( $x = 0.16 - 0.21$ ) at pressures around 10 kbar<sup>[44]</sup>. But whether this new phase is magnetic or not, or what the magnetic structure looks like couldn't be conclusively determined.

Recently published results also show that the phase diagram of  $\text{Ba}_{1-x}\text{K}_x\text{Fe}_2\text{As}_2$  is more complicated than expected<sup>[95]</sup>. Narrow magnetic tetragonal phases for  $x = 0.24 - 0.28$  seem to exist alongside with the known antiferromagnetic and orthorhombic phase at low temperatures. The magnetic spins in these phases seem to align along the *c*-axis as in  $\text{Ba}_{1-x}\text{Na}_x\text{Fe}_2\text{As}_2$ <sup>[106]</sup>.

Thus one may think that this new phase at high pressure and the new tetragonal phases at ambient pressure could be the same. On the other hand the application of two different doping agents at the same time usually brought different results than one doping agent alone. In this chapter the interplay of magnetism and superconductivity in  $\text{Ba}_{0.8}\text{K}_{0.2}\text{Fe}_2\text{As}_2$  is investigated and the evolution of a new magnetic phase in  $\text{Ba}_{0.8}\text{K}_{0.2}\text{Fe}_2\text{As}_2$  is observed at pressures higher than 10 kbar on the expense of the existing magnetic order at ambient pressure. This new phase has

the same magnetic structure as the known phase at ambient pressure and is thus not identical to magnetic tetragonal phases at ambient pressure.

## 5.2 Synthesis

As the samples described in chapter 3 and 4,  $\text{Ba}_{0.8}\text{K}_{0.2}\text{Fe}_2\text{As}_2$  (1.5 g) was synthesized by heating stoichiometric mixtures of the elements (purities > 99.9 %) in alumina crucibles sealed in silica tubes under an atmosphere of purified argon, which is further described in chapter 7.3. Small fractions of the impurity phases  $\text{Ba}_3(\text{AsO}_4)_2$  and FeAs were detected due to potassium loss and traces of oxygen contamination. The lattice parameters and the purity were obtained by X-ray powder diffraction (Cu- $K_{\alpha 1}$ -radiation) and Rietveld refinement using the TOPAS package<sup>[51]</sup> and cross-checked by an ICP-AAS analysis. The powder pattern and its Rietveld fit are depicted in Figure 5-1.

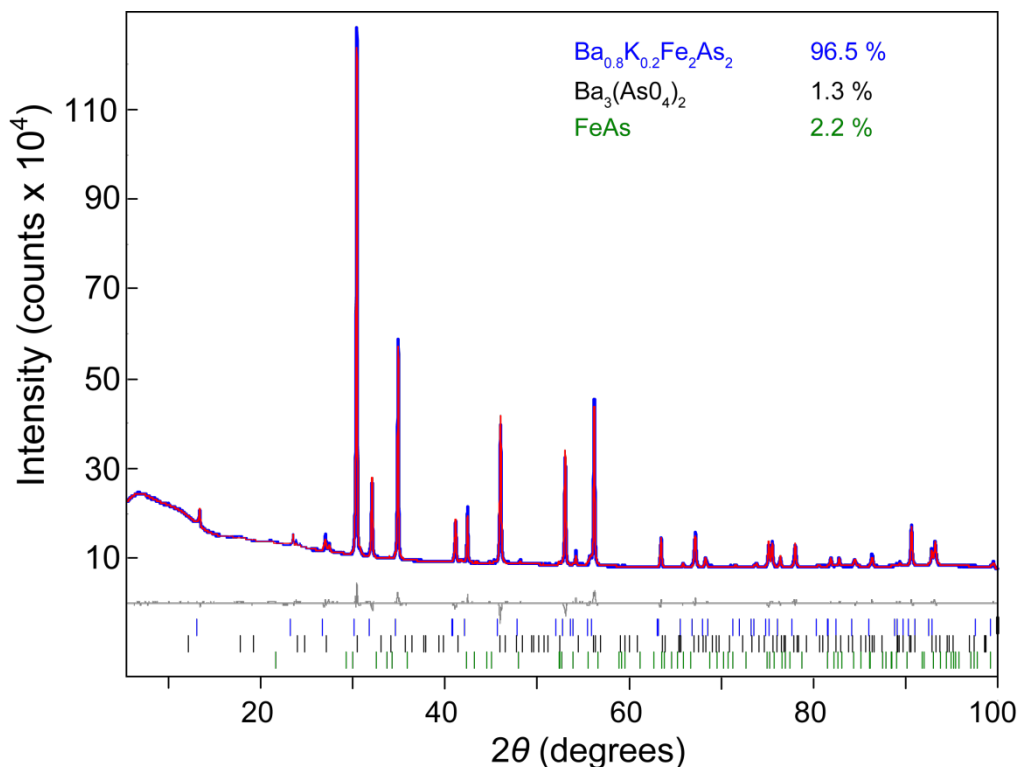
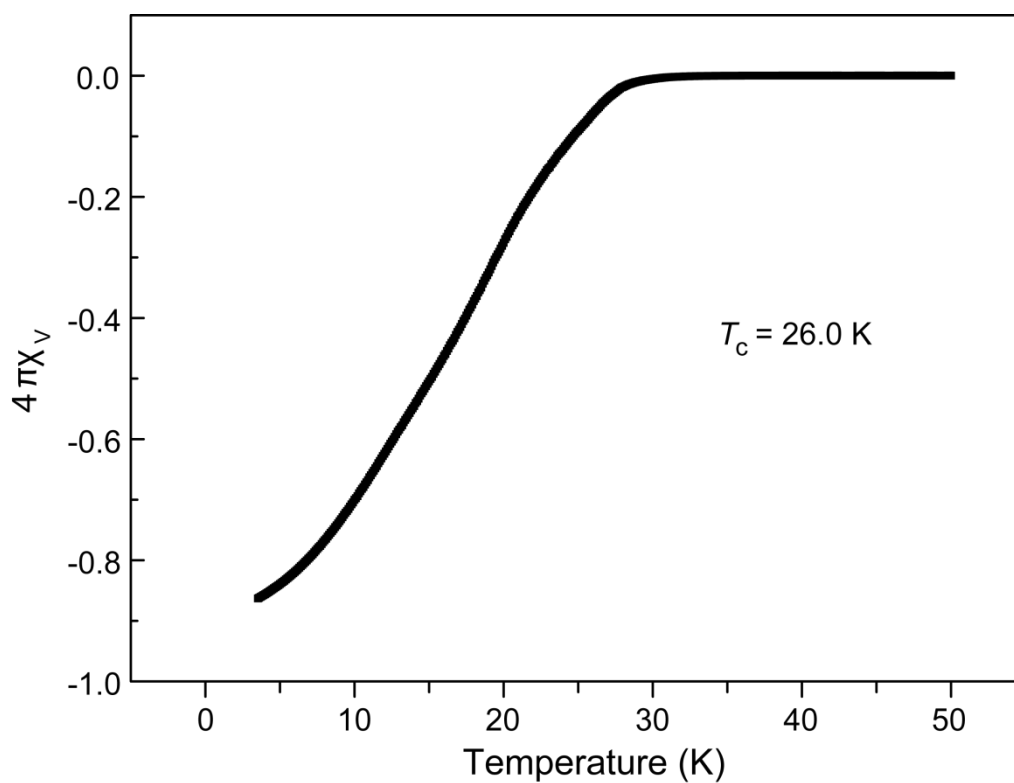


Figure 5-1: X-ray powder diffraction pattern (blue) and Rietveld fit (red) of  $\text{Ba}_{0.8}\text{K}_{0.2}\text{Fe}_2\text{As}_2$ .

## 5.3 Results and discussion

### 5.3.1 AC susceptibility

The susceptibility measurement and superconducting transition temperature are shown in Figure 5-2. The superconducting volume fraction of  $\text{Ba}_{0.8}\text{K}_{0.2}\text{Fe}_2\text{As}_2$  is about 87 %, proving bulk superconductivity, and is in good agreement with the Rietveld refinement.



**Figure 5-2:** Susceptibility measurement of  $\text{Ba}_{0.8}\text{K}_{0.2}\text{Fe}_2\text{As}_2$  at ambient pressure.

The superconducting transition under pressure was measured at several points up to 22.1 kbar in a diamond anvil cell and showed the same  $T_c$  (26 K) as the measurement at ambient pressure.

### 5.3.2 Muon spin rotation and relaxation

To perform the high pressure measurements, the sample was mixed with Daphne oil, pressed into pellets, and placed in a piston cylinder. The container was made out of *MP35*, an alloy chosen because of its non-magnetic behavior and its durability against pressure. Daphne oil was used as a pressure medium to obtain hydrostatic pressure<sup>[107]</sup>. The pressure was determined using the temperature shift of the superconducting temperature of an indium piece, that was also placed in the piston cylinder<sup>[108]</sup>.

At ambient pressure, the precession frequency of the muons rises below 110 K (Figure 5-3). With the frequency being proportional to the magnetic moment, this indicates the rise of the known stripe-type magnetic phase (AFM1) in  $\text{Ba}_{0.8}\text{K}_{0.2}\text{Fe}_2\text{As}_2$ .

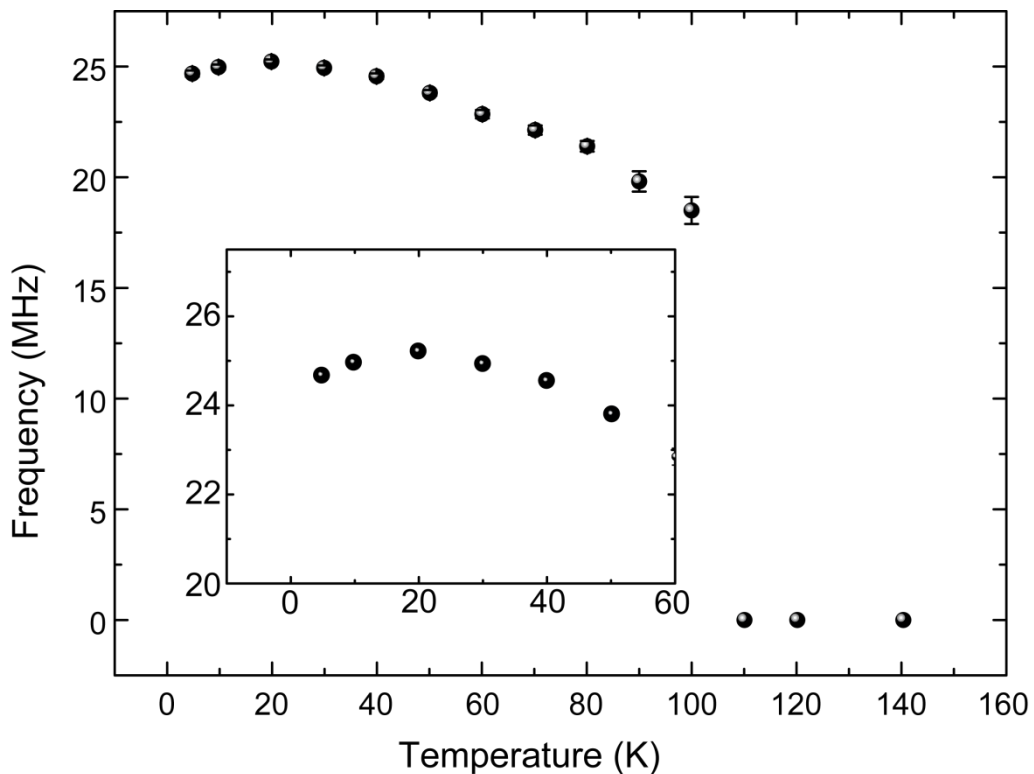


**Figure 5-3:** Magnetic order parameter of  $\text{Ba}_{0.8}\text{K}_{0.2}\text{Fe}_2\text{As}_2$  from ZF- $\mu$ SR data. Inset: Magnetic order parameter around the superconducting transition temperature.

The magnetic moment increases until  $T_c$  is reached. When passing the critical temperature it suddenly diminishes. This decrease of the magnetic moment can either be due to a reduction of the magnetic moment at each iron atom or the loss of the magnetic orientation at a portion of the spins. By looking at the magnetic volume fraction we can distinguish between these two options (Figure 5-4). It starts to rise below 140 K indicating the nematic phase, being described in chapter 4, that precedes the magnetic transition, which reaches its final state below 60 K with a magnetic volume fraction above 92 %. The missing magnetic volume fraction is probably a result of the existence of impurity phases. Furthermore, we can determine  $T_N^{50\%}$  with 107.1 K as the magnetic transition temperature.

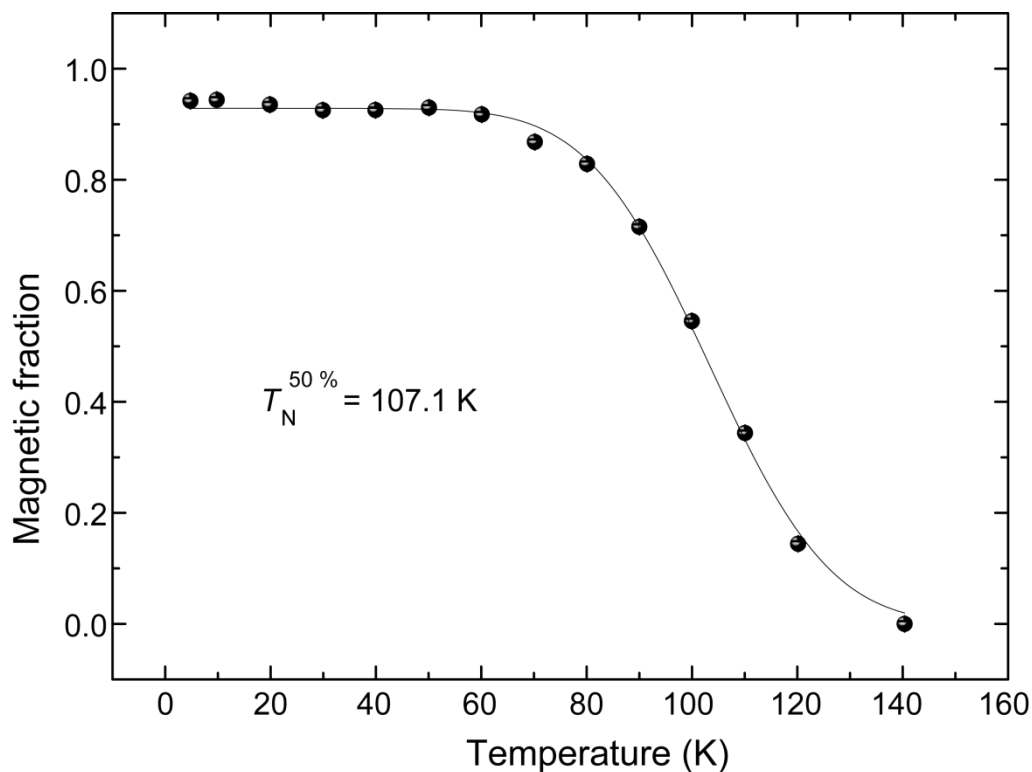


**Figure 5-4: Magnetic volume fraction of  $\text{Ba}_{0.8}\text{K}_{0.2}\text{Fe}_2\text{As}_2$  at ambient pressure measured via wTF-  $\mu$ SR.**

When positive muons are injected in the sample they tend to place themselves at highly symmetric places in a crystal with negative charge. In the case of  $\text{BaFe}_2\text{As}_2$  and the potassium doped compounds, two different muon frequencies are measured.

This indicates that, as proposed in chapter 3, there have to be two different muon sites.

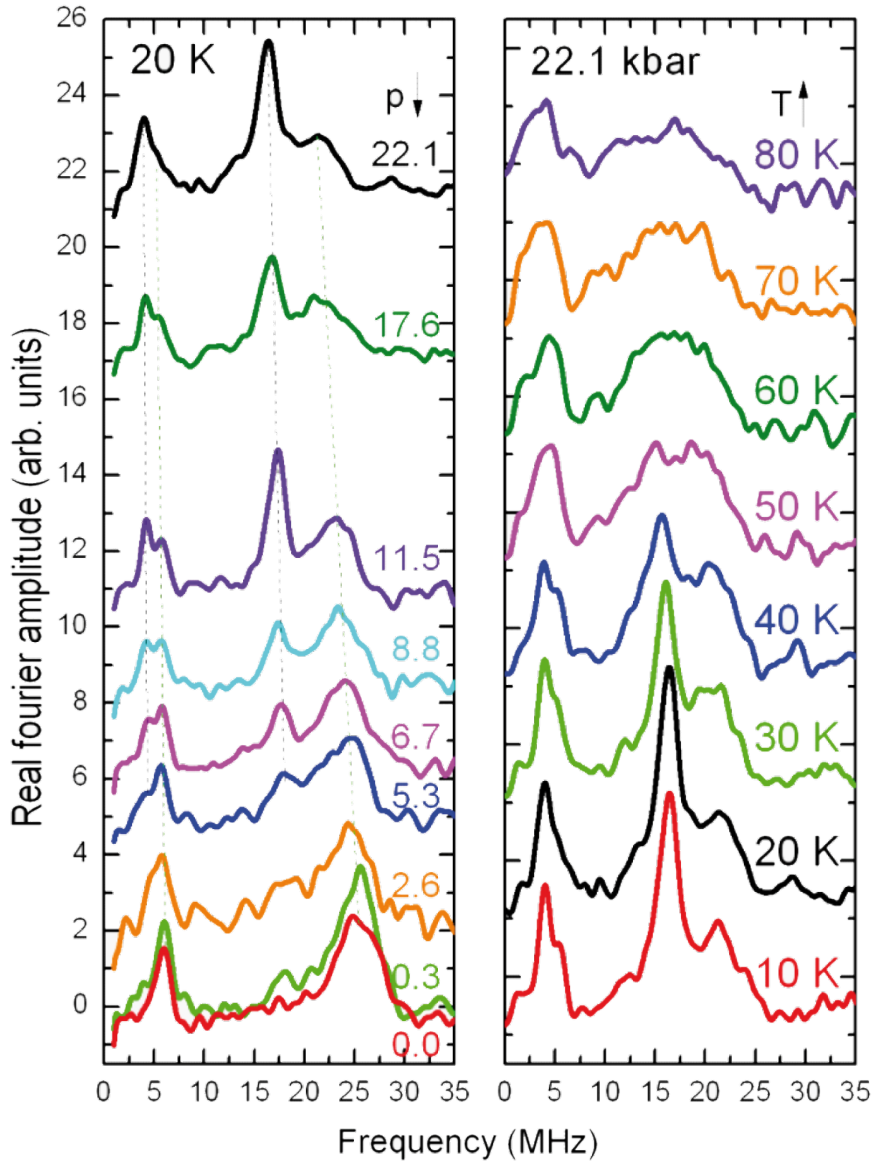


**Figure 5-5:** Fourier amplitude of the muon frequency. Left panel: At 20 K and different pressures. Right panel: At 22.1 kbar and different temperatures.

As can be seen in Figure 5-5, there are two peaks at frequencies of about 5 MHz and 25 MHz at 20 K with no external pressure applied (red line, left panel). These two frequencies represent the stripe-type magnetic order that we know from  $\text{BaFe}_2\text{As}_2$  already weakened by the partial substitution of barium with potassium. This magnetic

order is called AFM1. Under pressure the first observation is a broadening of the frequencies corresponding to AFM1 at 2.6 kbar. First traces of the new magnetic phase (AFM2) can also be assumed there but the new order becomes clearly visible at 5.3 kbar. It can be unambiguously distinguished from AFM1, as both phases have their own distinct volume. Also, the constant ratio of  $\sim 5$  between the higher and the lower frequency in AFM1 and AFM2 indicates that both phases have the same spin structure, whereby the magnetic moments are smaller in AFM2. A change in the spin structure would change the magnetic environment of the muons, causing them to choose new positions in the structure, and therefore lead to a different frequency ratio. With rising pressure the new phase becomes more and more pronounced. At the same time the known antiferromagnetic phase AFM1 is shifted to smaller frequencies and diminishes, but both magnetic orders are existent up to maximum pressure. On the right panel in Figure 5-5 the temperature-dependent evolution of the new magnetic phase at 22.1 kbar is shown. At 10 K peaks from both AFM1 and AFM2 can be seen. With increasing temperature the AFM1 peaks are broadened and starting from 40 K also AFM2 is unambiguously weakened and disappears above 50 K. The humps representing AFM1 remain basically unchanged up to 80 K and AFM1 is in fact detected up to 95.5 K.

The data are combined to a pressure dependent phase diagram of  $\text{Ba}_{0.8}\text{K}_{0.2}\text{Fe}_2\text{As}_2$  shown in Figure 5-6.

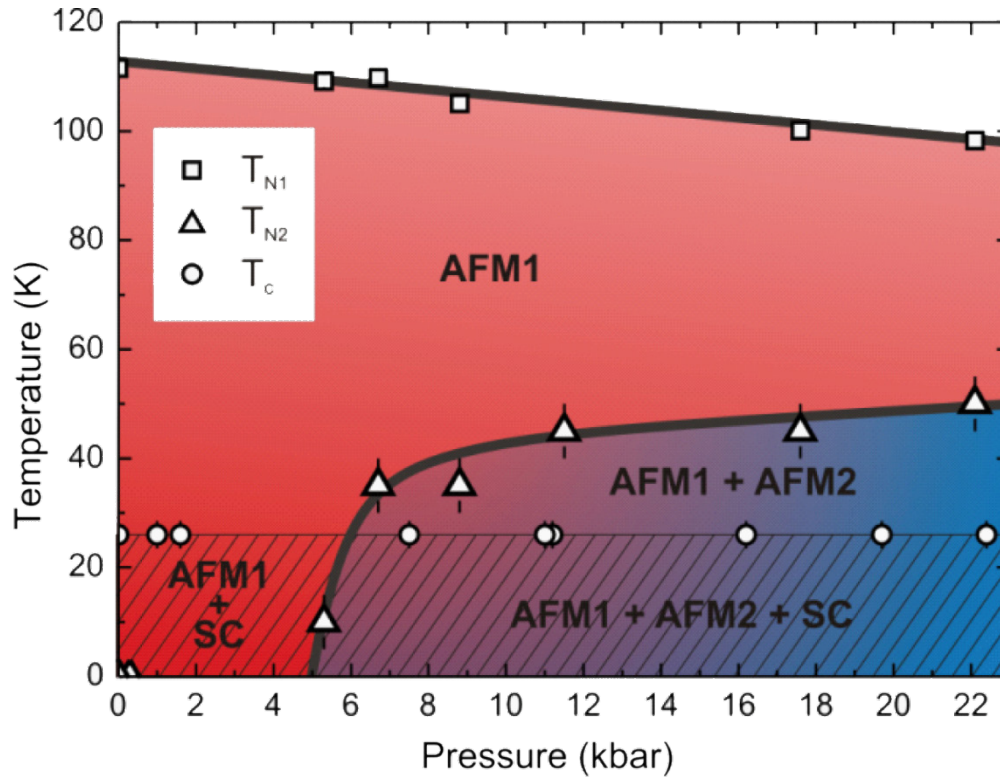


**Figure 5-6:** Magnetic phase diagram of  $\text{Ba}_{0.8}\text{K}_{0.2}\text{Fe}_2\text{As}_2$  from ambient pressure up to 22.1 kbar.

AFM1 diminishes slightly with rising pressure, while the new magnetic phase AFM2 evolves at 5.3 kbar. It grows with increasing pressure and reaches a maximum  $T_N$  of 50 K at 22.1 kbar. The measured  $T_c$  (26 K) stays constant over the whole measured pressure range. Such behavior has been observed before for samples with  $x = 0.3$  [109], but not for  $x = 0.2$ . Additionally, the  $T_c$ s for  $\text{Ba}_{0.8}\text{K}_{0.2}\text{Fe}_2\text{As}_2$  reported in literature vary between 6 and 26 K [42, 44, 109]. Thus, slight composition changes in this area of the phase diagram lead to remarkably different superconducting transition temperatures and a different behavior under pressure. AFM1 and superconductivity coexist on a microscopic scale throughout the whole measured pressure range. The new magnetic phase AMF2 behaves similarly to AFM1 with regards to its interplay with superconductivity. From its evolution at about 5 kbar to the highest obtained pressure of 22.1 kbar it coexists with superconductivity. In contrast to that, due to having their own distinct volume, both magnetic fractions are phase separated.

Comparing these results with higher-doped potassium samples ( $x > 0.2$ ), we see an increase of the  $T_c$  up to 39 K in optimally doped  $\text{Ba}_{0.6}\text{K}_{0.4}\text{Fe}_2\text{As}_2$  and a decrease of

the magnetic volume fraction. According to that, a phase separation of the magnetic and the superconducting phase occurs. The pressure experiments performed here show neither an increase of  $T_c$ , nor a phase separation. This emphasizes that the two doping agents cannot be treated equally, as it was already shown for other co-doped  $\text{BaFe}_2\text{As}_2$  descendants.

## 5.4 Conclusion

In conclusion, the microscopic coexistence of superconductivity and magnetism in  $\text{Ba}_{0.8}\text{K}_{0.2}\text{Fe}_2\text{As}_2$  has been verified at ambient pressure and up to 22.1 kbar. Above a pressure of about 5 kbar a new magnetic phase AFM2 with a maximum  $T_N$  of 50 K at 22.1 kbar was detected. It has the same spin structure as the known antiferromagnetic order AFM1 but exhibits smaller magnetic moments and becomes more and more distinct with rising pressure. Meanwhile, the transition temperature of the known magnetic order AFM1 decreases constantly towards higher pressures, but AFM1 persists over the whole pressure range. When reaching  $T_c$ , which remains unchanged up to 22.1 kbar, this new magnetic order also coexists with superconductivity on a microscopic scale. The coexistence of superconductivity and the two antiferromagnetic orders in  $\text{Ba}_{0.8}\text{K}_{0.2}\text{Fe}_2\text{As}_2$  under pressure and the fact that a new magnetic phase is induced with rising pressure itself shows again that physical pressure and doping are not equal. The combination of both leads to different results than using one modification alone.

## 6 Exploring the potential of $\text{Ba}_{0.6}\text{K}_{0.4}\text{Fe}_2\text{As}_2$ wires and tapes

*Parts of this chapter are accepted as :*

"Role of heat and mechanical treatments in the fabrication of superconducting  $\text{Ba}_{0.6}\text{K}_{0.4}\text{Fe}_2\text{As}_2$  ex-situ Powder-In-Tube tapes"

A. Malagoli, E. Wiesenmayer, S. Marchner, D. Johrendt, A. Genovese, M. Putti, *arXiv: 1507.03781*.

*Accepted in Superconductor Science and Technology. © 2015 IOP Publishing*

### 6.1 Motivation

The development, the production, and application of superconducting wires and tapes is an ongoing process and can help to improve a large variety of aspects in our life from small specific devices, like magnets in NMR spectrometers, to large power grids. The hope is that superconducting wires and tapes could replace conventional wires, at least in some areas, because of their improved efficiency combined with a simultaneous size reduction. For example a study of the *US Department of Energy* states that 7-10 % of electric power in the USA is lost in the copper-wire based power grid<sup>[110]</sup>. This corresponds to almost 180 million tons of  $\text{CO}_2$  from fossil power plants. Nevertheless, there is still a lot to be done until these new materials can find their way into daily life, and exceed the test phase, as wires in the power grid<sup>[111]</sup>, motors<sup>[111]</sup>, or generators<sup>[4]</sup>. Problems like low carrier densities, a short coherence length, the high anisotropy, thermal fluctuations, or current blocking grain boundaries in high-temperature superconductors need to be overcome in order to raise the critical current density and lower the costs. Up to now, a lot of effort was already made<sup>[112-115]</sup> for compounds like  $\text{MgB}_2$ <sup>[116-117]</sup>, diverse cuprates like  $\text{Bi-2212}$ <sup>[118]</sup>,  $\text{Bi-2223}$ <sup>[119-120]</sup> or  $\text{YBCO}$ <sup>[121-123]</sup>, and also iron-based superconductors like different  $1111$ <sup>[65, 124]</sup> compounds or  $\text{FeSe}$ <sup>[125-126]</sup>. In this chapter, the focus lies on a sufficiently large amount of high-quality  $\text{Ba}_{0.6}\text{K}_{0.4}\text{Fe}_2\text{As}_2$  for the production of wires and tapes in

order to explore how far the critical current density can be improved.  $\text{Ba}_{0.6}\text{K}_{0.4}\text{Fe}_2\text{As}_2$  displays certain advantages compared to the aforementioned superconductors. It shows a higher  $T_c$  than FeSe, is less anisotropic than the 1111 compounds, can operate at higher magnetic fields<sup>[127]</sup> than  $\text{MgB}_2$ , is robust to impurity doping<sup>[128]</sup>, and the misalignment of the grains can be higher than in cuprates.

## 6.2 Powder synthesis and characterization

To investigate the potential of  $J_c$  in  $\text{Ba}_{0.6}\text{K}_{0.4}\text{Fe}_2\text{As}_2$  materials, sufficient high-quality material has to be produced. Due to the limited size of the alumina crucibles used for the synthesis (reasons for their usage are explained in chapter 7.2) and to guarantee an equal quality of the samples,  $\text{Ba}_{0.6}\text{K}_{0.4}\text{Fe}_2\text{As}_2$  was synthesized in multiple portions of 1 g by heating stoichiometric mixtures of the elements (purities > 99.9 %) (see chapter 7.3). In only a few of the samples, small fractions of the impurity phase FeAs (< 3.5 %) were detected due to potassium evaporation. The lattice parameters, the Ba/K-ratio, and the purity were obtained by X-ray powder diffraction (Cu- $K_{\alpha 1}$ -radiation) and Rietveld refinements using the TOPAS package<sup>[51-52]</sup>. After careful analysis, the portions were united and used for the wire/tape production.

A powder diffraction pattern and the Rietveld fit of one sample free from impurity phases is depicted in Figure 6-1, while the X-ray powder diffraction patterns of a complete batch, containing seven portions, are shown in Figure 6-2.

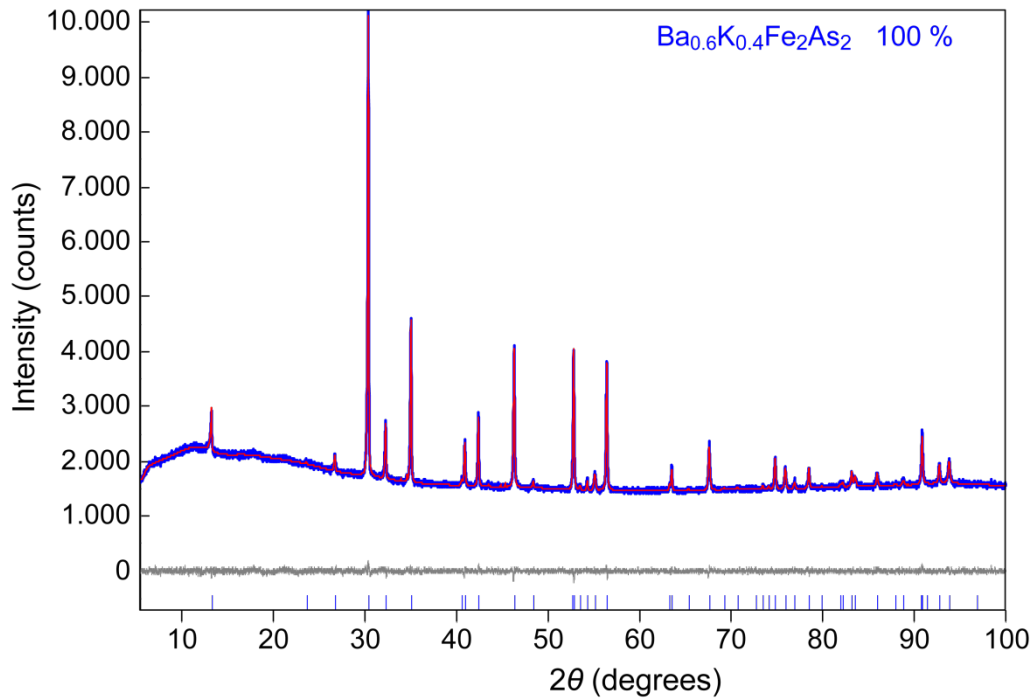


Figure 6-1: X-ray powder pattern (blue) and Rietveld fit (red) of one of the  $\text{Ba}_{0.6}\text{K}_{0.4}\text{Fe}_2\text{As}_2$  portions used in the wire/tape fabrication.

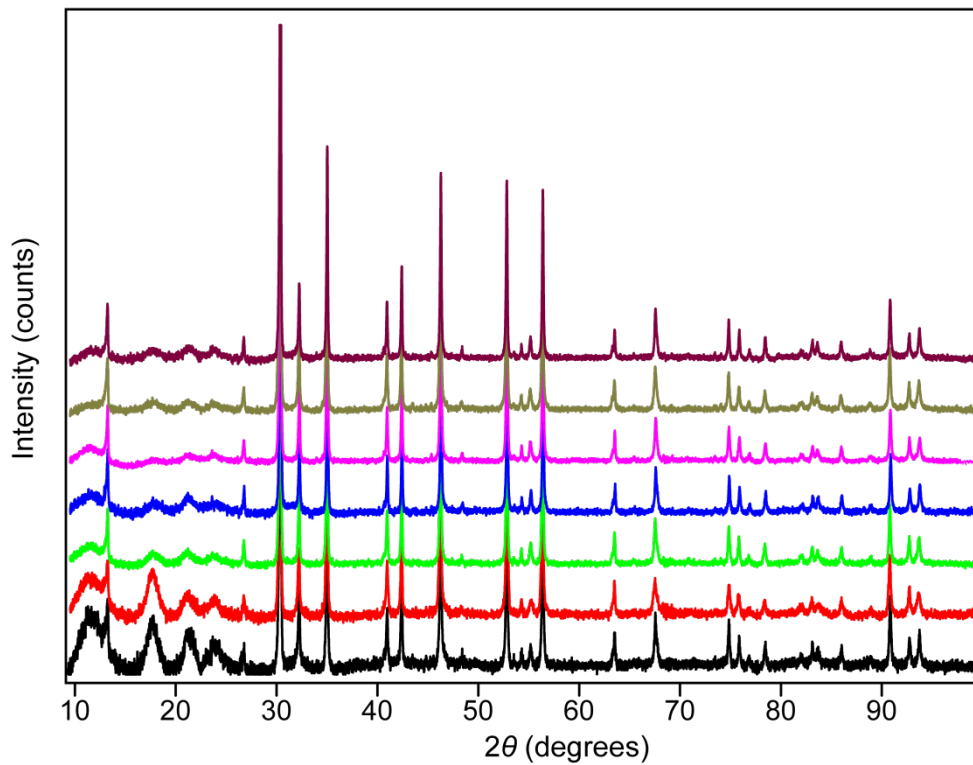
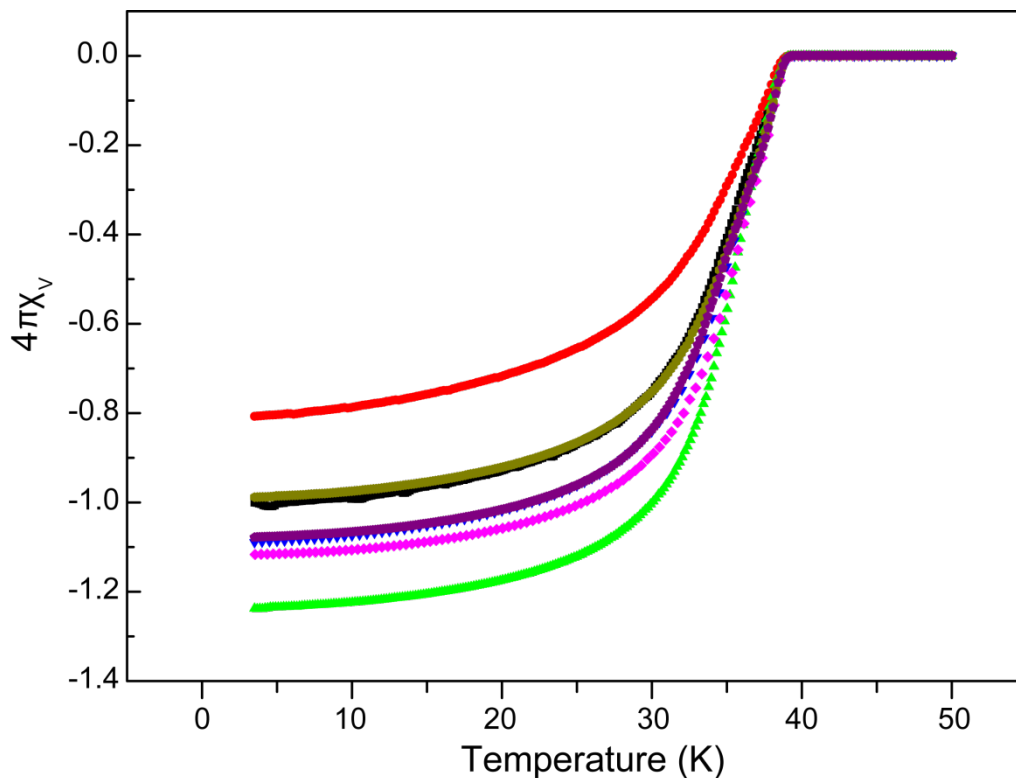


Figure 6-2: X-ray powder patterns of one complete batch (containing seven different samples) used in the production of one wire.

The four broad reflections between  $10$  and  $26^\circ 2\theta$ , especially pronounced in the red and the black powder pattern, are measurement artifacts. In order to obtain high-quality material with a homogeneous potassium distribution, the samples have to be homogenized accurately after each step. Otherwise, the XRD pattern reflections as well as the superconducting transition will be broadened.

The susceptibility measurements of the portions are shown in Figure 6-3.



**Figure 6-3:** Susceptibility measurement of the seven portions of  $\text{Ba}_{0.6}\text{K}_{0.4}\text{Fe}_2\text{As}_2$  that were used for the fabrication of one wire.

The superconducting volume fraction of all samples is above 80 % and proves bulk superconductivity. Furthermore, we see that as a result of the careful homogenization the whole batch has a narrow superconducting drop and almost the same superconducting transition temperature of 38.5 K.

## 6.3 $\text{Ba}_{0.6}\text{K}_{0.4}\text{Fe}_2\text{As}_2$ wires and tapes

### 6.3.1 The powder in tube method

The powder in tube method (P.I.T.) is a popular way to produce wires and tapes<sup>[129-131]</sup>. The interest in producing  $\text{Ba}_{0.6}\text{K}_{0.4}\text{Fe}_2\text{As}_2$  filaments is based on the properties described in chapter 6.1. The wires and tapes investigated in the following were produced by *Dr. Andrea Malagoli* (CNR-SPIN in Genoa, Italy). A schematic illustration of the method is shown in Figure 6-4.

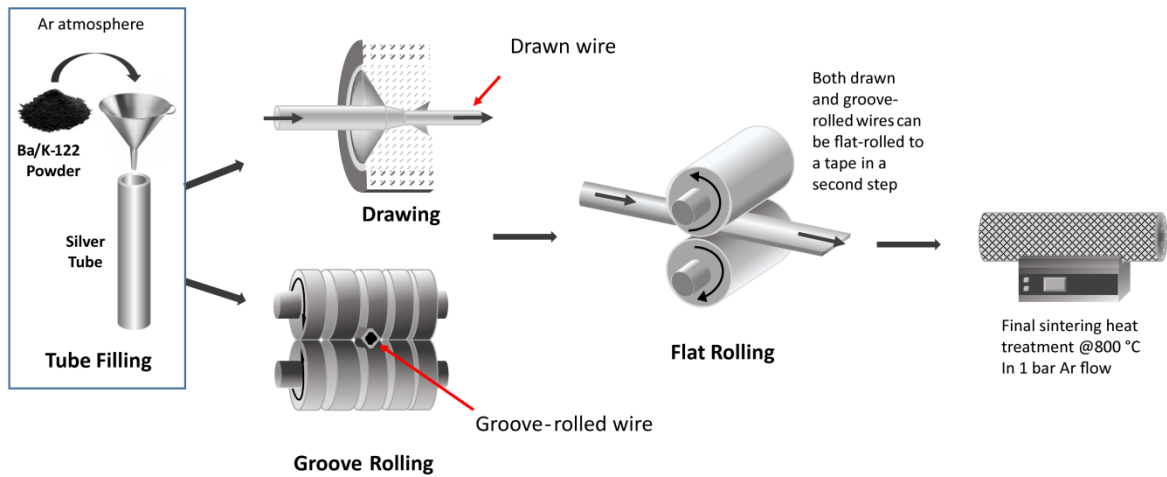


**Figure 6-4:** Fabrication process of wires and tapes in a silver tube. Starting from the tube filling (on the left) to drawing/groove rolling into wires and flat rolling of the wires to tapes and the final heat treatment<sup>[69]</sup>.

Thus, several wires and tapes were prepared from about 20 g of  $\text{Ba}_{0.6}\text{K}_{0.4}\text{Fe}_2\text{As}_2$  filled in various silver tubes with an outer diameter of 8 mm and an inner diameter of 5 mm. The silver tube was chosen among other materials like Nb, Ta, or Fe/Ti<sup>[132]</sup> because of its processability and reduced tendency to react with As at higher temperatures. This composite tube was cold worked through drawing, flat rolling, and groove rolling to obtain wires or tapes with different thicknesses and different levels of powder compaction. In order to further enhance the strength of the deformation, in one of the samples a double metallic sheath composed by an external nickel and an

internal silver tube was used. The specifications of the samples are collected in Table 6-1.

**Table 6-1: List of the samples with specification on the pursued preparation route and final size.**

Sample (sheath)	Process	Size
A (Ni/Ag)	groove-rolled wire	1 x 1 mm <sup>2</sup>
B (Ag)	drawn wire	Ø 0.9 mm
C (Ag)	drawn + flat-rolled tape	0.5 mm thick
D (Ag)	drawn + flat-rolled tape	0.4 mm thick
E (Ag)	groove-rolled wire	0.9 x 0.9 mm <sup>2</sup>
F (Ag)	drawn + groove-rolled wire	0.9 x 0.9 mm <sup>2</sup>
G (Ag)	groove-rolled + flat-rolled tape	0.4 mm thick

A selection of the wire/tape cross sections resulting from the deformation process is shown in Figure 6-5.

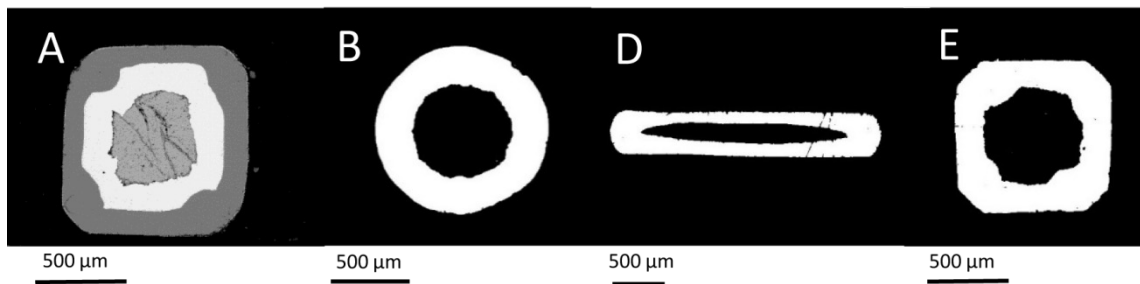


**Figure 6-5: Cross sections of selected samples.**

After the fabrication the wires/tapes were cut into 1 cm long pieces and underwent a sintering heat treatment in a three-zone tubular furnace with a homogeneity zone ( $\pm 0.5$  K) of 16 cm at different annealing temperatures between 973 – 1123 K. During the heat treatment a constant Ar flow with a pressure of 1 bar was applied. It is performed to enhance the intergrain connectivity and recover cracks produced in the wire and tape drawing/rolling. Before the heat treatment, the ends of all samples

were sealed by dipping them into molten silver to prevent the evaporation of potassium.

### 6.3.2 Properties of the wires and tapes

In order to optimize the sintering temperature, 1 cm pieces of sample D have been heat-treated for half an hour at different temperatures (973 K, 1073 K, and 1123 K, respectively). Figure 6-6 shows the resistance measurements of these samples.

A drop to zero resistivity at 36.8 K was measured for the tapes annealed at 1073 K and 1123 K, while for the sample heat-treated at 973 K the drop is at 33.2 K. Concerning the shape of the transitions, we observe that the steepest one is measured for the 1073 K sample denoting a better homogeneity of the superconducting core.

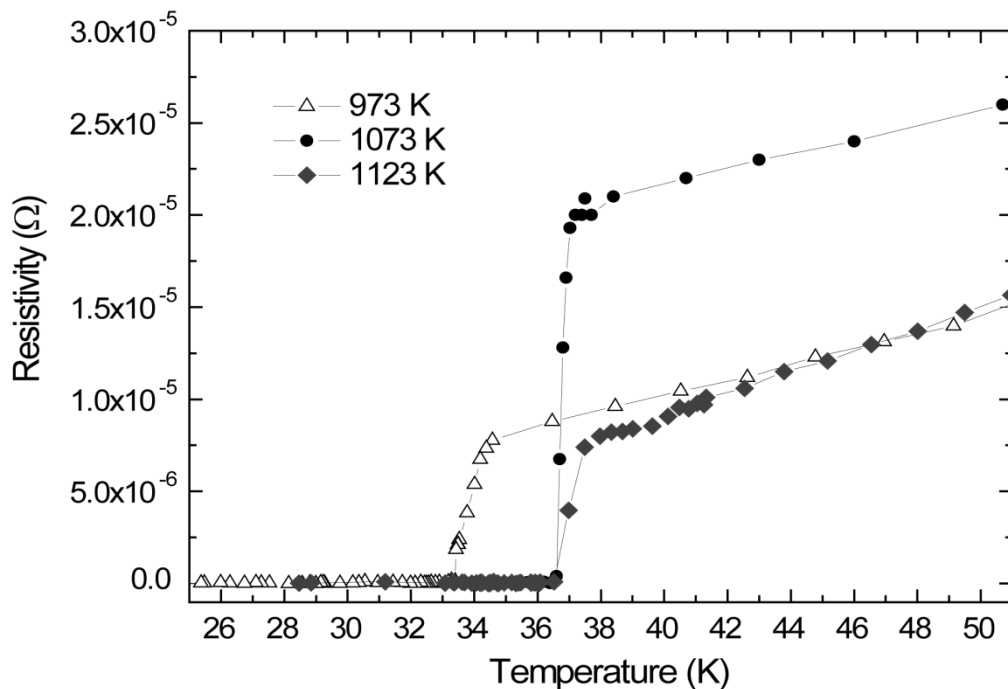
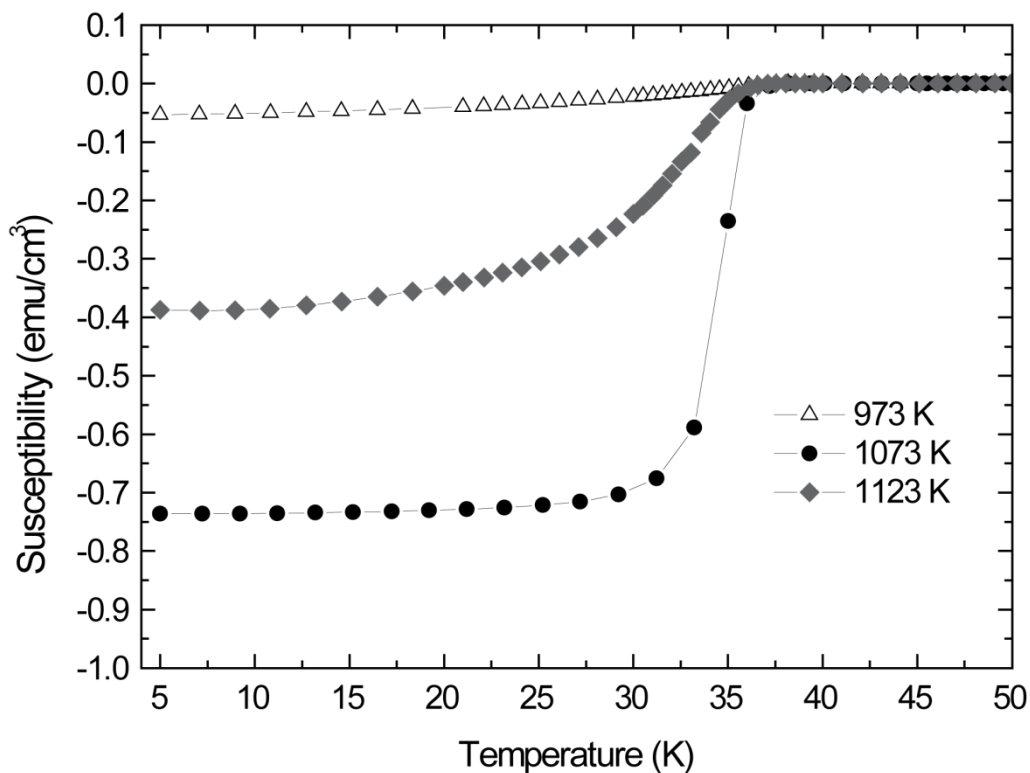


Figure 6-6: Resistivity measurements of different pieces of sample D annealed at 973 K, 1073 K, and 1123 K.

Short sample pieces of about 6 mm in length were employed for the magnetization measurements vs. temperature, performed with a commercial 5.5 T MPMS *Quantum Design* Squid magnetometer using a background field of 10 Oe.

The measurements, shown in Figure 6-7, exhibit similar  $T_c$  values for tapes annealed at 1073 K ( $T_c = 37.7$  K) and 1123 K ( $T_c = 37.0$  K). These are the highest measured critical temperatures in tapes and wires so far. However, the behavior of the susceptibilities is quite different. While for the sample treated at 1073 K an almost complete shielding and a narrow superconducting transition are observed, the sample annealed at 1123 K only exhibits partial shielding and the one annealed at 973 K almost no shielding.



**Figure 6-7:** Susceptibility measurement of different pieces of sample D annealed at 973 K, 1073 K, and 1123 K.

As a result of the resistivity and susceptibility measurements only the samples annealed at 1073 K and 1123 K were further investigated. High resolution SEM images of the tape cores annealed at 1073 K (pictures on the left) and 1123 K

(pictures on the right) are depicted in Figure 6-8. The gray scale is a measure for the electron contrast. Black areas are cavities. Light gray areas represent  $\text{Ba}_{0.6}\text{K}_{0.4}\text{Fe}_2\text{As}_2$  and the dark gray areas, emphasized with red circles, are the impurity phases  $\text{Fe}_2\text{As}$  and  $\text{FeAs}$ . After the heat treatment at 1073 K only small isolated grains of impurity phase were detected. In contrast to that, the tape annealed at 1123 K exhibits large impurity domains between the superconducting grains. By a variation of 50 K the nucleation and growth of the impurity phases is essentially increased.

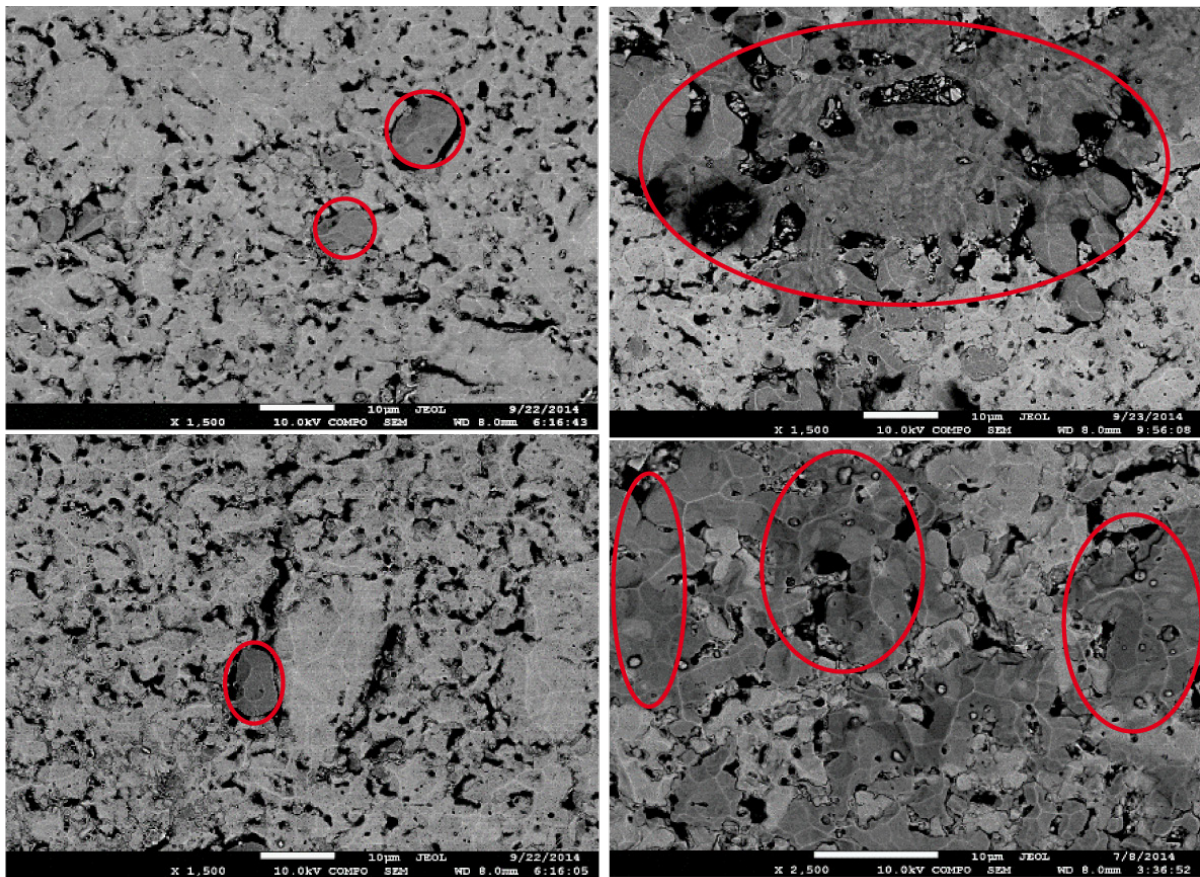


**Figure 6-8:** High resolution SEM images of 0.4 mm tapes annealed at 1073 K (left) and 1123 K (right). The red ellipses emphasize the impurity grains.

Figure 6-9 shows a TEM analysis of the tape heat-treated at 1073 K. In Figure 6-9a three different crystal grains with almost parallel interfaces are pictured. The EDX analysis shows a homogeneous distribution of all four elements over all three grains

in linear and areal mapping (Figure 6-9b and c). The increase of the concentrations in the linear mapping is a result of a slight increase of the particle thickness from left to right. High resolution TEM also shows only semicoherent and incoherent grain boundaries as a result of a slight misalignment of the grains (Figure 6-9d and e). Still, the grains tend to adopt a similar orientation with the *c*-axis along the direction of the tape elongation.

The sample annealed at 1123 K displays different properties (Figure 6-10). The EDX mapping of the two grains clearly shows two different phases in grain A and B (Figure 6-10a). Grain A is divided into two phases. The upper part exhibits a homogeneous distribution of barium, potassium, iron, and arsenic representing  $\text{Ba}_{0.6}\text{K}_{0.4}\text{Fe}_2\text{As}_2$ . The lower part of grain A is different. Two dark spots for barium and potassium appear, while the iron spot remains bright. However, the distribution of the arsenic is homogeneous. This is a clear evidence for an iron-arsenide impurity phase in grain A. In grain B the situation is similar to the one in the lower part of grain A. Although barium and potassium are still detectable, iron and arsenic dominate the EDX mapping. This can also be visualized in Figure 6-10b. High resolution TEM images of both grains and their grain boundary show not only a semicoherent interface but also different compositions for grain A and B displayed by diverging lattice periodicities.

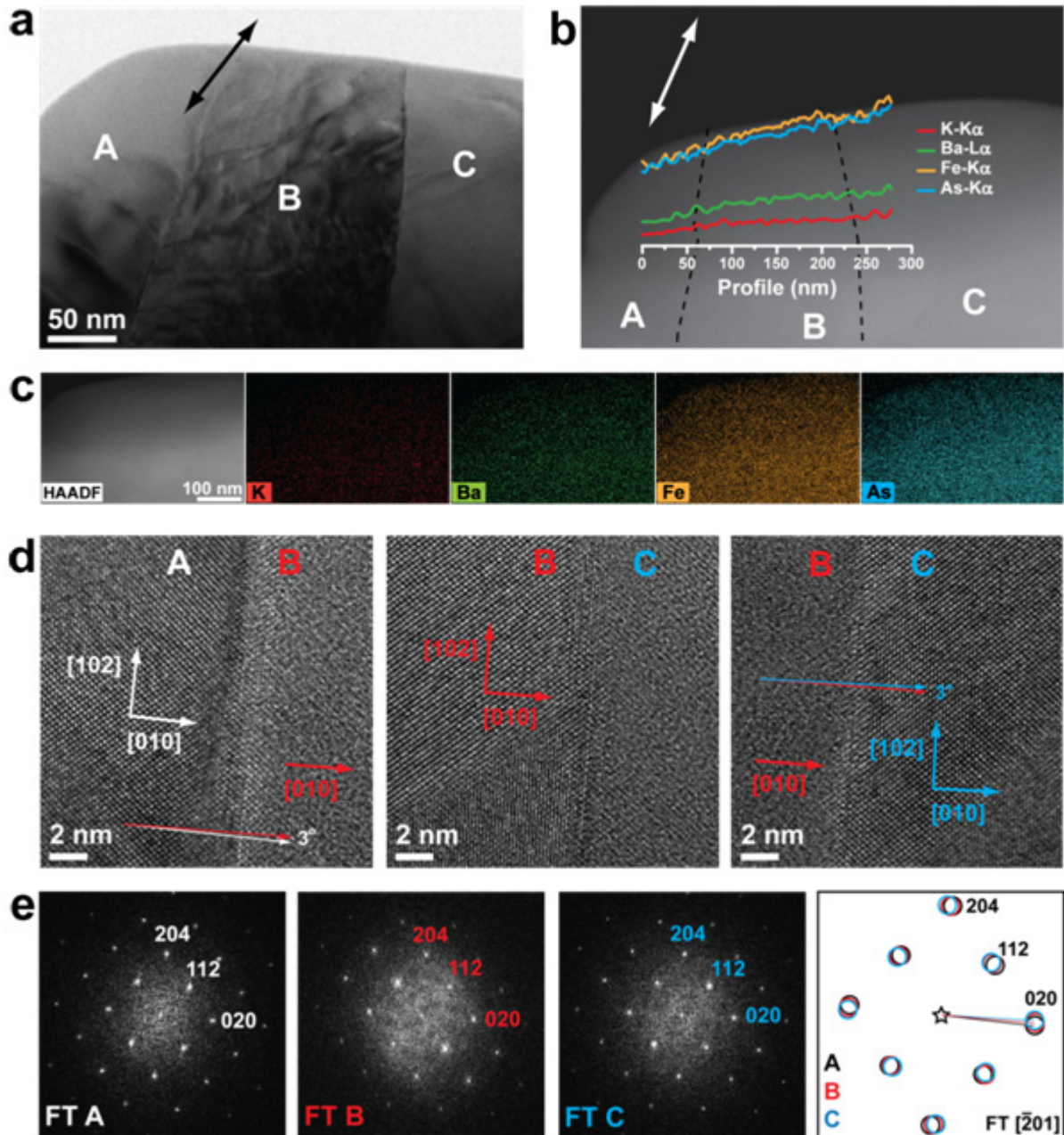
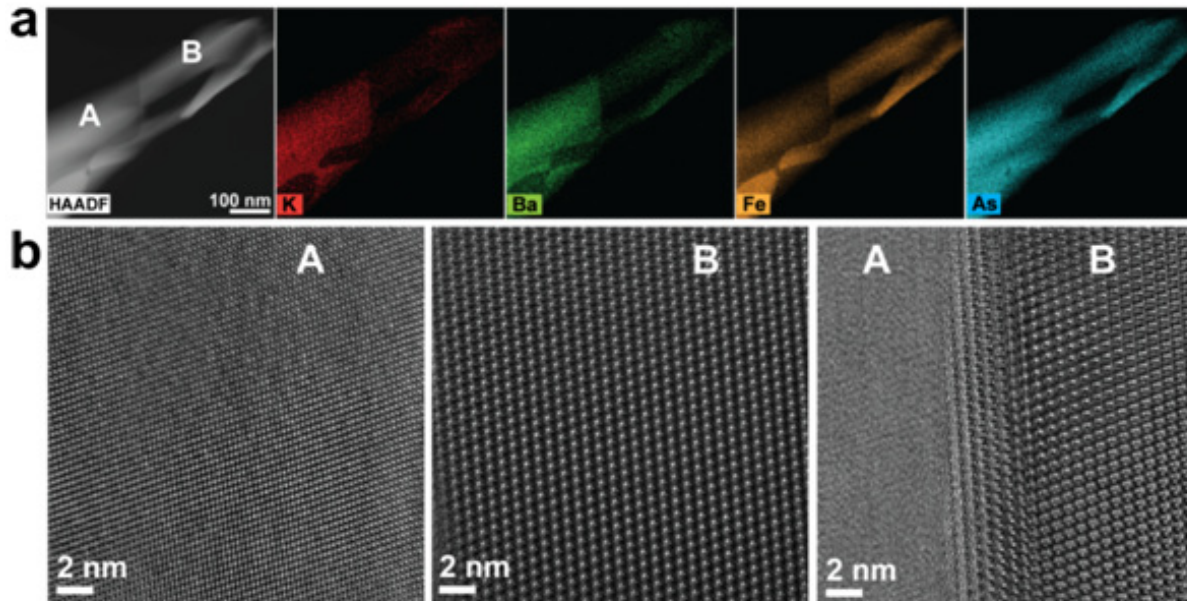


Figure 6-9: TEM analysis of the sample annealed at 1073 K. a) Three connected grains A, B, and C of  $\text{Ba}_{0.6}\text{K}_{0.4}\text{Fe}_2\text{As}_2$  with almost parallel interfaces recorded by EFTEM (the black arrow displays the direction of the elongation). b) HAADF image with EDX analysis of A, B, and C. The grain boundaries are marked by black dotted lines and the white arrow displays the direction of the elongation. c) Areal EDX mapping of the HAADF image. d) High resolution TEM of the grain boundaries observed along the  $[-201]$  zone axis. e) Fourier transform (FT) of the three grains showing the 204, 112, and the 020 spots of  $\text{Ba}_{0.6}\text{K}_{0.4}\text{Fe}_2\text{As}_2$ .



**Figure 6-10:** TEM analysis of the sample annealed at 1123 K. a) HAADF image and areal EDX mapping of two grains A and B. d) High resolution TEM of the grains and their boundary.

Another key aspect to improve the grain connectivity and by that the performance of the wires and tapes is the deformation process. To investigate the effect of deformation, a closer look is taken at the samples A and B. Sample A has a double metallic sheath, composed by silver for the inner sheath and nickel for the outer sheath. It underwent the strongest deformation due to the groove rolling. In contrast to that sample B, having only one silver sheath, was deformed only by drawing, probably the softest deformation applied on all samples.

To see the effects of the deformation on the superconducting core, the sheath in both samples had to be removed. Artificial damage through polishing was avoided by carefully etching the sheaths in a solution of  $\text{H}_2\text{O}_2$  (30 %) and  $\text{NH}_3$  (30 %). In Figure 6-11 several representative millimeters of two wires are depicted after deformation, but before the annealing. Wire A exhibits a dense core structure on one side, but also numerous transversal cracks that probably aggravate the current flow through the core. In sample B the core density is less distinct. Cracks are also visible but they align along the longitudinal axis of the wire, typical for cold working like drawing, and thus shouldn't hinder the current flow.

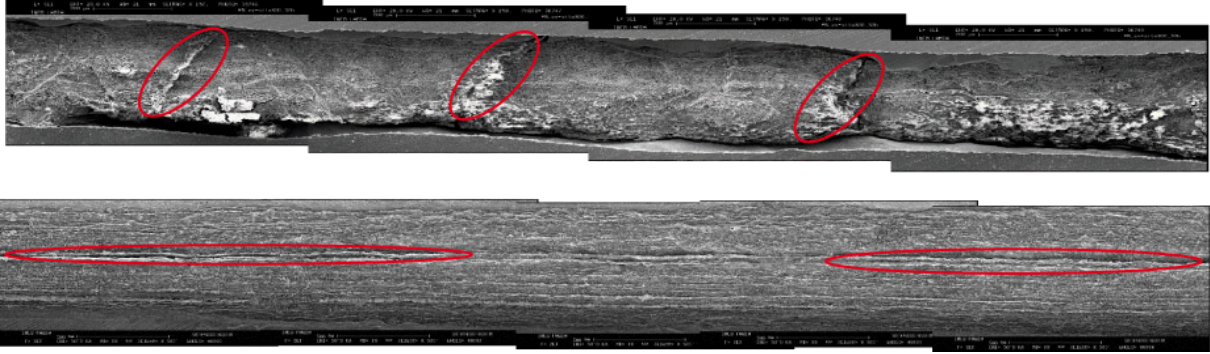


**Figure 6-11: SEM images of longitudinal cross sections of sample A (top) and sample B (bottom). The red ellipses emphasize the cracks.**

Based on this insight, the samples E and G were produced and the effect of the deformation on these samples was investigated. Wire E has a soft silver sheath and was groove rolled. The tape G has the same coating and was groove rolled but was additionally flat rolled into a 0.4 mm thick tape. To see the effect on the core, the sheath was partially removed again by chemical etching with  $\text{H}_2\text{O}_2$  and  $\text{NH}_3$ .

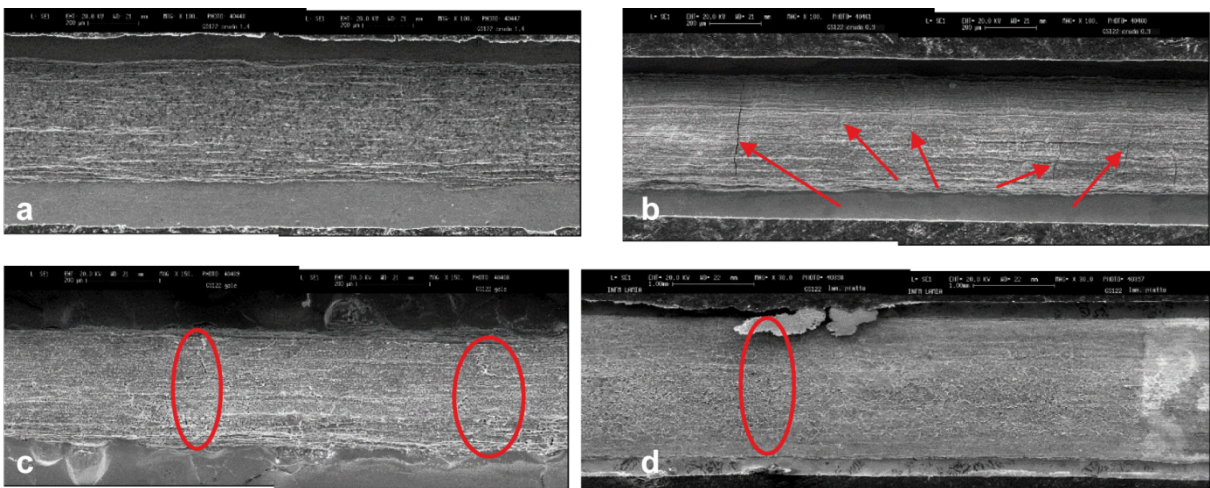


**Figure 6-12: SEM images of longitudinal cross sections at an intermediate stage (a), after the groove rolling (b) and after the heat treatment (c) for sample E. SEM image at the final stage after the heat treatment for sample G (d). The red arrows and ellipses emphasize the cracks.**

In Figure 6-12a to c SEM images of wire E are shown. At an intermediate stage of the groove rolling the  $\text{Ba}_{0.6}\text{K}_{0.4}\text{Fe}_2\text{As}_2$  core displays a certain porosity, but still looks very uniform. After the complete deformation the filament density is further enhanced, but numerous transversal cracks have evolved (red arrows, Figure 6-12b). The majority of them can be undone by the heat treatment at 1073 K as shown in Figure 6-12c (red ellipses mark the remaining cracks). Looking at the SEM image of Figure 6-12c it can be further stated that the annealing also enhances the grain size and the intergrain connectivity. Comparing wire E to tape G (Figure 6-12d) similar results including the residual cracks, but with higher core density are obtained after the heat treatment.

The critical current densities  $J_c$  were measured after annealing at 1073 K and 1123 K. In the samples A, E, and G no critical current density was measured, although they displayed a high core density. This is probably a consequence of the transversal cracks, resulting from the deformation process. In the other wires and tapes B, C, D, and F no critical current density was quantified after the heat treatment at 1123 K, most likely because of the amount of impurity phase. But B, C, D, and F samples at 1073 K all displayed detectable  $J_c$ s after the annealing (Figure 6-13).

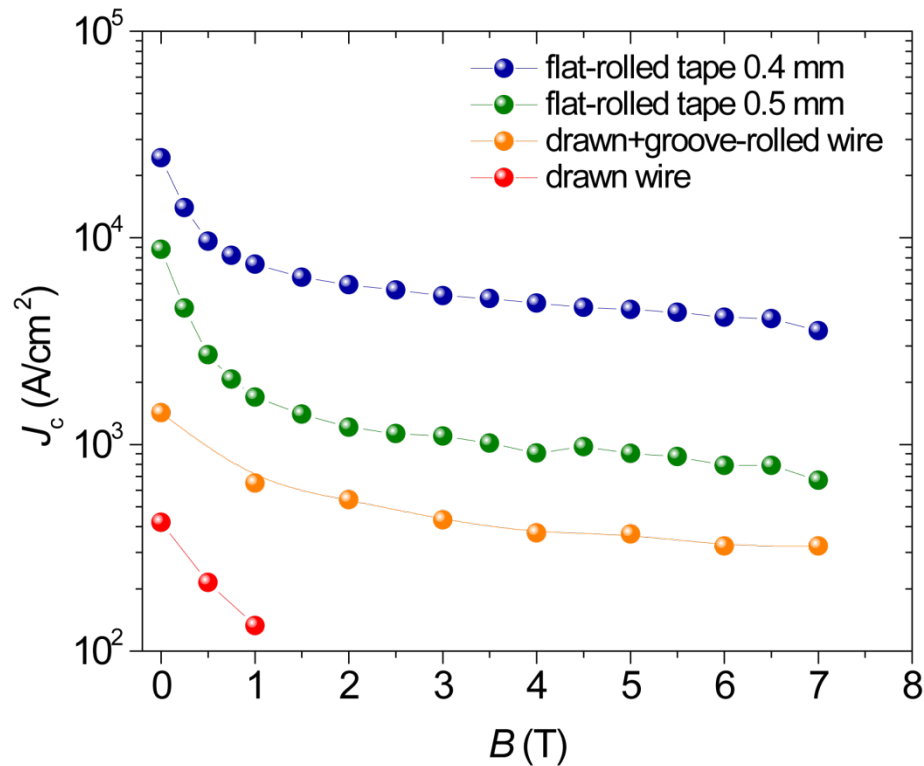


**Figure 6-13:** Critical current density as a function of the applied field for wires B (red) and F (yellow) and for the tapes C (green) and D (blue).

The differences between the samples exhibiting a current density and the ones which do not are the temperature of the heat treatment and the deformation process. Temperatures above 1073 K lead to formation of high amounts of impurity phase. These non-superconducting impurity phases block the current flow. As for the deformation, the samples B, C, D, and F were first processed by drawing instead of groove rolling and afterwards either groove rolled (wire F), flat rolled (tapes C and D), or not further deformed (wire B). This shows that a steady increase of the cold-working strength by drawing is better than an instant high cold-working strength through groove rolling. The measured  $J_c$  curves drop steeply within 1 T (Figure 6-13), but then slowly decrease for higher fields, almost displaying field independence, making  $\text{Ba}_{0.6}\text{K}_{0.4}\text{Fe}_2\text{As}_2$  a candidate for a possible high field application.

Another aspect important for a possible application is the  $n$ -factor. The current density is related to the sample size  $a$  by the power law  $J \propto a^{1/n}$ .  $n$  represents the  $n$ -factor and is a geometrical quantity that tells us if a superconductor is capable of

being used in the persistent mode<sup>[133]</sup>. This allows the advantages of a compact superconducting magnet with high field stability<sup>[134]</sup>. If the  $n$ -factor becomes large, the sample size dependence vanishes because  $a^{1/n} \rightarrow 1$ . In low-temperature superconductors values between 10 and 100 are typical. For a constant use of a superconducting magnet  $n$ -values of 30 and higher at the highest field are required. For sample D it was derived from the  $V$ - $I$  curve as seen in Figure 6-14.

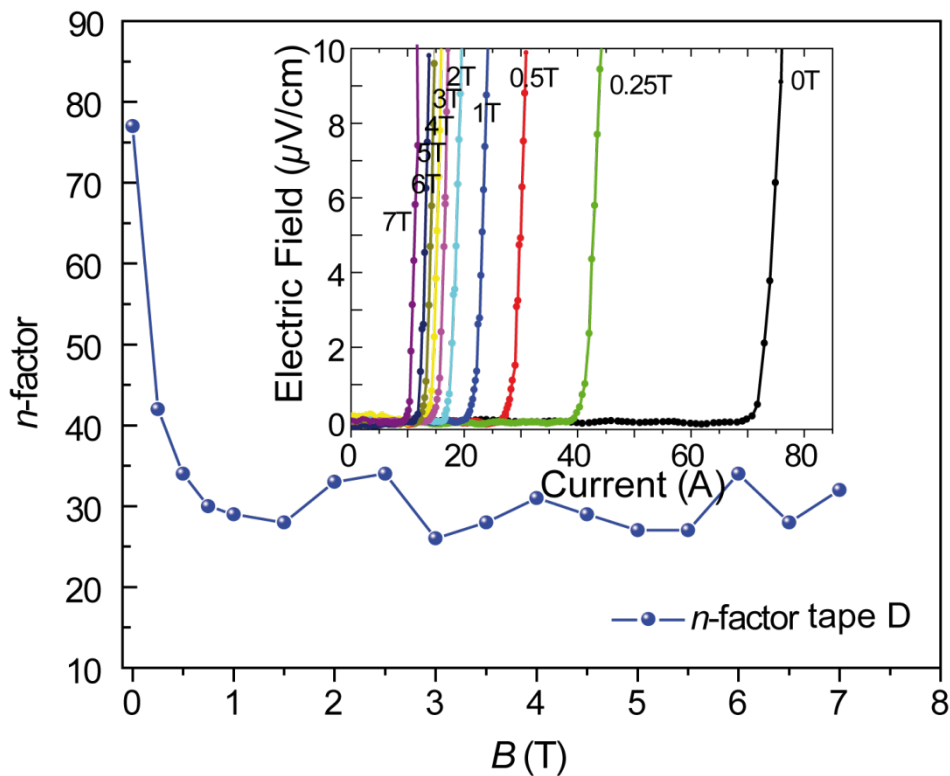


**Figure 6-14:**  $n$ -factor as a function of the applied field for the tape D derived from  $V$ - $I$  curves (inset).

Leaving the high values for fields below 1 T out, an average value of 30 is received, indicating a high homogeneity and uniformity in this tape, qualifying it for a constant use.

## 6.4 Discussion

In this chapter the production process and its impact on the physical properties of  $\text{Ba}_{0.6}\text{K}_{0.4}\text{Fe}_2\text{As}_2$  wires was investigated. Regarding the heat treatment, the path without additional pressure was chosen that can be applied in up-scaled processes for industrial use. Additional pressure during the synthetic process as performed in [135-136] results in a possible enhancement of the core density, thus in a better grain connectivity, and prevents element losses, leading to improved superconducting properties, but it is clear that this would complicate and raise the price for long wires. Element loss in the case of the before-investigated samples was averted by sealing the ends with molten silver. Here, three different temperature programs at 973 K, 1073 K, and 1123 K were tested. The best results obtained here were those heat-treated at 1073 K, showing values for  $J_c$  comparable with those reported for similar cold-rolled tapes<sup>[137]</sup>. At 1123 K the formation of large amounts of the impurity phases FeAs and  $\text{Fe}_2\text{As}$  (Figure 6-8) was observed. The increased nucleation of impurity phases achieved by applying temperatures higher than 1073 K is in agreement with results known from literature described and discussed previously on FeAs-based superconductors<sup>[124, 135]</sup>. On the other hand, at 973 K the temperature was not high enough to obtain a proper sintering, improve the grain connectivity, and the  $T_c$  of only 33 K was measured with almost no shielding (Figure 6-7). Before using the powder for the wire production, it displayed almost optimal  $T_c$  (38.5 K). Possibly an oxygen-contaminated Ar flow during the heat treatment led to the reduced superconducting properties.

Looking at the effect of the cold deformation on the microstructure, significant points for the manufacturing were revealed and confirmed. As seen before<sup>[118]</sup>, a desirable high density of the superconducting core can be achieved by strong deformation of the tube in the PIT processes. The downside is that the strong forces on the tube cause transversal cracks, limiting the current flow in the superconductor. A softer drawing instead of groove rolling avoids the evolution of cracks (Figure 6-11), but causes a higher porosity of the core. Constant flat rolling of the drawn wire (Figure 6-9) increases the core density and enhances the superconducting performance, but also provokes cracks, even though less than in groove-rolled samples. However, through annealing of the cold-worked wires and tapes, the cracks can be undone

(Figure 6-12) and critical current densities were obtained (Figure 6-13). The received critical current densities display a weak field dependence and values up to  $2 \times 10^4 \text{ A/cm}^2$  at low magnetic fields and critical temperatures up to 37.7 K.  $J_c$  values considerably higher than these have already been reported:  $J_{cs} > 1 \times 10^5 \text{ A/cm}^2$  at low fields and  $7.7 \times 10^4 \text{ A/cm}^2$  at 10 T in double-sheathed  $\text{Ba}_{0.6}\text{K}_{0.4}\text{Fe}_2\text{As}_2$  tapes<sup>[68]</sup>. Still, the  $T_c$  reported there (37.2 K) is lower, indicating either a worse potassium distribution or a slight deviation from the  $\text{Ba}_{0.6}\text{K}_{0.4}\text{Fe}_2\text{As}_2$  stoichiometry, because of the usage of up to 20 % excess potassium. In contrast to that, the samples presented here were synthesized using stoichiometric mixtures, maintaining the control of the final product's stoichiometry. A homogeneous distribution of the potassium in our tapes was also verified by the  $n$ -factor with an average value above 30 on a cm scale. This confirms the potential of these tapes for real application. Nevertheless, looking at the values of  $J_c$  there still is room for further improvement. To avoid a worsening of the superconducting properties, the heat treatment should be executed in a strictly water- and oxygen-free environment. Moreover, using a third sheath and flat rolling the tape to even smaller thicknesses could perhaps further improve the critical current density above  $10^5 \text{ A/cm}^2$  at high magnetic fields.

## 7 Optimizing the synthesis process of $Ba_{1-x}K_xFe_2As_2$

### 7.1 Motivation

Upscaling of the  $Ba_{1-x}K_xFe_2As_2$  synthesis is an important issue for further investigations concerning a possible application. This is especially interesting for  $Ba_{0.6}K_{0.4}Fe_2As_2$  because of its  $T_c = 39$  K and its high upper critical field  $H_{c2}$ <sup>[123]</sup>. The known processes for powder samples base on the reaction of the elements<sup>[17, 89, 138]</sup> or use binary precursors<sup>[101, 109]</sup>. The reaction temperatures lie between 873 K and 1373 K. These paths mostly either use excess potassium (explained in chapter 7.2), losing the control of the developing final product, or display considerable amounts of impurity phases. In this thesis two strategies of synthesizing  $Ba_{1-x}K_xFe_2As_2$  and especially  $Ba_{0.6}K_{0.4}Fe_2As_2$  are presented, using either the elements or ternary precursors  $BaFe_2As_2$  and  $KFe_2As_2$  as starting materials.

### 7.2 Synthetic difficulties

A reaction of the starting materials with the container is one of the major issues. Potassium metal is a strong reducing agent with a high vapor pressure (boiling point: 1027 K). Thus, reactions in oxide vessels like silica ampoules lead to a reaction of the evaporated potassium with the ampoule. As a result, FeAs emerges as impurity phase emerges (Figure 7-1). Therefore, using other metals like niobium as a container material would make sense. But because of the high reaction temperatures another problem occurs. At high temperatures the arsenic oxidizes the niobium, resulting in impurity phases like  $Fe_2As$  or various niobium arsenides. Hence a compromise has been found using open alumina crucibles, chosen because of their inert behavior and thermal stability. When adjusting the annealing temperature properly and using alumina inlays (Figure 7-2) to reduce the free space in the ampoule, the desired compound can be obtained without any element loss. This can serve as a model for upscaling the synthetic process.

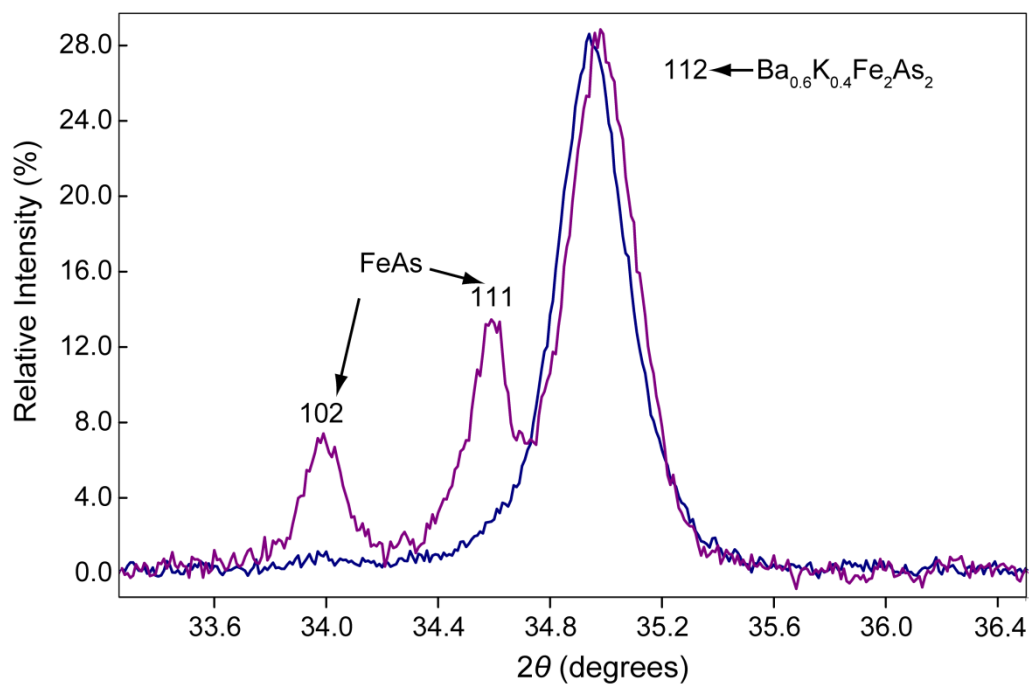


**Figure 7-1:** Section of the X-ray powder diffraction pattern of  $Ba_{0.6}K_{0.4}Fe_2As_2$  free from FeAs (blue) and with FeAs (purple).



**Figure 7-2:** Picture of a stoichiometric mixture of barium, potassium, iron, and arsenic in an alumina crucible with an alumina inlay, sealed in a silica ampoule under purified argon.

The potassium distribution in  $Ba_{1-x}K_xFe_2As_2$  is another key aspect in the synthesis process. It can be estimated by looking at the half-width of the reflections. A smaller

half-width indicates a more homogeneous potassium distribution (Figure 7-3) and thus a sharper superconducting transition is expected (Figure 7-4).

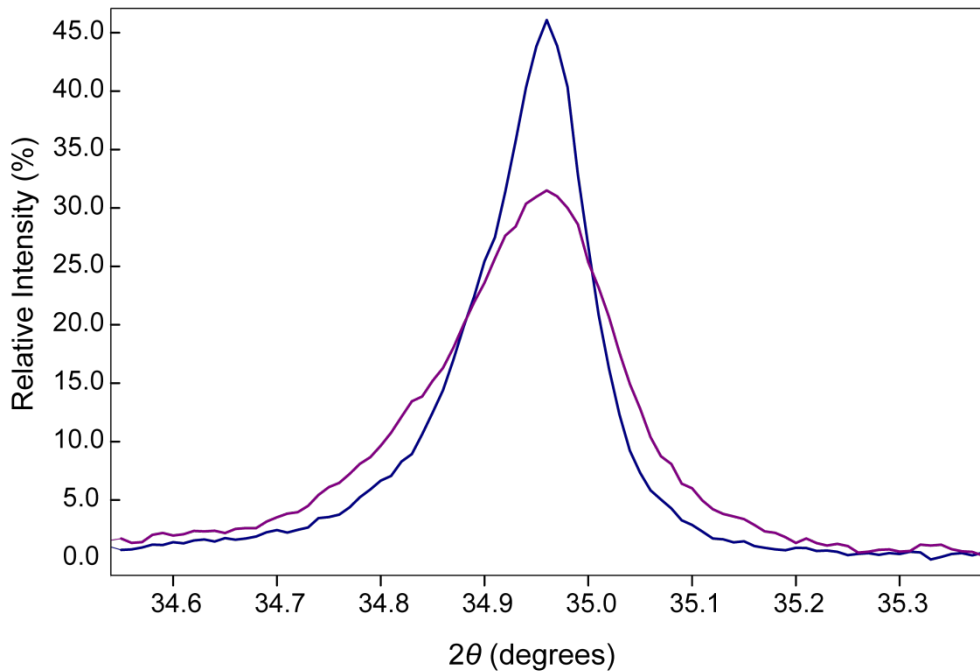


**Figure 7-3:** Section of the X-ray powder diffraction pattern of  $\text{Ba}_{0.6}\text{K}_{0.4}\text{Fe}_2\text{As}_2$  displaying the 112 reflection with a homogeneous potassium distribution (blue) and with a less homogeneous potassium distribution (purple).

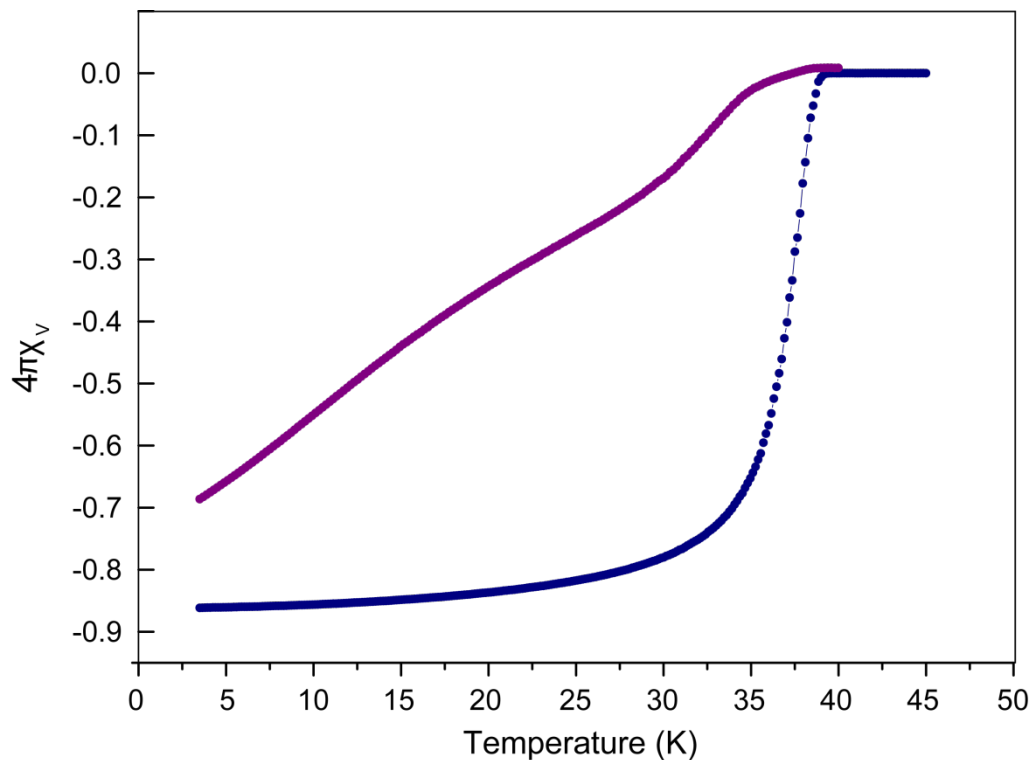


**Figure 7-4:** Susceptibility measurements of  $\text{Ba}_{0.6}\text{K}_{0.4}\text{Fe}_2\text{As}_2$  with a homogeneous potassium distribution (blue) and a less homogeneous potassium distribution (purple).

### 7.3 Element-based synthesis

The synthesis presented here was used to produce all samples investigated in chapters 3 - 6. High-quality powders of  $\text{Ba}_{1-x}\text{K}_x\text{Fe}_2\text{As}_2$  with quantities up to 1.5 g (limited by the size of the container) and small or absent impurity phase fraction can be obtained by an element-based synthesis. The synthesis can also be adapted to other agents like sodium or cobalt. It is a modification of the synthesis published by *Rotter et al.*<sup>[17]</sup>. Depending on the chosen agent, different temperatures have to be employed. For potassium doping the temperature is raised up to 873 K with 50 K/h in the first step, up to 923 K with 150 K/h in the second step and annealed for 15 h at 1023 K with a rate of 350 K/h in the final step. Before the third step the powder is pressed into a pellet ( $\varnothing = 10$  mm). After each step the furnaces were cooled down with 200 K/h. Then, the sample is removed from its container and homogenized properly for at least 5 minutes to obtain a good distribution of the doping component. The mixing is enhanced by using small pieces of the starting materials. Therefore,

the dendritic pieces of barium are reduced to small pieces. Arsenic and iron are used as fine powders. The potassium can be added as ingot as it melts at 336.5 K. As a result, a black air-stable powder with no or little impurity phase (Figure 7-5) and a steep superconducting transition (Figure 7-6) is obtained. The crystallographic data are summarized in Table 9-1.

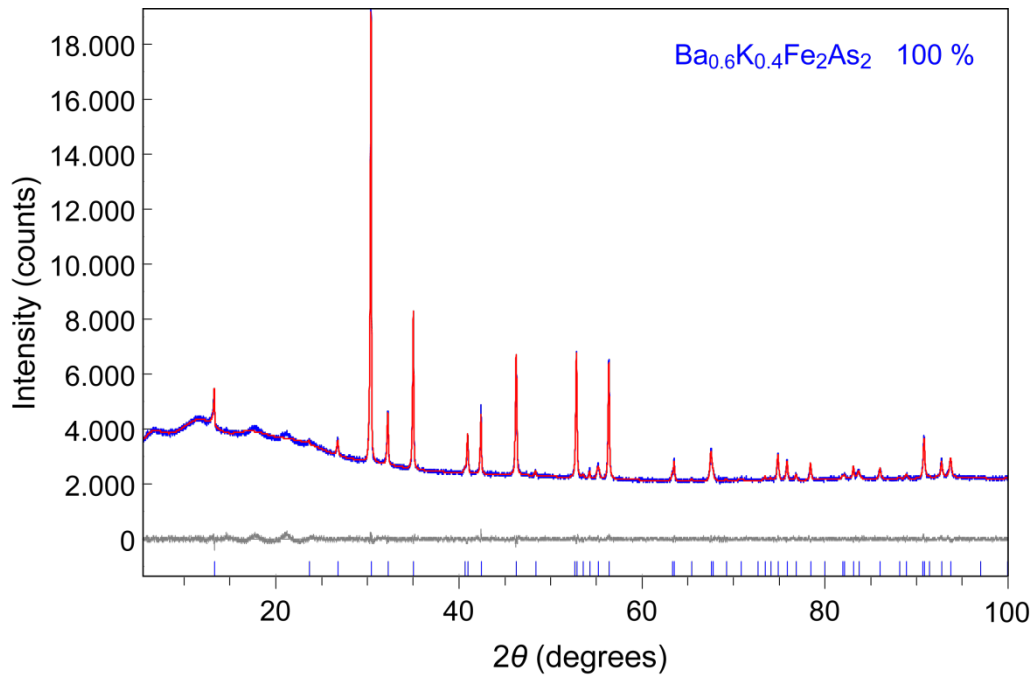


**Figure 7-5:** X-ray powder diffraction pattern (blue) and Rietveld fit (red) of  $\text{Ba}_{0.6}\text{K}_{0.4}\text{Fe}_2\text{As}_2$  powder from element-based synthesis.

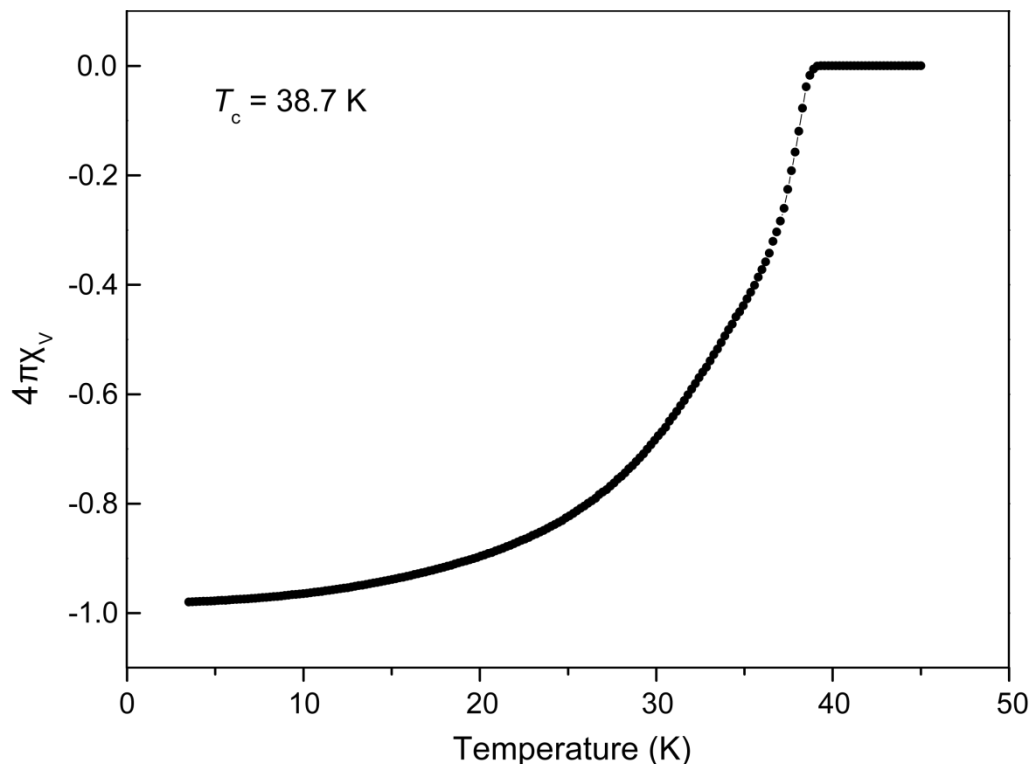


**Figure 7-6:** Susceptibility measurement of  $\text{Ba}_{0.6}\text{K}_{0.4}\text{Fe}_2\text{As}_2$  synthesized from the elements.

## 7.4 Synthesis via mechanical alloying of ternary precursors

This path was chosen because of the crystallographic similarity of the precursors  $\text{BaFe}_2\text{As}_2$  and  $\text{KFe}_2\text{As}_2$  to each other and to the final product, all crystallizing in the same structure type. The idea was that using small well-homogenized particles with the same space group and a similar-sized unit cell might reduce the reaction time and the temperature needed (using binary precursors: 1073 - 1373 K). Furthermore, the evaporation of potassium can possibly be prevented when using the ternary  $\text{KFe}_2\text{As}_2$  as agent for hole doping  $\text{BaFe}_2\text{As}_2$  instead of elemental potassium.

## 7.4.1 Precursor synthesis

### 7.4.1.1 $\text{BaFe}_2\text{As}_2$

Portions of up to 1.5 g of  $\text{BaFe}_2\text{As}_2$  can be produced in a three-step synthesis using stoichiometric mixtures of Ba, Fe, and As. The mixture is heated to 1023 K with a rate of 50 K/h in the first step, to 1173 K with a rate of 150 K/h in the second step, and to 973 K with a rate of 350 K/h in the third step. The annealing time of each step at maximum temperature is 15 h. Between the three annealing steps the ampoule was opened and the compound was homogenized thoroughly as described in 7.3. Before the third step the homogenized powder was pressed into a pellet ( $\varnothing = 10$  mm).

In order to make the precursor synthesis more efficient, the synthetic process was reduced by one step through reducing the size of the barium pieces used and mixing them with the other components before heating them. Simultaneously, the annealing time was raised to 20 hours for each step, at a temperature of 1173 K. The homogenization here is even more crucial for the complete reaction of the elements in order to receive a clean product (Figure 7-7) that can be used for further reactions. The crystallographic data are summarized in Table 9-2 in the Appendix. If not performed properly, the black air-stable product will be contaminated with impurity phases like non-reacted components or binary intermediates.

Both routes lead to high-quality  $\text{BaFe}_2\text{As}_2$  free from impurity phases.

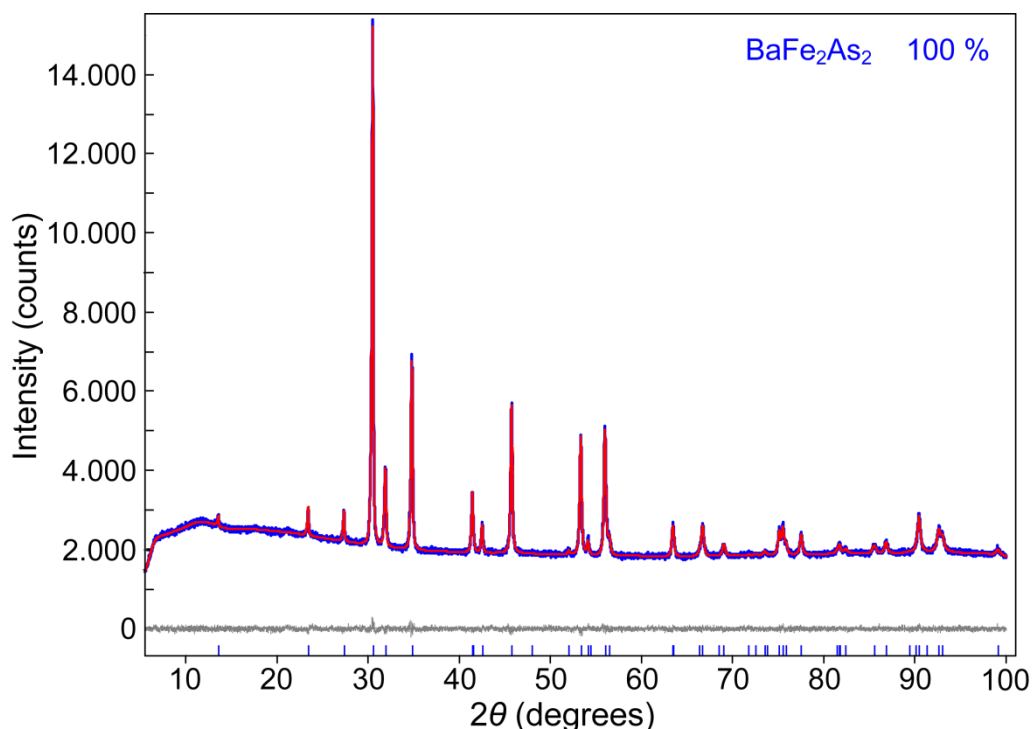


**Figure 7-7: X-ray powder diffraction pattern (blue) and Rietveld fit (red) of  $\text{BaFe}_2\text{As}_2$  powder.**

#### 7.4.1.2 $\text{KFe}_2\text{As}_2$

$\text{KFe}_2\text{As}_2$ , first being synthesized 1981<sup>[139]</sup>, is an air-sensitive superconductor with a critical temperature  $T_c = 3.8 \text{ K}$ <sup>[42]</sup>. It does not undergo a phase transition or exhibit a spin-density wave as  $\text{BaFe}_2\text{As}_2$ .

Portions of up to 1.5 g of  $\text{KFe}_2\text{As}_2$  were produced in a two-step synthesis. It was heated to 873 K with a rate of 50 K/h in the first step and to 923 K with a rate of 150 K/h in the second step. In both steps the maximum temperature was kept for 15 h. Between the two annealing steps, the ampoule was opened and the compound was ground thoroughly. After the second annealing step a black air-sensitive crystalline powder was obtained (Figure 7-8). The crystallographic data are summarized in Table 9-3 in the Appendix.

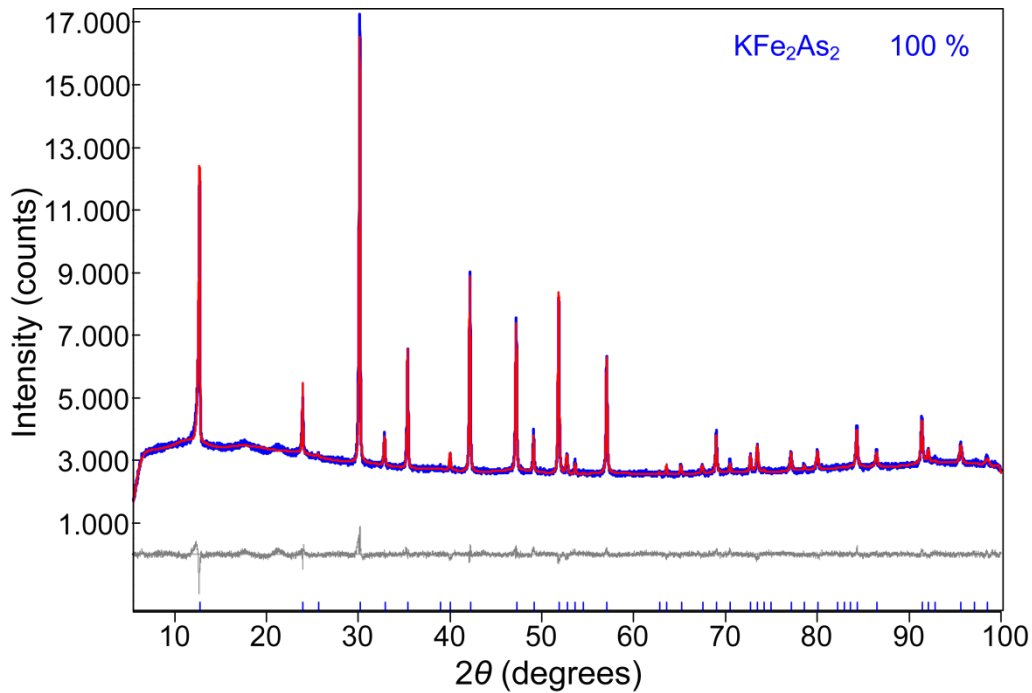


**Figure 7-8:** X-ray powder diffraction pattern (blue) and Rietveld fit (red) of  $\text{KFe}_2\text{As}_2$  powder.

## 7.4.2 Mechanical alloying

### 7.4.2.1 Overview

Solid state reactions are driven by the diffusion of the components. This can be expressed by Fick's first law:

$$J_x = -D \frac{\partial \text{conc}}{\partial x}$$

The diffusion flux  $J_x$ , as a measure for the reaction speed, can be expressed by the concentration gradient  $\partial \text{conc} / \partial x$  (with  $\text{conc}$  being the concentration and  $x$  being the distance) and the diffusion coefficient  $D$ , which depends on the temperature. The flux is thereby directed from higher to lower concentrations. Thus, a faster conversion can be achieved by either raising the reaction temperature or reducing the distance  $x$ , for example by reducing the grain size of the reactants. Raising the annealing temperature in our case leads to an enhanced evaporation of potassium. Thus, the grain size reduction is the only reasonable path to be pursued. One possibility to reduce the particle size is mechanical alloying (ball milling). Additionally, this leads to

a homogeneous mixing of the starting materials. Thereby the reaction time is decreased and the yield of metastable reaction products increases. This leads to a more efficient use of materials, energy, and time<sup>[140-141]</sup>. The compounds to be homogenized are filled into a milling chamber. Additionally, a number of balls is added and the chamber is sealed. The container is then shaken or rotated depending on the type of ball mill for a determined time period. During this motion the balls collide with the chamber's wall and with each other, crushing and merging the powder between the colliding objects. In order to achieve the best result possible, different parameters used in the milling process have to be well chosen. Parameters like the speed of the mill, the milling time, the material of the balls and the container used in the process, the filling ratio of the chamber, the size, and the number of the balls influence the result of the mechanical alloying tremendously.

### 7.4.2.2 Experimental details

In this work the focus lies especially on the speed, the duration of the milling process, and the materials used for the container and the balls. The speed of the ball mill is important for the synthesis. A minimum speed is necessary to obtain the desired sample quality but if the speed is too high this can lead to a decomposition of the starting materials<sup>[141-142]</sup>, due to a significant increase of temperature. The size, density, and the number of balls used in the alloying process can influence the product formation. Choosing large balls with a high density favors thermodynamically stable products<sup>[143-144]</sup>. Small balls on the other hand help creating meta stable or amorphous phases and improve the mixing. Another thing that has to be considered in the mixing is the abrasion of the container and the balls. The rate of wear depends on the used materials, is independent of the milling time, but increases with the speed of the mill<sup>[145]</sup>.

Here two different mixtures of  $BaFe_2As_2/KFe_2As_2$  with a molar ratio of 0.6/0.4 were tested in two different milling processes. One process was performed by *Dr. Marcus Tegel (Fraunhofer Institute for Manufacturing Technology and Advanced Materials, Dresden)* (process A), the other one was performed by *M. Sc. Eike Ahrens (Technical University Dresden)* and *Dr. Jan Engelmann (Leibnitz Institute for Solid*

*State and Material Research*, Dresden) (process B). The parameters for the two different mechanical alloying sequences are given in Table 7-1.

**Table 7-1: Parameters for the alloying sequences.**

	Milling time (min)	Revolution speed (rpm)	Milling pot	Milling balls
Process A	300	600	Stainless steel	Stainless steel
Process B	240	900	ZrO <sub>2</sub>	ZrO <sub>2</sub>

#### 7.4.2.3 Results of milling process A

An XRD pattern of the mixture was recorded before and after the 300 minutes at 600 rpm of mechanical alloying (Figure 7-9).

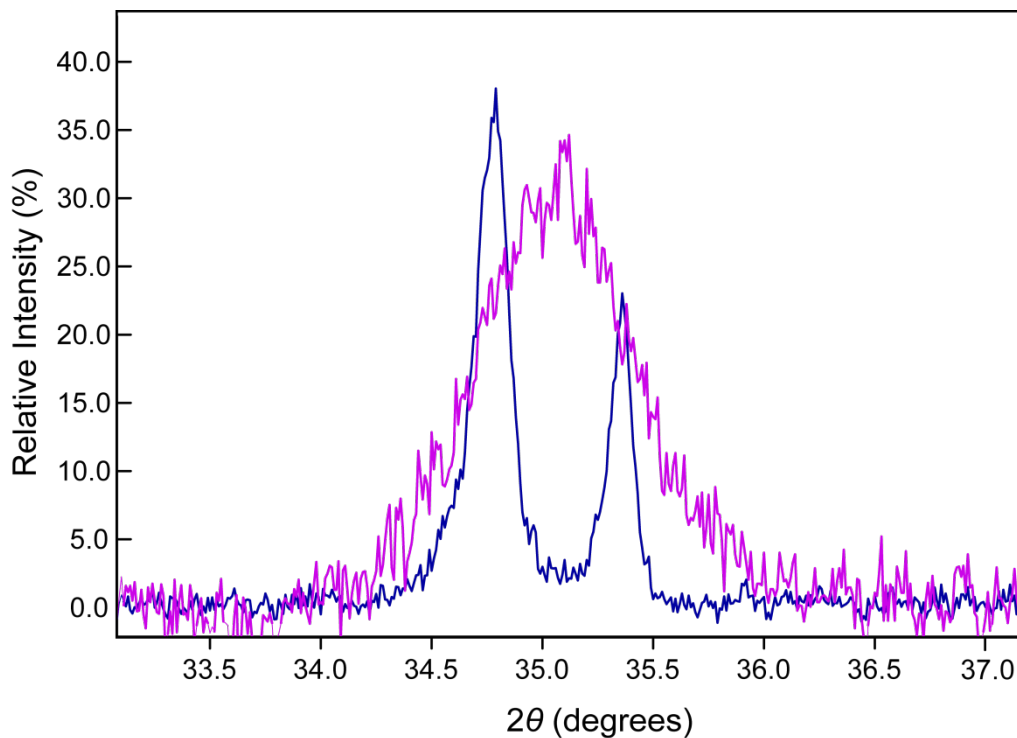


**Figure 7-9:** XRD pattern of the 112 reflections of a  $BaFe_2As_2$ (left)/ $KFe_2As_2$  (right) mixture (ratio: 0.6/0.4) before (blue) and after (purple) the milling process A.

Before milling, clearly two separate 112 reflections, one of  $\text{BaFe}_2\text{As}_2$  (blue curve, left reflection) and one of  $\text{KFe}_2\text{As}_2$  (blue curve, right reflection), can be seen in the XRD pattern. After the process only one broad 112 reflection appears, suggesting a reduction of the particle size. The fact that only one reflection is visible indicates a possible reaction during the mixing process and was checked by a susceptibility measurement (Figure 7-10).

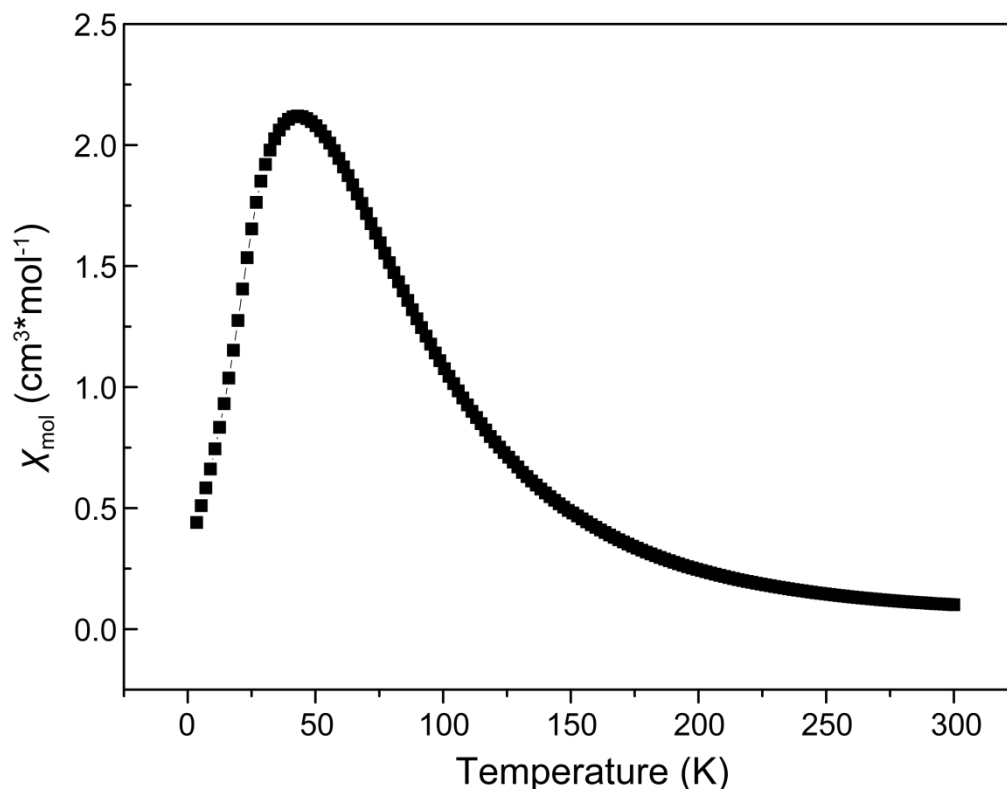


**Figure 7-10: Susceptibility measurement of the  $\text{BaFe}_2\text{As}_2/\text{KFe}_2\text{As}_2$  mixture (ratio: 0.6/0.4) after the milling process A.**

The susceptibility  $\chi$  increases until a temperature of about 43 K is reached. This may be attributed to a ferromagnetic contamination as a result of the wear of the steel balls and the steel milling container. Below 43 K the susceptibility drops. This temperature is 4 K above the  $T_c$  of  $\text{Ba}_{0.6}\text{K}_{0.4}\text{Fe}_2\text{As}_2$ , and therefore the drop cannot be attributed to a superconducting transition. Thus, further annealing is necessary.

The mixture was placed in an alumina crucible, sealed under purified argon in a silica glass ampoule and annealed at a temperature of 973 K for 30 h with a heating rate of 100 K. This temperature was chosen as result of a temperature screening for  $\text{BaFe}_2\text{As}_2/\text{KFe}_2\text{As}_2$  mixtures. In these experiments 500 mg of the mixture were heat treated with different temperatures and durations. Lower temperatures lead to incomplete reactions. Higher temperatures result in high amounts of impurity phases due to evaporation of potassium.

The annealing process A leads to the formation of  $\text{Ba}_{0.6}\text{K}_{0.4}\text{Fe}_2\text{As}_2$  as a main phase with 90.7 wt% and a small half-width of the reflections, which indicates an enhanced grain size. The impurity phase  $\text{Fe}_2\text{As}$  (9.3 wt%) is detected. The origin of  $\text{Fe}_2\text{As}$  is the loss of potassium during annealing, which is verified by chemical analysis.  $\text{Fe}_2\text{As}$  and not  $\text{FeAs}$  occurs due to additional iron from abrasion of the balls and milling container.

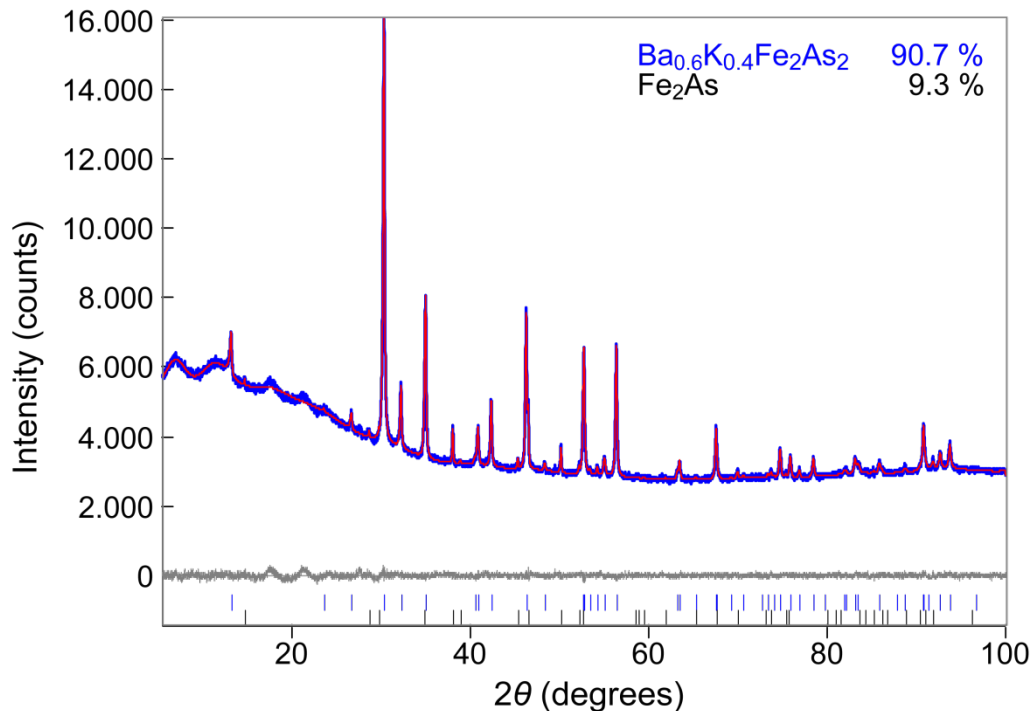


**Figure 7-11: X-ray powder diffraction pattern (blue) and Rietveld fit (red) of the  $\text{BaFe}_2\text{As}_2/\text{KFe}_2\text{As}_2$  mixture after milling process A and the annealing.**

The susceptibility measurement of this sample (Figure 7-12) also indicates a loss of potassium as it reveals a superconducting volume fraction of only about 21 %. The reduced  $T_c = 29.9$  K compared to the transition temperature of  $\text{Ba}_{0.6}\text{K}_{0.4}\text{Fe}_2\text{As}_2$  (38.7 K) implies that less potassium has been included in the compound. In addition, the superconducting transition is broad, extending from  $T_c$  to the lowest measured temperature at 3.5 K, indicating an inhomogeneous potassium distribution. Also, a second transition is observed around 10 K.

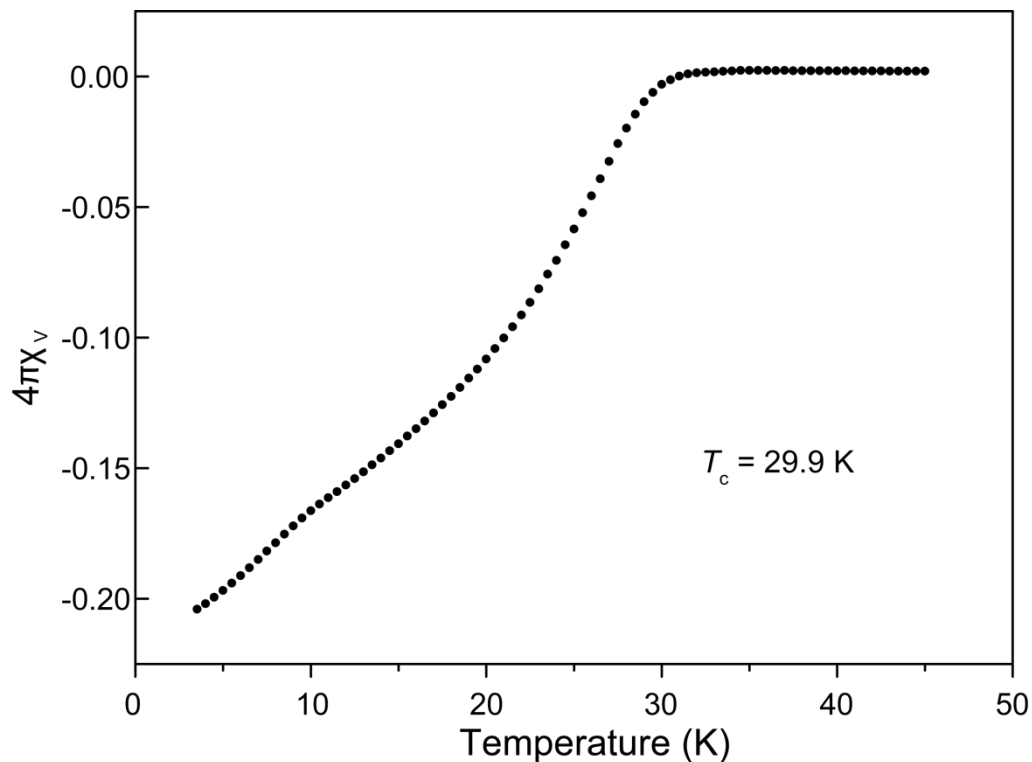


**Figure 7-12: Susceptibility measurement of a  $\text{BaFe}_2\text{As}_2/\text{KFe}_2\text{As}_2$  mixture after milling process A and the annealing.**

#### 7.4.2.4 Results of milling process B

To avoid the abrasion,  $\text{ZrO}_2$  was chosen as ball and container material instead of steel, the milling time was reduced to 240 minutes and the revolution speed was raised to 900 rpm to obtain a good homogenization. An XRD measurement of the mixture before and after the milling process B shows a less drastic change of the 112 reflections compared to process A (Figure 7-13).

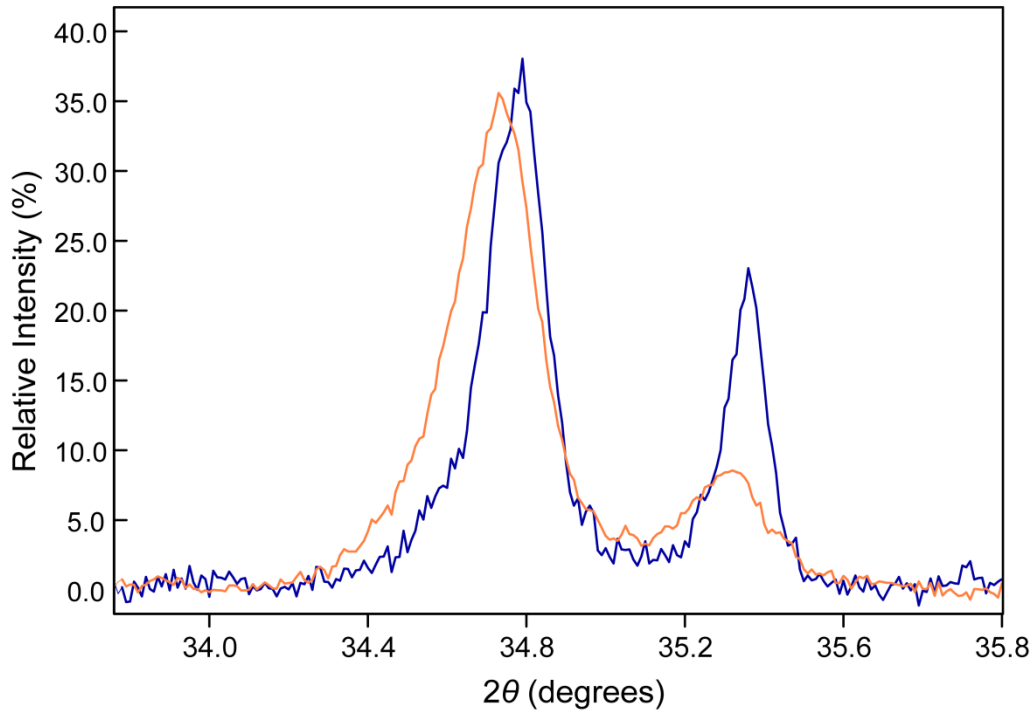


**Figure 7-13: XRD measurement of the 112 reflections of a  $\text{BaFe}_2\text{As}_2$ (left)/ $\text{KFe}_2\text{As}_2$  (right) mixture (ratio: 0.6/0.4) before (blue) and after (orange) the milling process B.**

A broadening of the reflections is also visible after the milling process B but in contrast to process A both 112 reflections can still be distinguished after the milling and no reaction of the precursors is observed. In process B especially the 112 reflection of  $\text{KFe}_2\text{As}_2$  seems to be affected by the alloying, as this compound is softer. Before and after the alloying, no additional reflections evolve that could be attributed to wear of the balls or the milling chamber.

The susceptibility measurement (Figure 7-14) after the mechanical alloying reveals a small ferromagnetic impurity due to a shift of the susceptibility up to 0.002. This impurity has not been detected in the powder diffraction pattern. Also, only the superconducting transition of  $\text{KFe}_2\text{As}_2$  at 3.8 K is observed. Subsequently, the mixture was annealed in order to achieve a reaction of the precursors into  $\text{Ba}_{0.6}\text{K}_{0.4}\text{Fe}_2\text{As}_2$ .

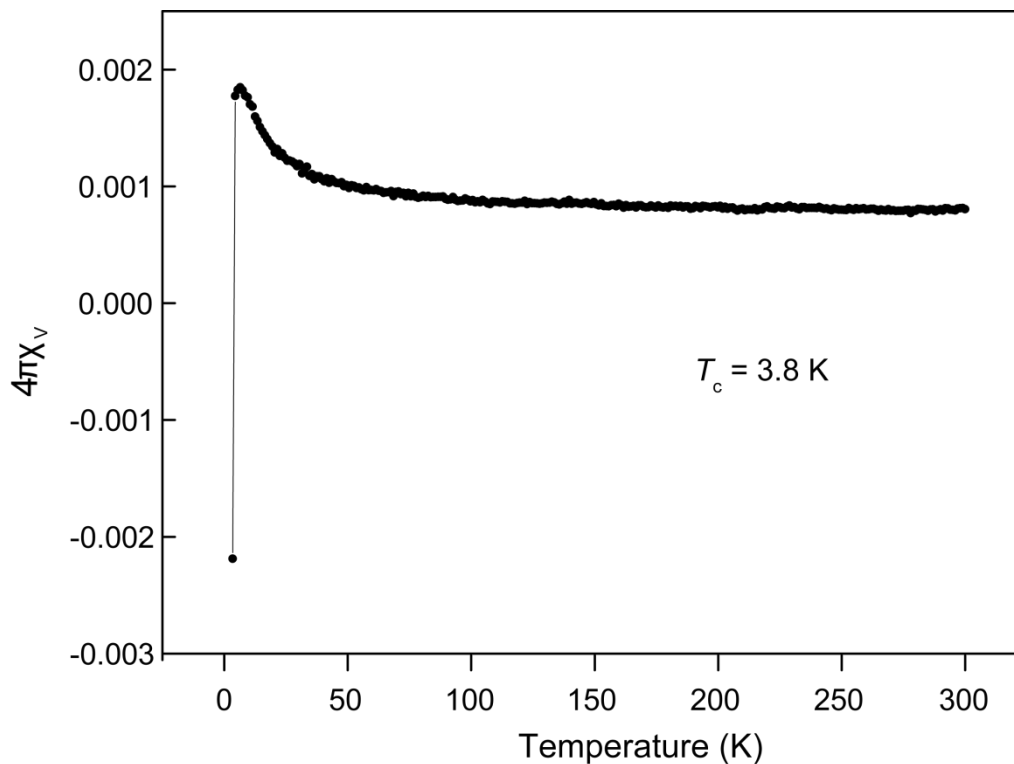


**Figure 7-14: Susceptibility measurement of the  $\text{BaFe}_2\text{As}_2/\text{KFe}_2\text{As}_2$  mixture (ratio: 0.6/0.4) after the application of process B.**

For reasons of comparison the same temperature program as in process A was chosen.  $\text{Ba}_{0.6}\text{K}_{0.4}\text{Fe}_2\text{As}_2$  was obtained as the main phase with 91.2 wt% (Figure 7-15). Again, an impurity phase evolved during the annealing process, verified by chemical analysis. But in contrast to process A, FeAs emerges instead of  $\text{Fe}_2\text{As}$  with 8.8 wt%. Before the heat treatment no impurity phase was detected. Thus, as in process A, this occurs due to the potassium evaporation during the annealing process. But by using  $\text{ZrO}_2$  as material for the milling chamber and balls the evolution of  $\text{Fe}_2\text{As}$  is prevented by eliminating the abrasion during the milling process.

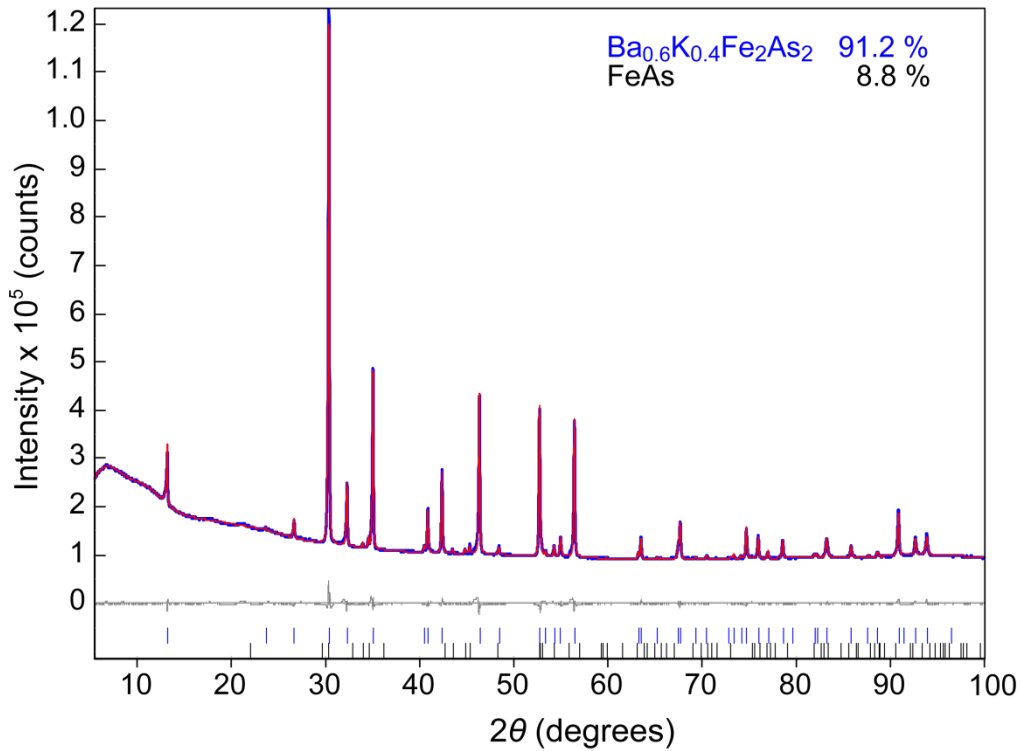


**Figure 7-15: X-ray powder diffraction pattern (blue) and Rietveld fit (red) of the  $\text{BaFe}_2\text{As}_2/\text{KFe}_2\text{As}_2$  mixture after milling process B and the annealing.**

The susceptibility measurement after the annealing shows major differences to the measurement after process A. The superconducting temperature is 38.6 K as expected for optimal doping, and the superconducting transition indicates a homogeneous potassium distribution. Moreover, the superconducting volume fraction in process B is 67 % proving bulk superconductivity. The missing volume fraction can be attributed to the impurity phase (6 vol%) and also to experimental parameters like the packing density of the powder.

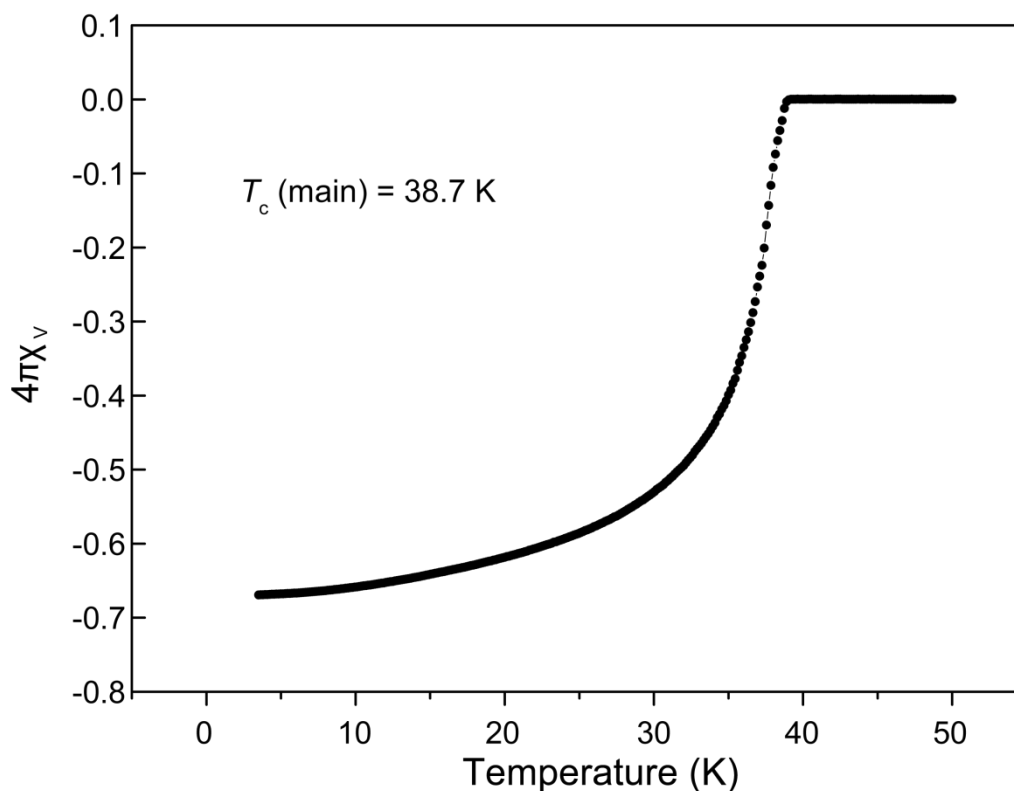


**Figure 7-16: Susceptibility measurement of a  $\text{BaFe}_2\text{As}_2/\text{KFe}_2\text{As}_2$  mixture after milling process B and the annealing.**

## 7.5 Discussion

Both, the element-based synthesis and the one using precursors lead to  $\text{Ba}_{1-x}\text{K}_x\text{Fe}_2\text{As}_2$  as the main phase. The advantage of the element-based synthesis is that no or little impurity phase is obtained. By slowly raising the temperature from 873 K to 923 K and 1023 K the potassium can mostly be restrained from evaporating, while the temperature is high enough for the barium to become mobile. A uniform Ba/K distribution is further achieved by the thorough homogenization of the products after each step. Sample quantities of up to 1.5 g with reproducibly high quality can be produced by this pathway making it perfect for the investigation of most of its physical properties.

For higher quantities of  $\text{Ba}_{1-x}\text{K}_x\text{Fe}_2\text{As}_2$  the second pathway presented here was developed. The precursors  $\text{BaFe}_2\text{As}_2$  and  $\text{KFe}_2\text{As}_2$  can be produced via conventional solid state reactions in high quantities free from impurities. Using individual temperatures for each precursor prevents the potassium in  $\text{KFe}_2\text{As}_2$  from evaporation

and supports a good formation of  $\text{BaFe}_2\text{As}_2$ . Using the precursors also simplifies the weighing process.

A key feature for the successful conversion is the homogenization achieved by the mechanical alloying. Comparing the materials used in the milling processes, the harder  $\text{ZrO}_2$  is the preferable choice compared to stainless steel. Using steel balls and mill leads to abrasion and enhances the formation of  $\text{Fe}_2\text{As}$ . In process A a particle size distribution between about  $10\ \mu\text{m}$  and less than  $1\ \mu\text{m}$  was observed, while in process B also larger particles were found and the amount of larger particles in contrast to process A is enhanced (Figure 7-17).

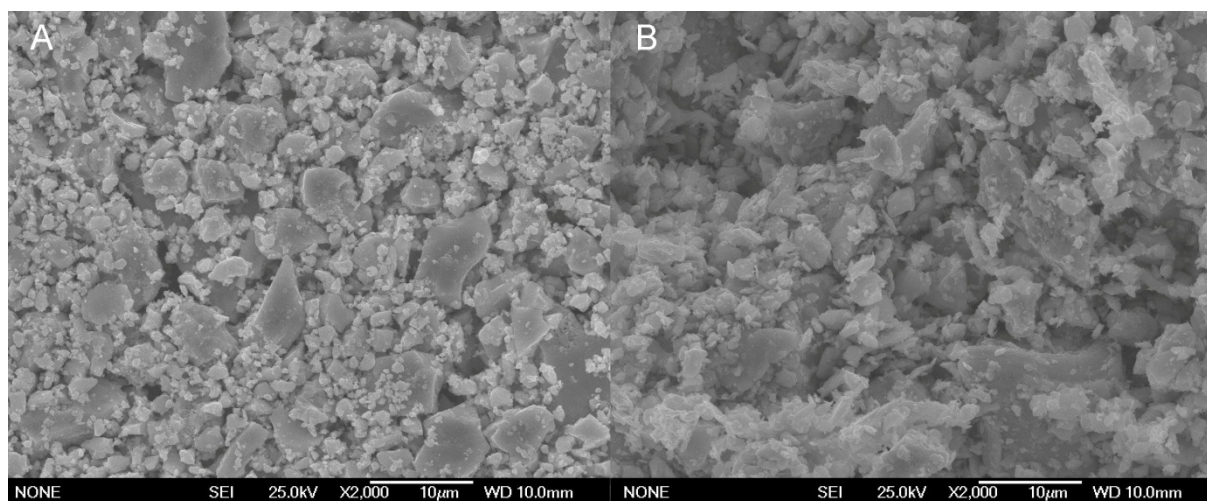


**Figure 7-17: SEM images of the precursor mixture after milling process A (left) and milling process B (right).**

This result was also shown in the XRD patterns recorded for each mixture leading to more or less broadened reflections. Still, after both steps of mechanical alloying further annealing was necessary. In both samples the Rietveld refinements show that  $\text{Ba}_{0.6}\text{K}_{0.4}\text{Fe}_2\text{As}_2$  was maintained as main phase. But both samples were contaminated with  $\text{Fe}_2\text{As}$  (process A) and  $\text{FeAs}$  (process B) in a similar amount. As stated before, the additional Fe in process A was most likely incorporated because of abrasion during the milling. Nevertheless, the susceptibility measurements revealed the significant difference. While the susceptibility for the sample treated by process B

displayed bulk superconductivity and a  $T_c$  of 38.6 K, the sample treated by process A showed a  $T_c$  of only 29.9 K, a superconducting volume fraction of only about 21 %, and a broad superconducting drop with two transitions.

Chemical analysis revealed that the potassium loss in process A and process B happens during the annealing, since both mixtures display the Ba/K ratio of 0.6/0.4 before the heat treatment. Therefore, the annealing step needs further optimization for example by implementing intermediate temperature steps comparable to the different annealing temperatures in the element-based synthesis to further reduce the potassium loss. Still, process B with its high  $T_c$  and its narrow superconducting transition is the better path to pursue for the production of larger amounts of high-quality  $\text{Ba}_{0.6}\text{K}_{0.4}\text{Fe}_2\text{As}_2$ .

## 8 Summary and outlook

The results presented in this thesis provide a deeper insight into the physical properties of  $\text{Ba}_{1-x}\text{K}_x\text{Fe}_2\text{As}_2$  and their connection among each other. By using a combination of high resolution X-ray diffraction, susceptibility measurements, and  $\mu\text{SR}$ , it was possible to unambiguously identify a microscopic coexistence of superconductivity and antiferromagnetism in underdoped  $\text{Ba}_{1-x}\text{K}_x\text{Fe}_2\text{As}_2$  (up to  $x = 0.23$ ). This result strongly supports the assumption of an  $s_{\pm}$ -wave symmetry in this area of the phase diagram. These studies were extended to the optimally and overdoped  $\text{Ba}_{1-x}\text{K}_x\text{Fe}_2\text{As}_2$  up to  $x = 0.66$ , generating a phase diagram displaying gradual transitions from long-range to short-range order instead of sharp borders. This magnetic order can be detected up to at least  $x = 0.66$ , a value beyond the expected one (between 0.2 and 0.3). On  $\text{Ba}_{0.8}\text{K}_{0.2}\text{Fe}_2\text{As}_2$  under pressure, a new antiferromagnetic order AFM2 was discovered, also displaying coexistence with superconductivity.

In the second part of this thesis,  $\text{Ba}_{0.6}\text{K}_{0.4}\text{Fe}_2\text{As}_2$  was examined as material for the production of superconducting wires and tapes. Preliminary critical current density measurements of these prototype filaments are encouraging. To further investigate these wires, a new synthesis route was explored using mechanical alloying of the ternary precursors  $\text{BaFe}_2\text{As}_2$  and  $\text{KFe}_2\text{As}_2$  in order to obtain larger sample amounts.

### **Microscopic coexistence of superconductivity and magnetism in $\text{Ba}_{1-x}\text{K}_x\text{Fe}_2\text{As}_2$**

On four high-quality samples of  $\text{Ba}_{1-x}\text{K}_x\text{Fe}_2\text{As}_2$  ( $x = 0, 0.19, 0.23, 0.25$ ) low-temperature XRD measurements were performed revealing a structural transition from  $I4/mmm$  to  $Fmmm$  below 140 K. The origin of this structural transition is an antiferromagnetic ordering of the iron atoms below 138 K. With increasing potassium content the magnetism is weakened, the structural transition temperature decreases from  $T_s = 140$  K ( $x = 0$ ) to 98 K ( $x = 0.19$ ), 84 K ( $x = 0.23$ ), and 70 K ( $x = 0.25$ ) and superconductivity is induced with increasing  $T_c = 22.7$  K ( $x = 0.19$ ), 28.5 K ( $x = 0.23$ ) and 32.6 K ( $x = 0.25$ ). Alongside with the reduction of  $T_s$  also the structural order

parameter  $\delta$  diminishes with rising potassium content. Interestingly, when reaching  $T_c$ ,  $\delta$  is slightly decreased, indicating a competition of the structural and magnetic order parameter with the superconducting one. Muon spin rotation measurements reveal information about the magnetic volume fraction of the samples with  $x = 0, 0.19, 0.23$ . After an initially slow evolution of the magnetic phases, the magnetic fractions increase up to  $T_N^{50\%}$  until they saturate at almost 100 % at 1.6 K. Simultaneously susceptibility data exhibits superconducting volume fractions of nearly 100 %, proving unequivocally that both properties coexist on a microscopic scale.

### **Short-range magnetic order in $\text{Ba}_{1-x}\text{K}_x\text{Fe}_2\text{As}_2$**

Throughout the investigated range of the phase diagram ( $0 \leq x \leq 0.66$ ) a nematic phase is detected, preceding the transition into an antiferromagnetic state. Beyond the underdoped area of the phase diagram, the  $T_c$ s rise up to  $x = 0.4$ , reaching a maximum at  $T_c = 38.7$  K, then decrease first slowly for  $x = 0.5$  ( $T_c = 37.4$  K) and then with an increasing rate for  $x = 0.6$  ( $T_c = 31.1$  K) and  $0.66$  ( $T_c = 23.3$  K). All superconducting volume fractions display bulk superconductivity. At the same time higher-doped compounds ( $x > 0.23$ ) exhibit an increasing non-magnetic fraction with increasing potassium content, indicating a phase separation into a non-magnetic superconducting phase and magnetic clusters that coexist with superconductivity. The dips in the curves coincide with the superconducting transition temperatures, demonstrating the competition of both magnetism and superconductivity in these clusters. In contrast to the common belief, the magnetic fraction does not vanish completely in the optimally and overdoped area but remains present throughout the whole investigated range (up to  $x = 0.66$ ). Only the nature of the antiferromagnetism changes from a long-range order up to  $x = 0.27$ , to a short-range order for  $0.27 \leq x \leq 0.66$ . Both the short-range order and the phase separation point to an avoided quantum critical point around  $x = 0.3$ . The overdoped compounds ( $x = 0.5, 0.6, \text{ and } 0.66$ ) were further analyzed concerning a possible transition of the superconducting wave function from an *s*- to a *d*-wave. For  $x = 0.5, 0.6$  the superfluid density measurements could be fitted best with *s*-wave functions, while for  $x = 0.66$  a *d*-wave seems to be preferable.

### Rise of a new magnetic phase in $\text{Ba}_{0.8}\text{K}_{0.2}\text{Fe}_2\text{As}_2$

$\mu\text{SR}$  measurements under pressure indicate the rise of a new antiferromagnetic phase AFM2 on the expense of the antiferromagnetic phase at ambient pressure, AFM1. This new phase differs from recently found tetragonal pockets in  $\text{Ba}_{1-x}\text{K}_x\text{Fe}_2\text{As}_2$  due to its spin structure, being the same as in AFM1 (along the  $ab$ -plane), but with lower magnetic moments. AFM2 is phase separated from AFM1 but coexists with the superconducting phase on a microscopic scale. First hints of AFM2 are observed at 20 K and 2.6 kbar and the phase becomes clearly visible at 5.3 kbar. With increasing pressure the new phase becomes more and more distinct, while the frequencies of AFM1 shift towards lower values and become less pronounced but are still existent at 22.1 kbar. At maximum pressure the AFM1 frequencies broaden at 20 K with rising temperature but the order exists up to 95.5 K. In contrast to that, AFM2 is first affected by an increase of temperature at 40 K but already disappears completely above 50 K.

### Exploring the potential of $\text{Ba}_{0.6}\text{K}_{0.4}\text{Fe}_2\text{As}_2$ wires and tapes

This material was chosen for production of filaments because of its low crystallographic anisotropy, high upper critical field  $H_{C2}$ <sup>[127]</sup> and the robustness to impurity phases<sup>[128]</sup>. Here important factors for the wire/tape manufacturing and the physical properties of these wires and tapes concerning the grain connectivity, superconductivity, and critical current density were investigated.

This was enabled by the up-scaling of the synthesis process (in total about 20 g of  $\text{Ba}_{0.6}\text{K}_{0.4}\text{Fe}_2\text{As}_2$ ), simultaneously ensuring a high quality of the material.

The best results concerning the heat treatment (performed to improve the grain connectivity and enhance  $J_c$ ) after the cold working were obtained for samples annealed at 1073 K. An oxygen- and water-free atmosphere for the annealing process is mandatory. The samples displayed a high shielding fraction and a  $T_c = 37.7$  K. In lower-doped samples the grain connectivity was insufficient. For the samples annealed at higher temperatures large areas of FeAs and  $\text{Fe}_2\text{As}$  were detected. A detailed microstructural analysis shows a homogeneous distribution of

the elements, a slight misalignment of the grains with semi- and incoherent grain boundaries, and an orientation almost parallel to the direction of the elongation for the compound heated at 1073 K.

Concerning the deformation process it was shown that groove rolling alone leads to a high core density, but also to transversal cracks that inhibit the current flow. A drawing of the wire results in uniform but less dense cores and also introduces cracks. These cracks are longitudinal to the drawing axis and should not hinder the current flow. The best result was obtained by a combination of groove rolling, flat rolling, and then annealing at 1073 K, leading to a dense core with almost no cracks. This was also confirmed by measuring critical current densities above  $1 \times 10^4$  A/cm<sup>2</sup> at low magnetic fields. The received  $n$ -factor for the best filament is around 30, proving the homogeneous distribution of the elements and empowering it as a material that can be used in constant mode. Comparing these values to the literature, we see that  $J_c$  is lower than in [68], but  $T_c$  is higher. It is the highest  $T_c$  measured up to now for Ba<sub>0.6</sub>K<sub>0.4</sub>Fe<sub>2</sub>As<sub>2</sub> wires and tapes, probably as a result of the optimized reaction conditions and the high quality material.

### **Optimizing the synthesis process of Ba<sub>1-x</sub>K<sub>x</sub>Fe<sub>2</sub>As<sub>2</sub>**

Two different processes were developed in order to improve and up-scale the synthesis process. One element-based and one via mechanical alloying of the ternary precursors BaFe<sub>2</sub>As<sub>2</sub> and KFe<sub>2</sub>As<sub>2</sub>.

The element-based synthesis was based on the three-step synthesis developed by *Rotter et al.* [17]. Using a moderate temperature of 873 K with a slow rate of 50 K/h in the first step, 923 K and a rate of 150 K/h in the second step, and 1023 K and a rate of 350 K/h in the third step allows a slow and steady reaction of the elements and minimizes a potential element loss. Decisive for the successful conversion into a homogeneous sample is the thorough homogenization of the mixtures after each step. Through this improvement high-quality powder samples with a homogeneous Ba/K distribution and no or very little impurity phase could be obtained. Limited by the size of the crucible, sample sizes of up to 1.5 g could be produced.

An alternative path to synthesize  $\text{Ba}_{0.6}\text{K}_{0.4}\text{Fe}_2\text{As}_2$  is mechanical alloying of  $\text{BaFe}_2\text{As}_2$  and  $\text{KFe}_2\text{As}_2$  as ternary precursors before annealing. Both precursors can be produced in large quantities and high quality in a two-step synthesis.  $\text{BaFe}_2\text{As}_2$  and  $\text{KFe}_2\text{As}_2$  were then mechanically alloyed in two different processes (A and B). Process A was performed with a milling chamber and milling balls made of stainless steel. After the annealing of this mixture  $\text{Ba}_{0.6}\text{K}_{0.4}\text{Fe}_2\text{As}_2$  was obtained as the main phase (91 wt%), but also the impurity phase  $\text{Fe}_2\text{As}$  evolved (additional Fe because of abrasion) and the superconducting properties with a volume fraction of only 20 % and a  $T_c = 29.9$  K were unsatisfactory.

Process B used  $\text{ZrO}_2$  milling chamber and balls. After the heat treatment  $\text{Ba}_{0.6}\text{K}_{0.4}\text{Fe}_2\text{As}_2$  was obtained as the main phase (more than 91 wt%) with the impurity phase  $\text{FeAs}$ . This material shows bulk superconductivity with a narrow transition indicating a homogeneous Ba/K distribution and  $T_c = 38.7$  K. By optimizing the heat treatment the amount of impurity phase has to be reduced further. However, the superconducting properties after the heat treatment in process B display that it is a promising path to larger quantities of  $\text{Ba}_{0.6}\text{K}_{0.4}\text{Fe}_2\text{As}_2$ , to further investigate the potential for future application.

## Outlook

The phase diagram of  $\text{Ba}_{1-x}\text{K}_x\text{Fe}_2\text{As}_2$  turned out to be significantly more complicated than expected earlier. Recently published results observing a tetragonal magnetic pocket in underdoped  $\text{Ba}_{1-x}\text{K}_x\text{Fe}_2\text{As}_2$ <sup>[95]</sup> underline this and should be investigated further. These pockets are in line with findings in the  $\text{Ba}_{1-x}\text{Na}_x\text{Fe}_2\text{As}_2$  phase diagram. Thus it would be interesting to also examine  $\text{Ba}_{1-x}\text{Na}_x\text{Fe}_2\text{As}_2$  concerning the new magnetic phase under pressure and see if this phase is an intrinsic feature of hole-doped  $\text{BaFe}_2\text{As}_2$ . Although the experimental results in the underdoped area support the  $s\pm$ -wave scenario, the indications of a transition to  $d$ -wave have to be analyzed in more detail towards the concentration of its appearance and its nature. Also, the evolution of the magnetic fluctuations in samples with  $0.66 > x > 1$  should be further examined to see at which potassium concentration the fluctuation vanishes completely.

The optimized synthesis processes allow to further improve the critical current density of  $\text{Ba}_{0.6}\text{K}_{0.4}\text{Fe}_2\text{As}_2$ -based wires/tapes. It should be examined if by additional deformation of the tapes to diameters smaller than 0.4 mm,  $J_c$  is increased. This could be either achieved by an additional sheath or higher deformation forces. If by force no further compaction can be obtained,  $J_c$  could be increased by radiation-induced pinning centers as recently shown in [146]. Moreover, directly converting the mechanically alloyed mixture of  $\text{BaFe}_2\text{As}_2$  and  $\text{KFe}_2\text{As}_2$  in a tube, in an oxygen- and water-free environment, drawn, flat rolled, and finally annealed, could lead to dense core structures without cracks.

The interaction of the interplay of superconductivity and magnetism in  $\text{Ba}_{1-x}\text{K}_x\text{Fe}_2\text{As}_2$  is unraveled bit by bit and provides a more detailed picture of how superconductivity works in  $\text{Ba}_{1-x}\text{K}_x\text{Fe}_2\text{As}_2$ . If the above-mentioned problems concerning a possible application are solved, this compound could find its way into future devices. This step may take some time, but  $\text{Ba}_{0.6}\text{K}_{0.4}\text{Fe}_2\text{As}_2$  filaments could help to use energy more efficiently. Referring to climate warming, as mentioned in the introduction,  $\text{Ba}_{0.6}\text{K}_{0.4}\text{Fe}_2\text{As}_2$  will not avert the climate change by itself, but it still has the potential to contribute to it.

## 9 Appendix

**Table 9-1: Crystallographic data of Ba<sub>0.6</sub>K<sub>0.4</sub>Fe<sub>2</sub>As<sub>2</sub> from element-based synthesis.**

Ba <sub>0.6</sub> K <sub>0.4</sub> Fe <sub>2</sub> As <sub>2</sub> .	
Space group	<i>I4/mmm</i> (Nr.139)
Z	2
Lattice parameters (Å)	<i>a</i> = 3.914 (1), <i>c</i> = 13.308 (1)
Cell volume (Å <sup>3</sup> )	203.9 (1)
Atomic parameters	
Ba, K	2 <i>a</i> (0, 0, 0)
Fe	4 <i>d</i> (0.5, 0, 0.25)
As	4 <i>e</i> (0, 0, 0.35432 (6))
Ba/K ratio	0.62 (3)/0.38 (3)
<i>R</i> <sub>wp</sub> / <i>R</i> <sub>p</sub>	0.0154/0.0121
$\chi^2$ / <i>R</i> <sub>Bragg</sub>	0.640/0.0065
<i>U</i> <sub>iso</sub> (pm <sup>2</sup> )	Ba/K 111 (5) Fe 35 (4) As 38 (4)
Detected phases	Ba <sub>0.6</sub> K <sub>0.4</sub> Fe <sub>2</sub> As <sub>2</sub> 97.2 wt% FeAs 2.8 wt%

**Table 9-2: Crystallographic data of BaFe<sub>2</sub>As<sub>2</sub>.**

BaFe <sub>2</sub> As <sub>2</sub>	
Space group	<i>I4/mmm</i> (Nr.139)
Z	2
Lattice parameter (Å)	<i>a</i> = 3.961 (1), <i>c</i> = 13.021 (4)
Cell volume (Å <sup>3</sup> )	204.3 (1)
Atomic parameters	
Ba	2 <i>a</i> (0, 0, 0)
Fe	4 <i>d</i> (0.5, 0, 0.25)
As	4 <i>e</i> (0, 0, 0.35393 (5))
<i>R</i> <sub>wp</sub> / <i>R</i> <sub>p</sub>	0.0152/0.0120
$\chi^2$ / <i>R</i> <sub>Bragg</sub>	0.709/0.0046
<i>U</i> <sub>iso</sub> (pm <sup>2</sup> )	Ba 76 (3) Fe 59 (4) As 50 (3)
Detected phases	BaFe <sub>2</sub> As <sub>2</sub> 100 wt%

**Table 9-3: Crystallographic data of  $\text{KFe}_2\text{As}_2$ .**

$\text{KFe}_2\text{As}_2$	
Space group	$I4/mmm$ (Nr.139)
Z	2
Lattice parameter (Å)	$a = 3.914$ (1), $c = 13.308$ (1)
Cell volume (Å <sup>3</sup> )	205.0 (1)
Atomic parameters	
Ba, K	2a (0, 0, 0)
Fe	4d (0.5, 0, 0.25)
As	4e (0, 0, 0.35257 (5))
$R_{wp} / R_p$	0.0149/0.0117
$\chi^2 / R_{Bragg}$	0.815/0.0936
$U_{iso}$ (pm <sup>2</sup> )	K 167 (6) Fe 141 (3) As 111 (3)
Detected phases	$\text{KFe}_2\text{As}_2$ 100 wt%

## 10 Abbreviations

2D	two-dimensional
$2\theta$	diffraction angle
3D	three-dimensional
$4\pi\chi$	magnetic (e.g. superconducting) volume fraction
$a^{1/n}$	sample size dependence
$a, b, c$	lattice parameters
Å	Angström
AC	alternating current
ARPES	angle resolved photoemission spectroscopy
BCS	acronym of Bardeen, Cooper, and Schrieffer
$B...$	magnetic flux density
Bi-2212	$\text{Bi}_2\text{Sr}_2\text{CaCu}_2\text{O}_8$
Bi-2223	$\text{Bi}_2\text{Sr}_2\text{Ca}_2\text{Cu}_3\text{O}_{10}$
$\delta$	a measure for the orthorhombic lattice distortion
$D$	diffusion coefficient
DC	direct current
$E$	energy
EDX	energy dispersive X-ray spectroscopy
$E_F$	Fermi energy

EFTEM	energy filtered transmission electron microscopy
g	gram(s)
$\gamma$	gyromagnetic ratio
$H$	magnetic field
$H_{\text{ext}}$	external magnetic field
$H_c$	critical magnetic field
$H_{c2}$	upper critical field (type 2 superconductor)
HAADF	high angle annular dark field
HRTEM	high resolution transmission electron microscopy
$I$	electric current
$I_c$	critical electric current
ICP-AAS	Induced coupled plasma atomic absorption spectroscopy
$J$	current density
$J_x$	diffusion flux
$J_c$	critical current density
K	Kelvin
$\lambda$	wavelength
LF	longitudinal field
LMU	Ludwig-Maximilians-Universität
$m^*$	effective mass of the superconducting carriers
$\mu$	muon

$\mu\text{s}$	microsecond(s)
$\mu\text{SR}$	muon spin rotation and relaxation
ns	nanosecond(s)
$n_s$	superfluid density
NMR	nuclear magnetic resonance
$N_B(t)$	count rate of the backward detector
$N_F(t)$	count rate of the forward detector
$\nu$	neutrino
$\omega_L$	Larmor frequency
$\omega_\mu$	muon frequency
pm	picometer
$\pi$	pion
$P(t)$	Polarization of the muons
$R\dots$	residual value
RBEI	Rutherford backscattered electron imaging
SDW	spin-density wave
SEM	scanning electron microscopy
$\sigma_{\text{sc}}$	muon spin relaxation rate
STEM	scanning transmission electron microscopy
T	Tesla
$t$	time

$T_c$	critical temperature
TEM	transmission electron microscopy
TF	transverse field
$T_N$	Néel temperature
$T_N^{10\%}$	Temperature where 10 % of a sample are magnetically ordered
$T_N^{50\%}$	Temperature where 50 % of a sample are magnetically ordered, also structural transition temperature in $Ba_{1-x}K_xFe_2As_2$
$T_N^{90\%}$	Temperature where 90 % of a sample are magnetically ordered
$T_s/T_{tr}$	(tetragonal-to-orthorhombic) structural transition temperature
$U$	electric voltage
$U_{iso}$	thermal displacement value
$V$	Voltage
vol%	volume per cent
wt%	weight per cent
wTF	weak transverse field
$x$	distance
$\chi$	magnetic susceptibility per volume (equivalent to $\chi_V$ )
$\chi^2$	goodness of fit
YBCO	$YBa_2Cu_3O_{7-x}$
$Z$	number of empirical formulas per unit cell
ZF	zero field

## 11 Scientific contributions

### Publications

#### **Microscopic co-existence of superconductivity and magnetism in $\text{Ba}_{1-x}\text{K}_x\text{Fe}_2\text{As}_2$**

E. Wiesenmayer, H. Luetkens, G. Pascua, R. Khasanov, A. Amato, H. Potts, B. Banusch, H.-H. Klaus, D. Johrendt, *Phys Rev. Lett.*, **2011**, *107*, 237001. (chapter 3)

#### **Role of heat and mechanical treatments in the fabrication of superconducting $\text{Ba}_{0.6}\text{K}_{0.4}\text{Fe}_2\text{As}_2$ ex-situ Powder-In-Tube tapes**

A. Malagoli, E. Wiesenmayer, S. Marchner, D. Johrendt, A. Genovese, M. Putti  
*Superconductor Science and Technology*, accepted; *arXiv: 1507.03781* **2015**.  
(chapter 6)

#### **Short range magnetic order in overdoped $\text{Ba}_{1-x}\text{K}_x\text{Fe}_2\text{As}_2$ ( $0 \geq x \geq 0.66$ )**

E. Wiesenmayer, G. Pascua, F. Hummel, H. Luetkens, Z. Guguchia, A. Binek, U. Pachmayr, T. Hermann, T. Goltz, R. Khasanov, A. Amato, H. Maeter, H.-H. Klaus, D. Johrendt.  
*in preparation* (chapter 4)

#### **Rise of a new magnetic phase in $\text{Ba}_{0.8}\text{K}_{0.2}\text{Fe}_2\text{As}_2$**

E. Wiesenmayer, G. Pascua, H. Luetkens, D. Bessinger, T. Hermann, Z. Shermadini, R. Khasanov, A. Amato, H.-H. Klaus, D. Johrendt.  
*in preparation* (chapter 5)

#### **Efficient Planar Heterojunction Perovskite Solar Cells Based on Formamidinium Lead Bromide.**

F. C. Hanusch, E. Wiesenmayer, E. Mankel, A. Binek, P. Angloher, C. Fraunhofer, N. Giesbrecht, J. M. Feckl, W. Jaegermann, D. Johrendt, T. Bein, and P. Docampo *J. Phys. Chem. Lett.* **2014**, *5*, 2791–2795.

## Conference contributions

D. Bichler, E. Wiesenmayer, D. Johrendt; **"Crystal structures and magnetic properties of GaV<sub>4</sub>Se<sub>8</sub> and GaV<sub>0.5</sub>Cr<sub>3.5</sub>Se<sub>8</sub>"** *ECSSC XII European Conference on Solid State Chemistry, Münster 2009*. (Poster)

E. Wiesenmayer, H. Luetkens, G. Pascua, R. Khasanov, A. Amato, H. Potts, B. Banusch, H.-H. Klaus, D. Johrendt; **"Koexistenz von Magnetismus und Supraleitung in unterdotiertem Ba<sub>1-x</sub>K<sub>x</sub>Fe<sub>2</sub>As<sub>2</sub> (0.2 ≤ x ≤ 0.3)"** *Festkörper-Seminar Hirschegg, Hirschegg, Austria 2011*. (Talk)

G. Pascua, H. Luetkens, E. Wiesenmayer, Z. Shermadini, R. Khasanov, A. Amato, H. Maeter, H.-H. Klaus, D. Johrendt; **"Microscopic Coexistence and Competition of Magnetism and Superconductivity in Ba<sub>1-x</sub>K<sub>x</sub>Fe<sub>2</sub>As<sub>2</sub>: A Structural, Magnetic, and Superconducting Phase Diagram"** *ICM International Conference on Magnetism, Busan, Korea 2012*. (Poster)

E. Wiesenmayer, H. Luetkens, G. Pascua, R. Khasanov, A. Amato, H. Potts, B. Banusch, H.-H. Klaus, D. Johrendt; **"Microscopic coexistence of superconductivity and magnetism in Ba<sub>1-x</sub>K<sub>x</sub>Fe<sub>2</sub>As<sub>2</sub>"**, *Summer School on Iron-Pnictides, Achatswies, Germany 2012*. (Poster)

E. Wiesenmayer, A. Binek, U. Pachmayr, K. Markovic, M. Dunst, D. Johrendt; **"Optimized synthesis of Ba<sub>1-x</sub>K<sub>x</sub>Fe<sub>2</sub>As<sub>2</sub> via mechanical alloying"**, *Student Workshop, Bad Schandau, Germany 2013*. (Poster)

E. Wiesenmayer, A. Binek, U. Pachmayr, K. Markovic, M. Dunst, D. Bessinger, D. Johrendt; **"New synthetic route and optimized synthesis of Ba<sub>1-x</sub>K<sub>x</sub>Fe<sub>2</sub>As<sub>2</sub>"**, *EUCAS European Conference on Applied Superconductivity, Genoa, Italy 2013*. (Poster)

A. Malagoli, C. Bernini, E. Wiesenmayer, D. Johrendt, A. Genovese and M. Putti; **"Fabrication and characterization of superconducting (Ba<sub>0.6</sub>K<sub>0.4</sub>)Fe<sub>2</sub>As<sub>2</sub> ex-situ P.I.T. processed wires"**, *ASC Applied Superconductivity Conference, Charlotte, USA 2014*. (Poster)

## 12 Bibliography

- [1] Arbeitsgemeinschaft Energiebilanzen e.V.; Berlin; **2014**
  
- [2] L. V. Alexander, S. K. Allen, N. L. Bindoff, *et al.*, *Summary for Policymakers. In: Climate Change 2013: The Physical Science Basis. Contribution of Working Group I to the Fifth Assessment Report of the Intergovernmental Panel on Climate Change*, Cambridge University Press, Cambridge, United Kingdom and New York, NY, USA, **2013**.
  
- [3] J. Nagamatsu, N. Nakagawa, T. Muranaka, Y. Zenitani, J. Akimitsu, *Nature (London)* **2001**, 410, 63.
  
- [4] S. Sanz, T. Arlaban, R. Manzananas, M. Tropeano, R. Funke, P. Kováč, Y. Yang, H. Neumann, B. Mondesert, *Journal of Physics: Conference Series* **2014**, 507, 032040.
  
- [5] H. Kamerlingh Onnes, *Comm. Phys. Lab Leiden* **1911**, 120b.
  
- [6] H. Kamerlingh Onnes, *Comm. Phys. Lab Leiden* **1911**, 122b.
  
- [7] H. Kamerlingh Onnes, *Comm. Phys. Lab Leiden* **1911**, 124c.
  
- [8] D. K. Finnemore, T. F. Stromberg, C. A. Swenson, *Physical Review* **1966**, 149, 231-243.
  
- [9] B. T. Matthias, T. H. Geballe, S. Geller, E. Corenzwit, *Physical Review* **1954**, 95, 1435.
  
- [10] B. T. Matthias, T. H. Geballe, R. H. Willens, E. Corenzwit, G. W. Hull, Jr., *Physical Review* **1965**, 139, 1501-1503.
  
- [11] R. Chevrel, M. Hirrien, M. Sergent, *Polyhedron* **1986**, 5, 87-94.

- 
- [12] A. Schilling, M. Cantoni, J. D. Guo, H. R. Ott, *Nature* **1993**, 363, 56-58.
- [13] Y. Kamihara, T. Watanabe, M. Hirano, H. Hosono, *Journal of the American Chemical Society* **2008**, 130, 3296.
- [14] S. S. Saxena, P. B. Littlewood, *Nature* **2001**, 412, 290-291.
- [15] Z.-A. Ren, W. Lu, J. Yang, W. Yi, X.-L. Shen, Z.-C. Li, G.-C. Che, X.-L. Dong, L.-L. Sun, F. Zhou, Z.-X. Zhao, *Chinese Physics Letters* **2008**, 25, 2215.
- [16] P. Cheng, B. Shen, G. Mu, X. Zhu, F. Han, B. Zeng, H.-H. Wen, *Europhysics Letters* **2009**, 85, 67003.
- [17] M. Rotter, M. Tegel, D. Johrendt, *Physical Review Letters* **2008**, 101, 107006.
- [18] M. Gooch, B. Lv, K. Sasmal, J. H. Tapp, Z. J. Tang, A. M. Guloy, B. Lorenz, C. W. Chu, *Physica C* **2010**, 470, S276-S279.
- [19] F. Hummel, Y. Su, A. Senyshyn, D. Johrendt, *Physical Review B* **2013**, 88, 144517.
- [20] P. M. Shirage, K. Kihou, C. H. Lee, H. Kito, H. Eisaki, A. Iyo, *J Am Chem Soc* **2011**, 133, 9630-9633.
- [21] T. Stürzer, G. Derondeau, D. Johrendt, *Physical Review B* **2012**, 86, 060516.
- [22] C. Löhnert, T. Stürzer, M. Tegel, R. Frankovsky, G. Friederichs, D. Johrendt, *Angewandte Chemie International Edition* **2011**, 50, 9195-9199.
- [23] T. Nomura, S. W. Kim, Y. Kamihara, M. Hirano, P. V. Sushko, K. Kato, M. Takata, A. L. Shluger, H. Hosono, *Superconductor Science and Technology* **2008**, 21, 125028.
- [24] C. d. I. Cruz, Q. Huang, J. W. Lynn, J. Li, W. Ratcliff, J. L. Zarestky, H. A. Mook, G. F. Chen, J. L. Luo, N. L. Wang, P. Dai, *Nature* **2008**, 453, 899.

- [25] P. Klüfers, A. Mewis, *Zeitschrift für Naturforschung B* **1978**, 33, 151-155.
- [26] M. Pfisterer, G. Nagorsen, *Zeitschrift für Naturforschung B* **1980**, 35b, 703-704.
- [27] M. Rotter, M. Tegel, I. Schellenberg, W. Hermes, R. Pöttgen, D. Johrendt, *Physical Review B: Condensed Matter and Materials Physics* **2008**, 78, 020503(R).
- [28] S. Nandi, M. G. Kim, A. Kreyssig, R. M. Fernandes, D. K. Pratt, A. Thaler, N. Ni, S. L. Bud'ko, P. C. Canfield, J. Schmalian, R. J. McQueeney, A. I. Goldman, *Physical Review Letters* **2010**, 104, 057006.
- [29] M. Rotter, C. Hieke, D. Johrendt, *Physical Review B* **2010**, 82, 014513.
- [30] S. K. Kim, M. S. Torikachvili, E. Colombier, A. Thaler, S. L. Bud'ko, P. C. Canfield, *Physical Review B* **2011**, 84, 134525.
- [31] J. Bardeen, *Physical Review* **1955**, 97, 1724.
- [32] L. N. Cooper, *Physical Review* **1956**, 104, 1189.
- [33] J. Bardeen, L. N. Cooper, J. R. Schrieffer, *Physical Review* **1957**, 106, 162.
- [34] M. Tegel, PhD thesis, Ludwig-Maximilians-Universität **2011**.
- [35] A. Y. Liu, I. I. Mazin, J. Kortus, *Physical Review Letters* **2001**, 87, 087005.
- [36] J. R. Schrieffer, X. G. Wen, S. C. Zhang, *Physical Review B* **1989**, 39, 11663-11679.
- [37] N. D. Mermin, H. Wagner, *Physical Review Letters* **1966**, 17, 1133-1136.
- [38] D. Vaknin, S. K. Sinha, D. E. Moncton, D. C. Johnston, J. M. Newsam, C. R. Safinya, H. E. King, *Physical Review Letters* **1987**, 58, 2802-2805.

- 
- [39] G. Xu, H. Zhang, X. Dai, Z. Fang, *EPL (Europhysics Letters)* **2008**, *84*, 67015.
- [40] A. I. Liechtenstein, I. I. Mazin, O. K. Andersen, *Physical Review Letters* **1995**, *74*, 2303-2306.
- [41] R. Thomale, C. Platt, W. Hanke, J. Hu, B. A. Bernevig, *Physical Review Letters* **2011**, *107*, 117001.
- [42] M. Rotter, M. Pangerl, M. Tegel, D. Johrendt, *Angewandte Chemie, International Edition* **2008**, *47*, 7949-7952.
- [43] R. M. Fernandes, D. K. Pratt, W. Tian, J. Zarestky, A. Kreyssig, S. Nandi, M. G. Kim, A. Thaler, N. Ni, P. C. Canfield, R. J. McQueeney, J. Schmalian, A. I. Goldman, *Physical Review B* **2010**, *81*, 140501.
- [44] E. Hassinger, G. Gredat, F. Valade, S. R. de Cotret, A. Juneau-Fecteau, J. P. Reid, H. Kim, M. A. Tanatar, R. Prozorov, B. Shen, H. H. Wen, N. Doiron-Leyraud, L. Taillefer, *Physical Review B* **2012**, *86*, 140502.
- [45] H. Q. Yuan, J. Singleton, F. F. Balakirev, S. A. Baily, G. F. Chen, J. L. Luo, N. L. Wang, *Nature* **2009**, *457*, 565.
- [46] W. RAWDAT, 2.14 ed., STOE & Cie GmbH Darmstadt, **2005**.
- [47] W. GRAPHICS, 2.16 ed., STOE & Cie GmbH Darmstadt, **2004**.
- [48] JCPDS, 2.2 ed., International Center for Diffraction Data, Swathmore, USA, **2001**.
- [49] S. W. THEO, 2.04 ed., STOE & Cie GmbH, **2004**.
- [50] P. K. C. Villars, ASM International, Materials Park, Ohio, USA, **2009/10**.
- [51] A. Coelho, 4.1 ed., Coelho Software, Brisbane, **2007**.
-

- [52] R. W. Cheary, A. A. Coelho, J. P. Cline, *J. Res. Natl. Inst. Stand. Technol.* **2004**, *109*, 1-26.
- [53] A. Le Bail, A. Jouanneaux, *Journal of Applied Crystallography* **1997**, *30*, 265.
- [54] A. March, *Zeitschrift für Kristallographie* **1932**, *81*, 285-297.
- [55] W. A. Dollase, *Journal of Applied Crystallography* **1986**, *19*, 267-272.
- [56] M. Tegel, 1.67 rc ed., Ludwig-Maximilians-Universität, München, **2010**.
- [57] INCA, 4.02 ed., Oxford Instruments Analytical Ltd., **1998-2002**.
- [58] A. Suter, B. M. Wojek, *Physics Procedia* **2012**, *30*, 69-73.
- [59] K. Hagiwara, *Phys Rec. D* **2002**, *66*, 010001.
- [60] H. Luetkens, in *PSI Summer School*, Villigen, Switzerland, **2010**.
- [61] C. S. Wu, E. Ambler, R. W. Hayward, D. D. Hoppes, and, R. P. Hudson, *Phys. Rev.* **1957**, *105*, 1413-1415.
- [62] R. L. Garwin, L. M. Lederman, and, M. Weinrich, *Phys. Rev.* **1957**, *105*, 1415-1417.
- [63] G. Pascua, PhD thesis, Universität Zürich **2014**.
- [64] K. Muller, C. Andrikidis, H. K. Liu, S. X. Dou, *Physical review. B, Condensed matter* **1994**, *50*, 10218-10224.
- [65] A. Yamamoto, J. Jiang, C. Tarantini, N. Craig, A. A. Polyanskii, F. Kametani, F. Hunte, J. Jaroszynski, E. E. Hellstrom, D. C. Larbalestier, R. Jin, A. S. Sefat, M. A. McGuire, B. C. Sales, D. K. Christen, D. Mandrus, *Applied Physics Letters* **2008**, *92*, 252501.

- 
- [66] M. Vojenčiak, F. Grilli, A. Stenvall, A. Kling, W. Goldacker, *Cryogenics* **2013**, 57, 189-194.
- [67] C. Dong, C. Yao, H. Lin, X. Zhang, Q. Zhang, D. Wang, Y. Ma, H. Oguro, S. Awaji, K. Watanabe, *Scripta Materialia* **2015**, 99, 33-36.
- [68] Z. Gao, K. Togano, A. Matsumoto, H. Kumakura, *Superconductor Science and Technology* **2015**, 28, 012001.
- [69] A. Malagoli, *Private communication*, **2015**
- [70] V. Zinth, T. Dellmann, H.-H. Klauss, D. Johrendt, *Angewandte Chemie International Edition* **2011**, 50, 7919-7923.
- [71] H. Chen, Y. Ren, Y. Qiu, W. Bao, R. H. Liu, G. Wu, T. Wu, Y. L. Xie, X. F. Wang, Q. Huang, X. H. Chen, *Europhysics Letters* **2009**, 85, 17006.
- [72] M. Rotter, M. Tegel, I. Schellenberg, F. M. Schappacher, R. Pöttgen, J. Deisenhofer, A. Günther, F. Schrettle, A. Loidl, D. Johrendt, *New Journal of Physics* **2009**, 11, 025014.
- [73] A. A. Aczel, E. Baggio-Saitovitch, S. L. Budko, P. C. Canfield, J. P. Carlo, G. F. Chen, P. C. Dai, T. Goko, W. Z. Hu, G. M. Luke, J. L. Luo, N. Ni, D. R. Sanchez-Candela, F. F. Tafti, N. L. Wang, T. J. Williams, W. Yu, Y. J. Uemura, *Physical Review B* **2008**, 78, 214503.
- [74] T. Goko, A. A. Aczel, E. Baggio-Saitovitch, *et al.*, *Physical Review B* **2009**, 80, 024508.
- [75] J. T. Park, D. S. Inosov, C. Niedermayer, G. L. Sun, D. Haug, N. B. Christensen, R. Dinnebier, A. V. Boris, A. J. Drew, L. Schulz, T. Shapoval, U. Wolff, V. Neu, X. P. Yang, C. T. Lin, B. Keimer, V. Hinkov, *Physical Review Letters* **2009**, 102, 117006.

- [76] M. H. Julien, H. Mayaffre, M. Horvatić, C. Berthier, X. D. Zhang, W. Wu, G. F. Chen, N. L. Wang, J. L. Luo, *EPL (Europhysics Letters)* **2009**, *87*, 37001.
- [77] D. K. Pratt, W. Tian, A. Kreyssig, J. L. Zarestky, S. Nandi, N. Ni, S. L. Bud'ko, P. C. Canfield, A. I. Goldman, R. J. McQueeney, *Physical Review Letters* **2009**, *103*, 087001.
- [78] R. M. Fernandes, J. Schmalian, *Physical Review B* **2010**, *82*, 014521.
- [79] S. Avci, O. Chmaissem, E. A. Goremychkin, S. Rosenkranz, J. P. Castellán, D. Y. Chung, I. S. Todorov, J. A. Schlueter, H. Claus, M. G. Kanatzidis, A. Daoud-Aladine, D. Khalyavin, R. Osborn, *Physical Review B* **2011**, *83*, 172503.
- [80] S. D. Wilson, Z. Yamani, C. R. Rotundu, B. Freelon, E. Bourret-Courchesne, R. J. Birgeneau, *Physical Review B* **2009**, *79*, 184519.
- [81] H.-H. Klauss, H. Luetkens, R. Klingeler, C. Hess, F. J. Litterst, M. Kraken, M. M. Korshunov, I. Eremin, S.-L. Drechsler, R. Khasanov, A. Amato, J. Hamann-Borrero, N. Leps, A. Kondrat, G. Behr, J. Werner, B. Büchner, *Physical Review Letters* **2008**, *101*, 077005.
- [82] A. Jesche, N. Caroca-Canales, H. Rosner, H. Borrmann, A. Ormeci, D. Kasinathan, H. H. Klauss, H. Luetkens, R. Khasanov, A. Amato, A. Hoser, K. Kaneko, C. Krellner, C. Geibel, *Physical Review B* **2008**, *78*, 180504.
- [83] A. Yaouanc, P. D. Réotier, *MUON SPIN RELAXATION and RESONANCE*, Oxford University Press, **2011**.
- [84] C. Bernhard, A. J. Drew, L. Schulz, V. K. Malik, M. Rössle, N. Ch, W. Th, G. D. Varma, G. Mu, H. H. Wen, H. Liu, G. Wu, X. H. Chen, *New Journal of Physics* **2009**, *11*, 055050.

- [85] P. Marsik, K. W. Kim, A. Dubroka, M. Rössle, V. K. Malik, L. Schulz, C. N. Wang, C. Niedermayer, A. J. Drew, M. Willis, T. Wolf, C. Bernhard, *Physical Review Letters* **2010**, *105*, 057001.
- [86] A. V. Chubukov, D. V. Efremov, I. Eremin, *Physical Review B* **2008**, *78*, 134512.
- [87] P. J. Hirschfeld, M. M. Korshunov, I. I. Mazin, *Reports on Progress in Physics* **2011**, *74*, 124508.
- [88] P. Dai, J. Hu, E. Dagotto, *Nat Phys* **2012**, *8*, 709-718.
- [89] E. Wiesenmayer, H. Luetkens, G. Pascua, R. Khasanov, A. Amato, H. Potts, B. Banusch, H. H. Klauss, D. Johrendt, *Phys Rev Lett* **2011**, *107*, 237001.
- [90] J.-H. Chu, J. G. Analytis, K. De Greve, P. L. McMahon, Z. Islam, Y. Yamamoto, I. R. Fisher, *Science* **2010**, *329*, 824-826.
- [91] C. Fang, H. Yao, W.-F. Tsai, J. Hu, S. A. Kivelson, *Physical Review B* **2008**, *77*, 224509.
- [92] R. M. Fernandes, A. V. Chubukov, J. Schmalian, *Nat Phys* **2014**, *10*, 97-104.
- [93] S. Avci, O. Chmaissem, J. M. Allred, S. Rosenkranz, I. Eremin, A. V. Chubukov, D. E. Bugaris, D. Y. Chung, M. G. Kanatzidis, J. P. Castellán, J. A. Schlueter, H. Claus, D. D. Khalyavin, P. Manuel, A. Daoud-Aladine, R. Osborn, *Nat Commun* **2014**, *5*.
- [94] F. Waßer, A. Schneidewind, Y. Sidis, S. Wurmehl, S. Aswartham, B. Büchner, M. Braden, *Physical Review B* **2015**, *91*, 060505.
- [95] A. E. Böhmer, F. Hardy, L. Wang, T. Wolf, P. Schweiss, C. Meingast, *arXiv:1412.7038* **2014**.

- [96] A. E. Böhmer, P. Burger, F. Hardy, T. Wolf, P. Schweiss, R. Fromknecht, M. Reinecker, W. Schranz, C. Meingast, *Physical Review Letters* **2014**, *112*, 047001.
- [97] D. Hu, X. Lu, W. Zhang, *et al.*, *Physical Review Letters* **2015**, *114*, 157002.
- [98] D. K. Pratt, M. G. Kim, A. Kreyssig, Y. B. Lee, G. S. Tucker, A. Thaler, W. Tian, J. L. Zarestky, S. L. Bud'ko, P. C. Canfield, B. N. Harmon, A. I. Goldman, R. J. McQueeney, *Physical Review Letters* **2011**, *106*, 257001.
- [99] X. Lu, H. Gretarsson, R. Zhang, X. Liu, H. Luo, W. Tian, M. Laver, Z. Yamani, Y.-J. Kim, A. H. Nevidomskyy, Q. Si, P. Dai, *Physical Review Letters* **2013**, *110*, 257001.
- [100] P. J. Baker, H. J. Lewtas, S. J. Blundell, T. Lancaster, F. L. Pratt, D. R. Parker, M. J. Pitcher, S. J. Clarke, *Physical Review B* **2008**, *78*, 212501.
- [101] S. Avci, O. Chmaissem, D. Y. Chung, S. Rosenkranz, E. A. Goremychkin, J. P. Castellan, I. S. Todorov, J. A. Schlueter, H. Claus, A. Daoud-Aladine, D. D. Khalyavin, M. G. Kanatzidis, R. Osborn, *Physical Review B* **2012**, *85*, 184507.
- [102] J. E. Sonier, J. H. Brewer, R. F. Kiefl, *Reviews of Modern Physics* **2000**, *72*, 769-811.
- [103] N. Xu, P. Richard, X. Shi, A. van Roekeghem, T. Qian, E. Razzoli, E. Rienks, G. F. Chen, E. Ieki, K. Nakayama, T. Sato, T. Takahashi, M. Shi, H. Ding, *Physical Review B* **2013**, *88*, 220508.
- [104] T. Goltz, V. Zinth, D. Johrendt, H. Rosner, G. Pascua, H. Luetkens, P. Materne, H.-H. Klauss, *Physical Review B* **2014**, *89*, 144511.
- [105] V. Zinth, D. Johrendt, *EPL (Europhysics Letters)* **2012**, *98*, 57010.

- 
- [106] J. M. Allred, S. Avci, D. Y. Chung, H. Claus, D. Khalyavin, P. Manuel, M. Taddei, M. G. Kanatzidis, S. Rosenkranz, R. Osborn, O. Chmaissem, *arXiv:1505.01433* **2015**.
- [107] P. L. Alireza, Y. T. C. Ko, J. Gillett, C. M. Petrone, J. M. Cole, G. G. Lonzarich, S. E. Sebastian, *Journal of Physics: Condensed Matter* **2009**, *21*, 012208.
- [108] L. D. Jennings, C. A. Swenson, *Physical Review* **1958**, *112*, 31-43.
- [109] S. L. Bud'ko, M. Sturza, D. Y. Chung, M. G. Kanatzidis, P. C. Canfield, *Physical Review B* **2013**, *87*, 100509.
- [110] Office of Science, US Department of Energy, **2006**.
- [111] A. P. Malozemoff, *Nat Mater* **2007**, *6*, 617-619.
- [112] R. Flükiger, H. L. Suo, N. Musolino, C. Beneduce, P. Toulemonde, P. Lezza, *Physica C: Superconductivity* **2003**, *385*, 286-305.
- [113] H. Takeshi, S. Ken-ichi, H. Hajime, *Japanese Journal of Applied Physics* **1989**, *28*, L82.
- [114] J. E. Kunzler, E. Buehler, F. S. L. Hsu, J. H. Wernick, *Physical Review Letters* **1961**, *6*, 89-91.
- [115] Z. Gao, L. Wang, Y. Qi, D. Wang, X. Zhang, Y. Ma, *Superconductor Science and Technology* **2008**, *21*, 105024.
- [116] M. Vignolo, G. Bovone, C. Bernini, A. Palenzona, S. Kawale, G. Romano, A. S. Siri, *Superconductor Science and Technology* **2013**, *26*, 105022.
- [117] A. Malagoli, V. Braccini, C. Bernini, G. Romano, M. Vignolo, M. Putti, C. Ferdeghini, *Superconductor Science and Technology* **2010**, *23*, 025032.
- [118] A. Malagoli, V. Braccini, M. Vignolo, X. Chaud, M. Putti, *Superconductor Science and Technology* **2014**, *27*, 055022.
-

- [119] L. A. Schwartzkopf, J. Jiang, X. Y. Cai, D. Apodaca, D. C. Larbalestier, *Applied Physics Letters* **1999**, *75*, 3168-3170.
- [120] M. Y. Li, X. P. Chen, T. M. Qu, H. P. Yi, Z. Han, Q. Liu, *Physica C: Superconductivity* **2004**, *412–414, Part 2*, 1091-1095.
- [121] D. Larbalestier, A. Gurevich, D. M. Feldmann, A. Polyanskii, *Nature* **2001**, *414*, 368-377.
- [122] M. Majoros, B. A. Glowacki, A. M. Campbell, G. A. Levin, P. N. Barnes, M. Polak, *Applied Superconductivity, IEEE Transactions on* **2005**, *15*, 2819-2822.
- [123] A. Gurevich, *Nat Mater* **2011**, *10*, 255-259.
- [124] F. Kametani, P. Li, D. Abraimov, A. A. Polyanskii, A. Yamamoto, J. Jiang, E. Hellstrom, A. Gurevich, D. C. Larbalestier, Z. A. Ren, J. Yang, X. L. Dong, W. Lu, Z. X. Zhao, *Applied Physics Letters* **2009**, *95*, 142502.
- [125] T. Ozaki, Y. Mizuguchi, S. Demura, K. Deguchi, Y. Kawasaki, T. Watanabe, H. Okazaki, H. Hara, H. Takeya, T. Yamaguchi, H. Kumakura, Y. Takano, *Journal of Applied Physics* **2012**, *111*, 013912.
- [126] H. Izawa, Y. Mizuguchi, T. Ozaki, Y. Takano, O. Miura, *Japanese Journal of Applied Physics* **2012**, *51*, 010101.
- [127] A. Gurevich, *Reports on Progress in Physics* **2011**, *74*, 124501.
- [128] M. Yanwei, *Superconductor Science and Technology* **2012**, *25*, 113001.
- [129] Z. Gao, L. Wang, C. Yao, Y. Qi, C. Wang, X. Zhang, D. Wang, C. Wang, Y. Ma, *Applied Physics Letters* **2011**, *99*, 242506.
- [130] B. A. Glowacki, M. Majoros, M. Vickers, J. E. Evetts, Y. Shi, I. McDougall, *Superconductor Science and Technology* **2001**, *14*, 193.

- [131] A. Malagoli, C. Bernini, V. Braccini, G. Romano, M. Putti, X. Chaud, F. Debray, *Superconductor Science and Technology* **2013**, *26*, 045004.
- [132] X. Zhang, L. Wang, Y. Qi, D. Wang, Z. Gao, Z. Zhang, Y. Ma, *Physica C: Superconductivity* **2010**, *470*, 104-108.
- [133] M. J. Qin, S. Keshavarzi, S. Soltanian, X. L. Wang, H. K. Liu, S. X. Dou, *Physical Review B* **2004**, *69*, 012507.
- [134] K. Fukushima, M. Okada, J. Sato, T. Kiyoshi, H. Kumakura, K. Togano, H. Wada, *Japanese Journal of Applied Physics* **1997**, *36*, L1433.
- [135] J. D. Weiss, C. Tarantini, J. Jiang, F. Kametani, A. A. Polyanskii, D. C. Larbalestier, E. E. Hellstrom, *Nat Mater* **2012**, *11*, 682-685.
- [136] H. Lin, C. Yao, X. Zhang, C. Dong, H. Zhang, D. Wang, Q. Zhang, Y. Ma, S. Awaji, K. Watanabe, H. Tian, J. Li, *Sci. Rep.* **2014**, *4*.
- [137] T. Kazumasa, G. Zhaoshun, M. Akiyoshi, K. Hiroaki, *Superconductor Science and Technology* **2013**, *26*, 115007.
- [138] Z. Gao, K. Togano, A. Matsumoto, H. Kumakura, *Sci. Rep.* **2014**, *4*.
- [139] S. Rozsa, H. U. Schuster, *Zeitschrift für Naturforschung B* **1981**, *36B*, 1668-1670.
- [140] E. L. Fokina, N. I. Budim, V. G. Kochnev, G. G. Chernik, *Journal of Materials Science* **2004**, *39*, 5217-5221.
- [141] V. V. Tcherdyntsev, S. D. Kaloshkin, E. V. Shelekhov, A. I. Salimon, S. Sartori, G. Principi, *Intermetallics* **2005**, *13*, 841-847.
- [142] S. D. Kaloshkin, V. V. Tcherdyntsev, Y. V. Baldokhin, I. A. Tomilin, E. V. Shelekhov, *Journal of Non-Crystalline Solids* **2001**, *287*, 329-333.

- [143] V. P. Balema, J. W. Wiench, M. Pruski, V. K. Pecharsky, *Chemical Communications* **2002**, 724-725.
- [144] A. Stolle, T. Szuppa, S. E. S. Leonhardt, B. Ondruschka, *Chemical Society Reviews* **2011**, 40, 2317-2329.
- [145] C. F. Burmeister, A. Kwade, *Chemical Society Reviews* **2013**, 42, 7660-7667.
- [146] T. Baumgartner, M. Eisterer, H. W. Weber, R. Flükiger, C. Scheuerlein, L. Bottura, *arXiv:1504.05366* **2015**.